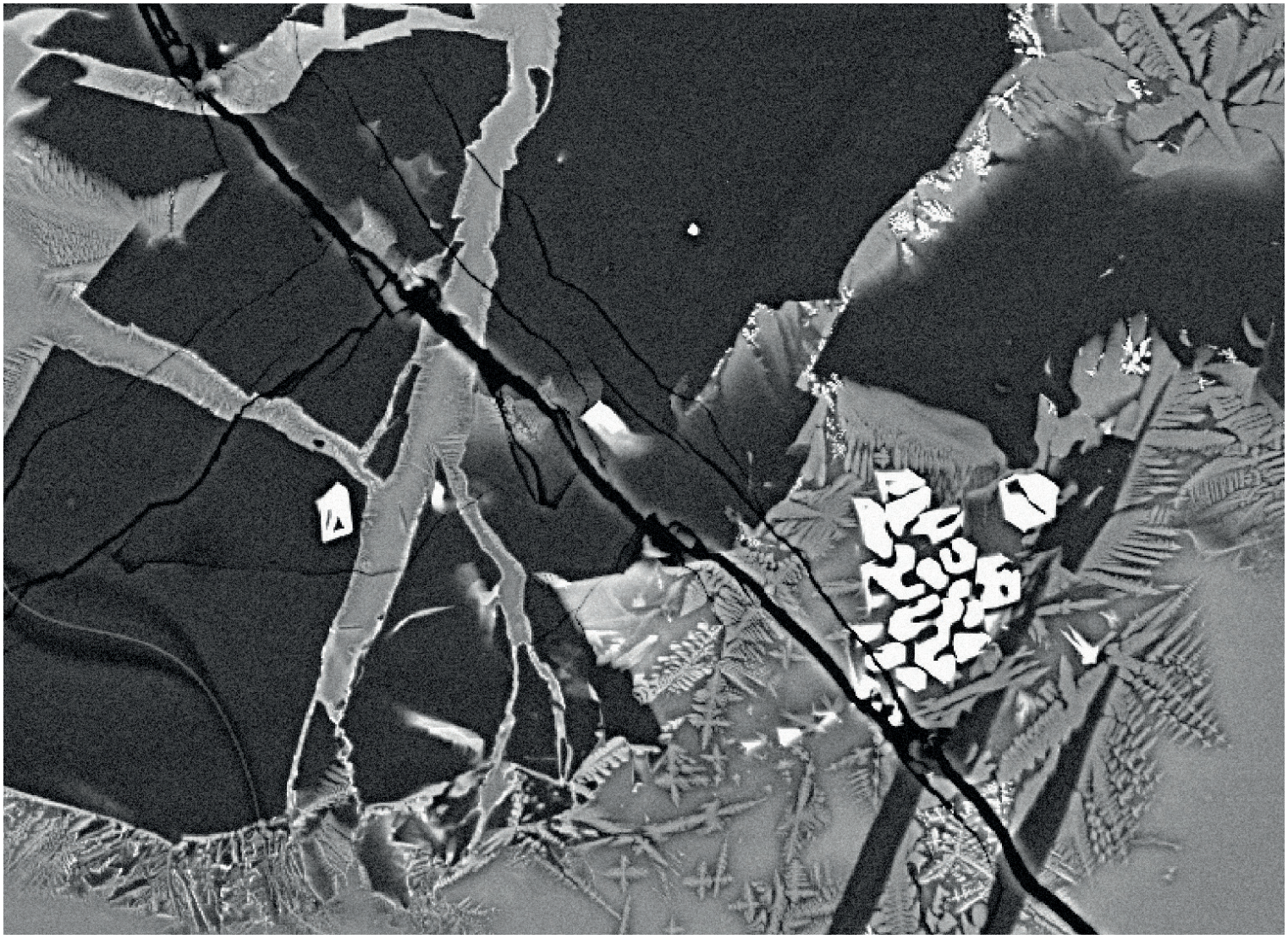

2020 ANNUAL REPORT

HP-HT laboratory

EXPERIMENTAL VOLCANOLOGY AND GEOPHYSICS

laboratory

NEW TECHNOLOGIES

Department of Seismology and Tectonophysics
Istituto Nazionale di Geofisica e Vulcanologia

Via di Vigna Murata 605 | 00143 Roma Italia | Tel +39-0651860437 | Fax +39-0651860507
www.ingv.it

Follow us on

About the cover | SEM image (550x) of the products of experiments on the fragmentation of basaltic magma. The broken crystals reveal the brittle failure of the sample and the subsequent healing of the fractures due to the viscous flow of the melt.

Credits | HPHT Lab, Jacopo Taddeucci

Follow us on

HPHTlab - Science, Technology & Engineering

HPHTlab (@hphtlab) | Twitter

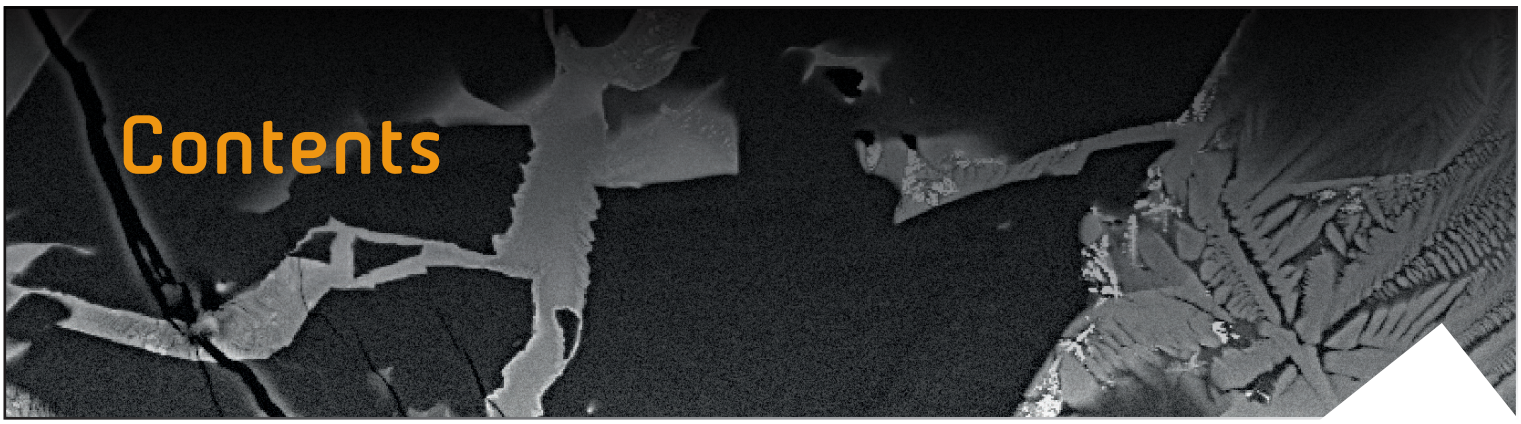

Contents

HP-HT Laboratory of Experimental Volcanology
and Geophysics LNT Laboratory of New Technologies

2020 Annual Report

1| ABSTRACT

This report summarizes the facilities, activities, collaborations, and scientific and technological products of the High Pressure High Temperature Laboratory of Experimental Volcanology and Geophysics and of the Laboratory of New Technologies for the year 2020. In this difficult year, the activities of the lab have been heavily impacted by the COVID 19 pandemic, which limited the mobility of scientists worldwide. There has been only one visiting scientists, while remote supervising has allowed 13 PhD and 10 Master students to keep their activities alive in the laboratory.

While international research projects and, to a lesser degree, field work were greatly harmed by the pandemic, the lab personnel and their associate research fellows have used their time to finalize their researches, which resulted in 46 publications in peer review journals, a total in line with that of the previous year (50). 34 abstracts were submitted to virtual or non-virtual meetings.

Finally, national and international research projects, 14 in all, have kept on driving both research activities - in the fields of petrology, mineralogy, volcanology, and rock physics - and technological development of the lab facilities during the year, but at a slower pace, with 30 summarising abstracts to be found in this report.

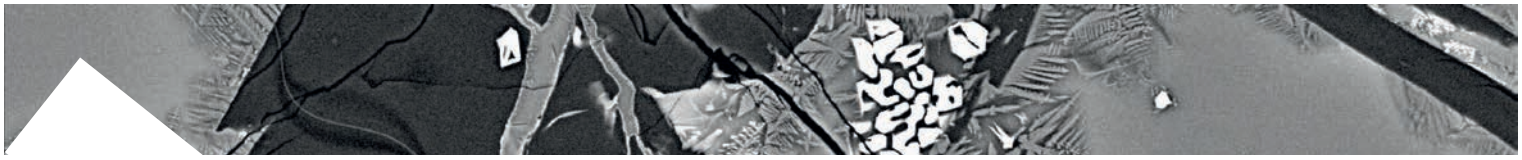

21 PERSONNEL

HPHT Laboratory

Piergiorgio Scarlato | Senior Researcher

Responsible of the HP-HT Laboratory

Stefano Aretusini | Contract Researcher
Chiara Cornelio | Contract Researcher
Gianfilippo De Astis | Senior Researcher
Elisabetta Del Bello | Researcher
Flavio Di Stefano | Contract Researcher
Valeria Misiti | Technologist
Manuela Nazzari | Researcher
Giacomo Pozzi | Contract Researcher
Tullio Ricci | Researcher
Elena Spagnuolo | Researcher
Laura Spina | Researcher
Jacopo Taddeucci | Senior Researcher

Laboratory of New Technologies

Giovanni Romeo | Technical Director

Responsible of the Laboratory of New Technologies

Giuseppe Di Stefano | Senior Technologist
Alessandro Iarocci | Engineer Technologist
Massimo Mari | Technician
Francesco Pongetti | Engineer Technician
Marcello Silvestri | Technician
Giuseppe Spinelli | Engineer Technologist
Mario Tozzi | Technician
Giuseppe Urbini | Engineer Technologist
Massimiliano Vallocchia | Technician

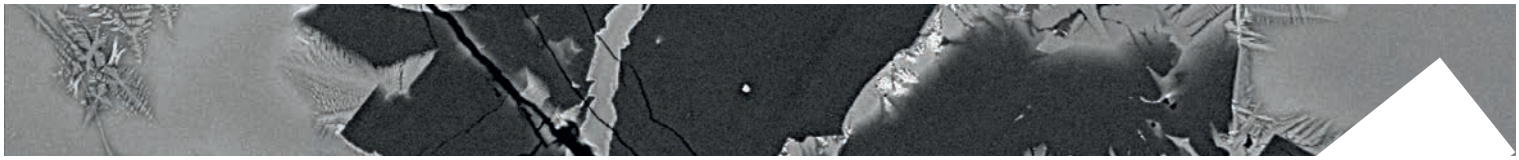

Associated researchers

Cristiano Collettini | Sapienza Università di Roma, Italy | Associated Professor in Structural Geology
Frances M. Deegan | Uppsala University, Sweden | Researcher
Giancarlo Della Ventura | Università di Roma Tre | Full Professor in Mineralogy
Giulio Di Toro | Università degli Studi di Padova, Italy | Full Professor in Structural Geology
Silvio Mollo | Sapienza Università di Roma, Italy | Associated Professor in Petrology
Vincenzo Stagno | Sapienza Università di Roma, Italy | Associated Professor in Petrology
Valentin R. Troll | Uppsala University, Sweden | Chair of Petrology

Collaborators

Luca Samuele Capizzi | Sapienza Università di Roma, Italy | Contract Researcher
Matteo Masotta | Università di Pisa, Italy | Researcher
Alessio Pontesilli | University of Otago, New Zealand | PhD
Marco M. Scuderi | Sapienza Università di Roma, Italy | RTDB Geophysics

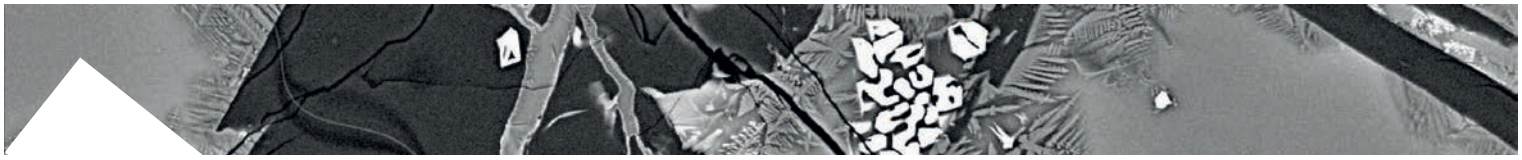

3| INSTRUMENTS and FACILITIES

HPHT Laboratory

- Multiple press 840 ton | Voggenreiter
- Piston cylinder - 3/4" and 1" pressure plates | Voggenreiter
- Multianvil - Walker type 6/8 | Voggenreiter
- Quick Press - Piston Cylinder 3/4" and 1" pressure plates | Depth of the Earth
- Bi-Tri-Axial Press (BRAVA) | RMP - INGV
- Low to High Velocity Apparatus (SHIVA) | RMP - INGV
- Electron microprobe equipped with 5 WDS and 1 EDS | JEOL JXA-8200
- Field Emission Scanning Electron Microscope equipped with EDS and BSE detectors | JEOL JSM-6500F
- Auto Carbon coater | JEOL JEC-530
- Fine coater | JEOL JFC-2300HR
- High and low temperature furnaces | Lenton
- Impedance analyser | Solartron SI1260
- Digital oscilloscope | Tektronix DPO4032
- Wave generator | Agilent 33250A
- H-Frame presses 10 ton | Enerpac
- Uniaxial testing machine with double load cell (15 and 250 kN) and LVDT controller | Tecnotest
- Precision balance | Sartorius
- Optical and stereo microscopes | Leica DMRXP and Euromex
- Ultra-high velocity, intensified, gated digital camera | Cordin 204-2
- High speed digital camcorder | Optronis and NAC 512 SC
- Stereomicroscopes | Leica MZ 9.5
- Semiautomatic polisher | Buehler Minimet 1000
- Power Supply | Agilent 6575A
- Helium Picnometer | AccuPyc II 1340
- Permeameter with double intensifier | Rock Physics
- Rheometer MCR 301 Physica | Anton Paar
- Vertical Furnace RHTV 120-300/18 | Nabertherm
- High Temperature Furnace LHT 04/18 | Nabertherm
- Cecchi data acquisition system | Applied Seismology
- Rock drilling, cutting, and grinding equipment for samples preparation
- Thermal High speed camera | FLIR SC 645
- Welder PUK U3 | Lampert
- Laser line generator | Edmund optics
- Precision test sieves | Endecotts
- Laser MGL-III, 532nm 200mW, PSU-III-LED/Unit | Changchun New Industries

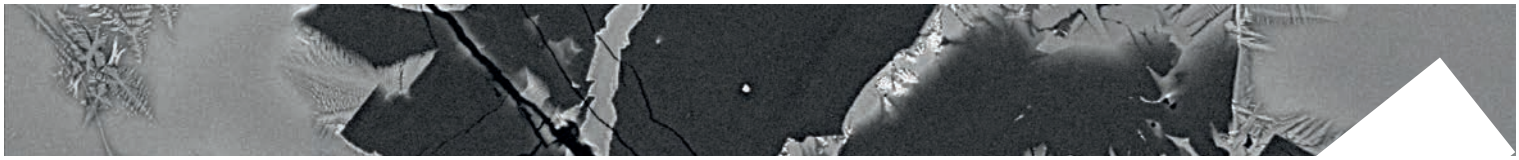

- Multi-Wavelength Analyser LUMiReader® PSA with Particle sizing according to ISO 13317
- 2 Polarized Free-feld Microphones 40AN 1/2", Low Frequency (0.5Hz - 20kHz) I G.R.A.S.
- Ext. Polarized Pressure Microphone 46DP-1 1/8", High Frequency (6.5Hz -140kHz) I G.R.A.S.
- Vacuometro PVG-500 I Pirani
- Petrographic microscope ECLIPSE E-50i POL I Nikon
- Drying oven UF 75 I Memmert
- 4K digital camcorders I Sony
- High speed digital camcorder I NAC Memrecam-HX6
- Shock-tube apparatus (Jet-Buster) I INGV
- High speed digital camcorders I NAC 512 SC, Optronis CR600x2, NAC HX6, NAC HX3
- Laser range finder I Vectronix VECTOR 21
- Time Lapse Camera with 24-70 lens I Brinno TLC200 Pro
- Precision Syringe Pumps I ISCO
- Ash dispersal/settling apparatus (Ash-Buster) I INGV
- Drone Mavic 2 Pro I DJI
- Drone Phantom 4 RTK I DJI
- Drone Mini 2 I DJI
- Dual UV cameras 340 UVGE I Thorlabs
- Laboratory sieve shaker Octagon 200 I Endecotts
- Optical Profilometer Modus6ZS-3D I DeltaPIX
- Triaxial ICP accelerometer I PCB PIezotronics
- Three ceramic shear ICP accelerometers I PCB PIezotronics
- Two 4-channel ICP sensor signal conditioners I PCB Piezonotrics
- MEERA direct shear apparatus
- High-temperature, vacuum, inert, and reactive gas furnace

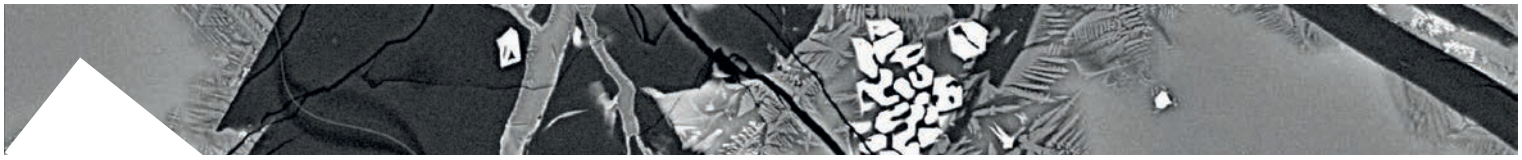

Laboratory of New Technologies

- Analog Oscilloscope | HP
- Analog Oscilloscope | Iwatsu SS5710
- Analog Oscilloscope | Tektronix TDS220
- Analog Oscilloscope | Tektronix
- Oscilloscope | HP54201
- Oscilloscope | HP54602b
- Power supply | Elind HL series
- Power supply | Elind 6TD20
- Power supply | DC DF1731SB
- Signal generator | HP8656A
- Function generator | HP3325A
- Multimeter | HP3478A
- Milling machine for printed circuit boards | T-Tech
- Logic state analyzer | HP16500A
- Superheterodyne spectrum analyzer | Tektronix
- Soldering-reworking station | JBC advanced AM6500
- Oscilloscope | FLUKE 199C
- Oscilloscope | Tektronix DPO4000
- Oscilloscope | Tektronix MSO4034
- Calibrator | FLUKE 5700 (series II)
- Function generator | HP33120
- Function generator | AGILENT 33250 A
- PXI Industrial computer with I/O boards | National Instruments
- Universal counter | HP53131A
- Waveform generator | Agilent 33210 A
- Oscilloscope W wave surfer | LeCroy 44MXs-A
- Drone Phantom 3 pro with termination system
- Power supply (4 items) | -3005D

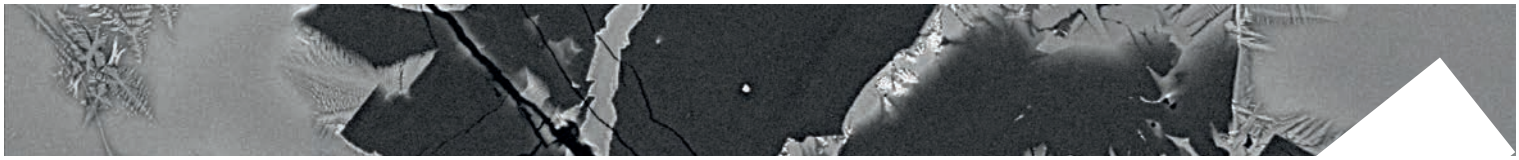

Machine shop

- Lathe | Grazioli Fortuna
- Small lathe | Ceriani
- Small milling machine | Schaublin
- Cutting machine | Ercoletta
- Bending machine | Ercoletta
- Drill press | Serrmac
- Small drill press | Webo
- Bandsaw | Femi
- Grinder | Femi
- Extractor hood | Filcar
- Inverter welding machine | Tecnica
- TIG welding machine | Cebora
- Miter saw
- Numerically controlled milling machine

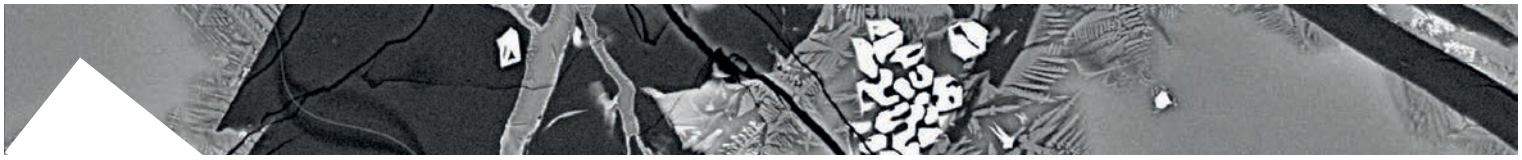

4| LABORATORY ACTIVITIES

Experimental laboratory

Super press | Multi Anvil

10 experiments have been conducted with the aim to investigate the structural behavior of tourmaline minerals as function of pressure, temperature and oxygen fugacity with implications for the mobilization of boron during subduction. From the technical point of view, the use of a cell assembly with 18mm octahedron edge length coupled with WC anvils of 11mm truncation was calibrated at 3 and 6 GPa. Experiments were performed under oxygen fugacity buffered by carbon-CO_2 and Re-ReO_2 using the double capsule technique.

Quick press | Piston cylinder

During 2020 no experiments were conducted due to the Covid19 pandemia. Anyway, we improve the machine inserting an electrovalve.

BRAVA

During the 2020 we performed about 70 friction experiments, which were designed and run to test:

1) Frictional properties anhydrite-dolomite powder mixtures and slip velocity profiles produced during stick-slip events
2) Frictional properties of clay-bearing rocks in dry and wet conditions.

BRAVA was used in collaboration with La Sapienza University to train two PhD students and to produce their first datasets of mechanical data and associated microstructures.
BRAVA maintenance was also performed during 2020. Intervents include
1) Revision and fix of the refrigeration system.
2) Removal of the oil leakage from the pressurised lines.

Slow to HIgh Velocity Apparatus (SHIVA)

The tenth year of activity of SHIVA has been mainly dedicated to:
1. the investigation of fluid – rock interaction in affecting frictional properties of bare rocks and gouges. The latter in particular by developing a new system for fluid pressurization of gouges.
2. The study of natural and experimental smectite group clay minerals to understand the mechanical behavior and the deformation processes pertaining to subduction zone fault cores at shallow depth (<1 km) following IODP projects e.g. Sumatra-Adaman region and Hikurangi subduction zones.
3. The study of the energy budget and the thermomechanical weakening of fault rocks by means of: optical fibers to measure the temperature increase directly inside the fault zone and by using dynamically consistent slip velocity functions.

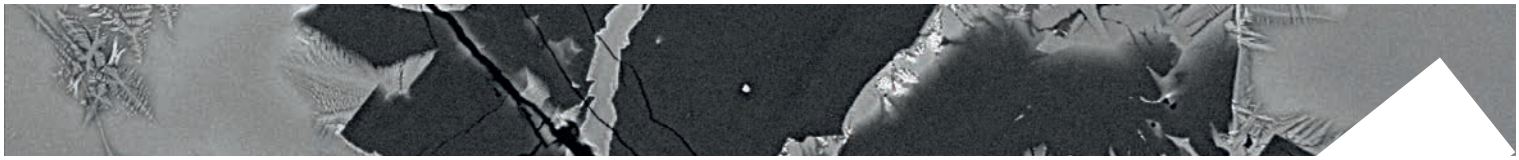

We developed a new system to overcome a challenging technical problem of gouge confinement with pressurized fluids.
We are now able to control the slip velocity functions to test dynamically consistent conditions of frictional behavior at earthquake slip velocities.
We run 55 experiments during 2020 due to the pandemic situation.

Analog modeling laboratory

The Jet Burster laboratory device for the study of volcanic particles ejection and sedimentation was implemented with three electrovalves and a new, small-diameter tube. The use of the electrovalves increases the number of experiments per day by a factor of ten. The acquisition of a new microphone for the high-frequencies (up to 140 kHz) is allowing the recording of the jet noise generated by the experiments. We are currently working on the effect of particles on supersonic jets and on the development of a new, better performing, portable wind tunnel for the in-situ study of the resuspension of volcanic ash.

FaMoUS (Fast Multiparametric Setup)

In the period 2-5 July and 6-13 October, we carried out two field campaigns at Stromboli to study: i) the variations of the ordinary explosive activity and degassing, ii) the modifications of the active vents and of the crater terrace morphology, iii) the chemical and textural variations of tephra. The October campaign coincided with the 7th edition of BAcIO multi-parametric field experiment on Stromboli, in collaboration with international research partners @LMU.

Visible Highspeed cameras (*NAC and Optronis*): i) about 30 Strombolian explosions events were filmed at 500 fps and at 1280x1024 pixel resolution.
Infrared Camera: about 1 to 5 hours of continuous recording of the volcanic activity at the crater terrace of Stromboli were acquired at 50 Hz and at 640x480 pixel resolution.
UV Camera: about 1 to 5 hours of continuous recording of the volcanic activity at the crater terrace of Stromboli were acquired at a 50 Hz and at 640x480 pixel resolution.
Drone: 5 daily drone overflights were performed.
Sampling: about 16 rock samples were collected, of which 10 were of tephra, collected during fallout from as many explosions.

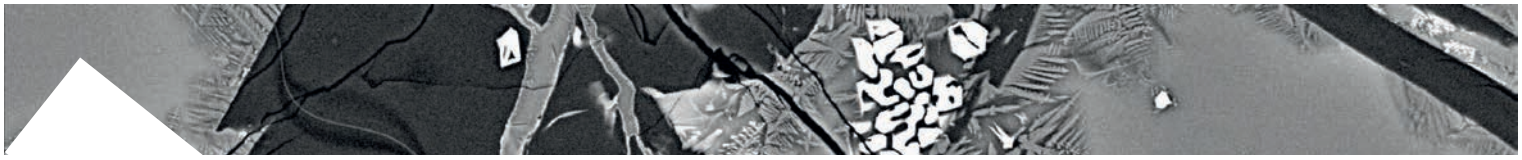

Microanalytical laboratory

FE-SEM and EMP performed 132 days of analyses in the frame of 16 research proposals.

Proposal

1. Experimental investigation of mechanisms generating phonolites in the Dunedin Volcano, New Zealand
   A. Pontesilli – M. Nazzari | University of Otago (New Zealand) - INGV Roma1

2. Kinetic aspects of major and trace element partitioning between olivine and melt during solidification of terrestrial and extraterrestrial basaltic materials
   S. Langh – V. Misiti - P. Scarlato | Sapienza University of Rome - INGV Roma1

3. Timescales of magmatic processes
   I. Arienzo – M. Nazzari | INGV OV - INGV Roma1

4. Formation of mirror-like surfaces in faulted bituminous dolostones (Vado di Ferruccio, Italian Central Apennines)
   G. Di Toro – E. Spagnuolo | University of Padova - INGV Roma 1

5. Lab-study on the frictional properties of basalts interacting with H_2O- and CO_2- rich fluids and implications for CO_2 storage
   P. Giacomel – E. Spagnuolo | Sapienza University of Rome - INGV Roma1

6. Characterization of Stromboli volcanics from 2019 paroxysms
   G. De Astis | INGV Roma1

7. Analysis of Pre- and post-Experimental Clays and Rocks (APECAR) storage
   S. Aretusini – E. Spagnuolo | INGV Roma 1

8. In situ viscosity and structural measurements of volatile-bearing melts at upper mantle pressure-temperature conditions
   V. Stagno – P. Scarlato | Sapienza University of Rome - INGV Roma1

9. Reconstruction of the intensive variables and magmatic architecture of Vulcano island
   F. Palummo – M. Nazzari – G. De Astis | Sapienza University of Rome - INGV Roma1

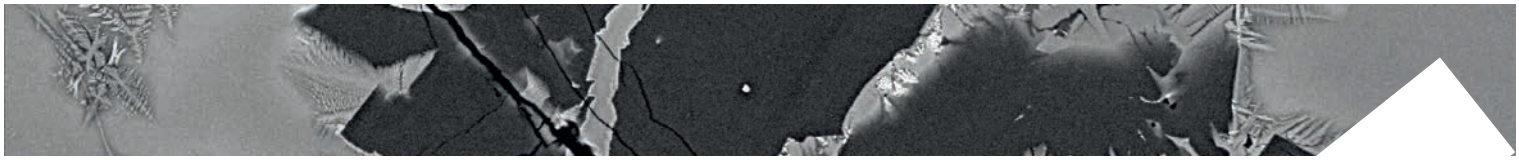

10. **Volcanic hazard assessment at Mt. Etna: a time-integrated, polybaric and polythermal perspective**
    P. Moschini – P. Scarlato | Sapienza University of Rome - INGV Roma1

11. **The 3 July 2019 paroxysm at Stromboli volcano (Itay): is Stromboli playing by new rules?**
    P. Scarlato – M. Nazzari | INGV Roma 1

12. **COupling of Rheology and Textures in Experimental Seismic faults (CORTES)**
    G. Pozzi | INGV Roma 1

13. **Fractured microlites**
    J. Taddeucci | INGV Roma 1

14. **Petrological study of a tephritic to phono-tephritic caldera forming eruption: the case of Onano Eruption (Latera volcano, Central Italy)**
    P. Landi | INGV PI

15. **Crystal-chemical variations induced by variable cooling rate in sub-alkaline silicate liquids**
    G. Iezzi – V. Misiti | University of Chieti - INGV Roma1

16. **Short time scales textural and chemical variations in strombolian tephra samples**
    E. Del Bello - S. Mollo - M. Nazzari | INGV Roma 1 - Sapienza University of Rome

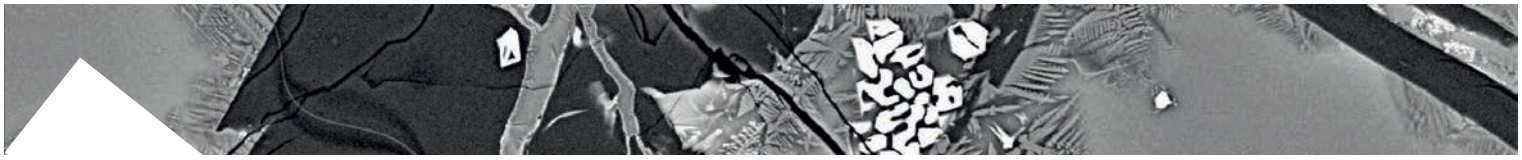

5| RESEARCH PROJECTS

1. **MIUR Progetti Premiali 2015**
   Ash-RESILIENCE A research infrastructure for volcanic ash hazard assessment to aviation and communities living near Italian active volcanoes | **P.I. A. Costa, D. Andronico**

2. **MIUR Progetto PRIN**
   Scales of solidification in magmas: applications to volcanic eruptions, silicate melts, glasses, glass-ceramics | **P.I. M. Carroll**

3. **MIUR PON-GRINT**
   EUROPEAN PLATE OBSERVING SYSTEM ACRONIMO: GRINT | **P.I. G. Puglisi**

4. **European research project**
   EUROVOLC 'European Network of Observatories and Research Infrastructures for Volcanology'
   P.I. K. VogFjiord

5. **European research project**
   EPOS 'European Plate Observing System' Implementation Phase, WP 16 Multi-scale Laboratories
   P.I. M. Cocco

6. **DPC Grant – EXTEND**
   Estendere la conoscenza del terremoto dalla profondità in superficie | **P.I. E. Spagnuolo**

7. **Petrobras3 - Petroleo Brasileiro S.A.**
   Igneous rocks as source and sink of abiotic hydrocarbons and CO_2 | **P.I. G. Etiope**

8. **INGV "Ricerca libera" Project**
   Magma dynamics triggering the 3 July and 28 August 2019 paroxysms at Stromboli volcano: A comparative approach based on the ascent rates, timescales and P-T-H_2O paths of magma
   P.I. P. Scarlato

9. **INGV "Ricerca libera" Project**
   PoWAR, a Portable Wind-tunnel for volcanic Ash Resuspension | **P.I. J. Taddeucci - E. Del Bello**

10. **INGV "Ricerca libera" Project**
    ROUGHER, expeRimental Observations aboUt irreGular cHannel gEometRies | **P.I. L. Spina**

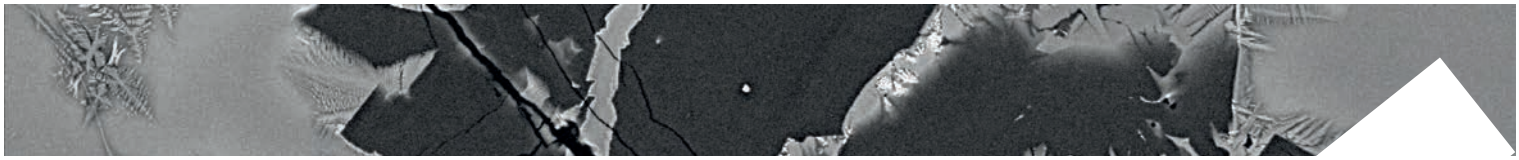

11. INGV Departmental Strategic Projects

UNO - UNderstanding the Ordinary to forecast the extraordinary: An integrated approach for studying and interpreting the explosive activity at Stromboli volcano | **P.I. P. Scarlato**

12. INGV "Pianeta Dinamico" Project

Task V1: Studio 3D-4D della struttura dei vulcani tramite tecniche di geofisica di esplorazione e confronto, integrazione e modellazione di dati geofisici, geochimici e geodetici.| **P.I. G. Ventura, P. Augliera**

13. "Esopianeti" ASI-INAF Project | P.I. G. De Astis

14. ERC Syn Fear

Fault activation and Earthquake Rupture | **P.I. D. Giardini, F. Amman, M. Cocco, S. Wiemer**

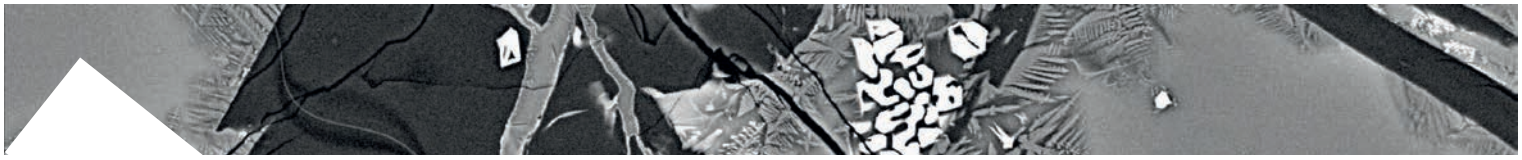

6| PARTNER LABORATORIES

1. Planetary Environmental Facilities | **Aarhus University** | Denmark

2. Experimental & Physical Volcanology | **Ludwig Maximillians Universitat** | Germany

3. Dipartimento di Scienze | **Unversità di Roma Tre** | Italy

4. Geoscience Department | **Utrecht University** | Netherlands

5. Institute of Geochemistry and Petrology | **ETH Zurich** | Switzerland

6. Dipartimento di Scienze Biologiche, Geologiche e Ambientali | **Università di Catania** | Italy

7. Dipartimento di Fisica e Scienze della Terra | **Università di Ferrara** | Italy

8. Petro-Volcanology Research Group (PVRG) Department of Physics and Geology
Università di Perugia | Italy

9. School of Earth and Environmental Sciences | **University of Queensland** | Australia

10. Department of Geology | **University of Otago** | New Zealand

11. Dipartimento di Geoscienze | **Università di Padova** | Italy

12. LEMR | EPFL | **Lausanne** | Switzerland

13. Rock Mechanics Laboratory | **Durham University** | UK

14. Jackson School of Geosciences | **Texas University at Austin** | USA

15. The Rocks Physics and Mechanics Laboratory (RPML) | **ETH** | Switzerland

16. Rock Mechanics Laboratory | **UCL Earth Sciences** | UK

17. Laboratoire Aleas geologiques et Dynamique sedimentaire | **IFREMER** | France

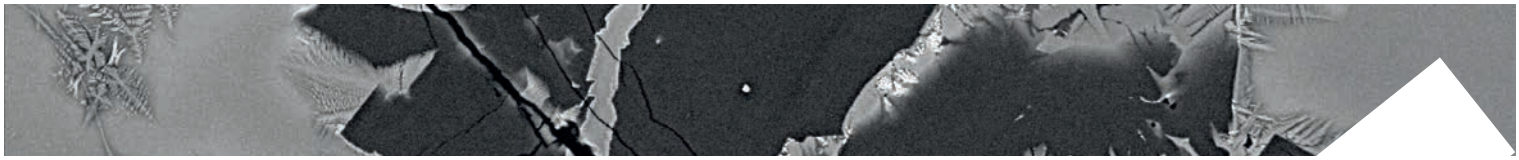

7| PARTNER INSTITUTIONS

1. Ludwig Maximillians Universitat Munchen | **Munich** | Germany

2. Department of Geology and Geophysics, SOEST | **University of Hawaii** | USA

3. Department of Physics and Astronomy | **Aarhus University** | Denmark

4. HVO Hawaiian Volcano Observatory | **USGS** | USA

5. School of Earth and Environmental Sciences | **University of Queensland** | Australia

6. Department of Geology | **University of Otago** | New Zealand

7. Department of Earth Sciences | **University of Durham** | UK

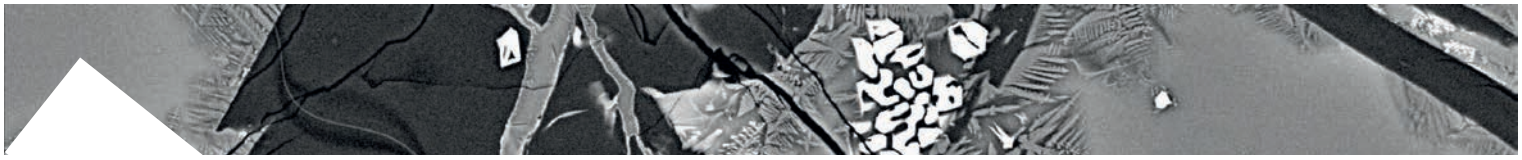

8| RESEARCH ACTIVITY and RESULTS

8.1 PETROLOGY, MINERALOGY, VOLCANOLOGY

Clustering of Experimental Seismo-Acoustic Events Using Self-Organizing Map (SOM)

Giudicepietro F., Esposito A.M., Spina L., Cannata A., Morgavi D., Layer L., Macedonio G.

The analogue experiments mimicking conduit dynamics of gas-bearing magmas and the related seismo-acoustic events are relevant for understanding the degassing processes of a volcanic system. The aim of this work is to design an unsupervised neural network for clustering experimental seismo-acoustic events to investigate the possible cause-effect relationships between the obtained signals and the processes. We focused on two tasks: 1) identify an appropriate strategy for parameterizing experimental seismo-acoustic events recorded during analogue experiments devoted to the study of degassing behaviour at basaltic volcanoes; 2) define the set up of the selected neural network, the Self-Organizing Map (SOM), suitable for clustering the features extracted from the experimental events. The seismo-acoustic dataset derives from the work of Spina et al. (2019) and consists of seismic and acoustic events generated using an ad hoc experimental setup under different physical conditions of the analogue magma (variable viscosity), injected gas flux (variable flux velocity) and conduit surface (variable surface roughness). We tested the SOMs ability to group the experimental seismo-acoustic events generated under controlled conditions and conduit geometry of the analogue volcanic system. We used 616 seismo-acoustic events characterized by different analogue magma viscosity (10, 100, 1000 Pa s), gas flux (5, 10, 30, 60, 90, 120, 150, 180 x 10-3 l/s) and conduit roughness (i.e. different fractal dimension FD corresponding to 2, 2.18, 2.99). We parameterized the seismo-acoustic events in the frequency domain by applying

the analogue experiments mimicking conduit dynamics of gas-bearing magmas and the related seismo-acoustic events are relevant for understanding the degassing processes of a volcanic system. The aim of this work is to design an unsupervised neural network for clustering experimental seismo-acoustic events to investigate the possible cause-effect relationships between the obtained signals and the processes. We focused on two tasks:

1) identify an appropriate strategy for parameterizing experimental seismo-acoustic events recorded during analogue experiments devoted to the study of degassing behaviour at basaltic volcanoes;

2) define the set up of the selected neural network, the Self-Organizing Map (SOM), suitable for clustering the features extracted from the experimental events.

The seismo-acoustic dataset derives from the work of Spina et al. (2019) and consists of

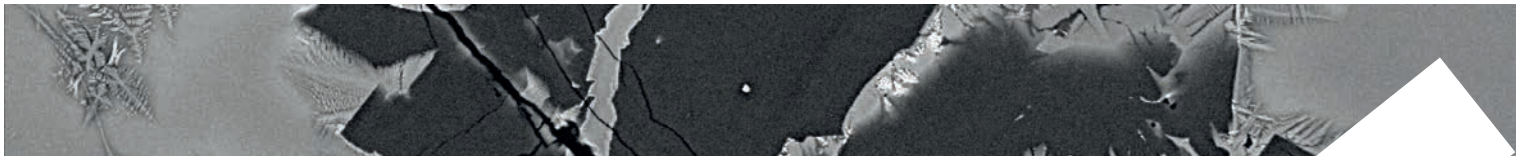

seismic and acoustic events generated using an ad hoc experimental setup under different physical conditions of the analogue magma (variable viscosity), injected gas flux (variable flux velocity) and conduit surface (variable surface roughness). We tested the SOMs ability to group the experimental seismo-acoustic events generated under controlled conditions and conduit geometry of the analogue volcanic system. We used 616 seismo-acoustic events characterized by different analogue magma viscosity (10, 100, 1000 Pa s), gas flux (5, 10, 30, 60, 90, 120, 150, 180 × 10^{-3} l/s) and conduit roughness (i.e. different fractal dimension FD corresponding to 2, 2.18, 2.99). We parameterized the seismo-acoustic events in the frequency domain by applying the Linear Predictive Coding to both accelerometric and acoustic signals generated by the dynamics of various degassing regimes, and in the time domain, applying a waveform function. Then we applied the SOM algorithm to cluster the feature vectors extracted from the seismo-acoustic data through the parameterization phase, and identified different clusters. The results were consistent with the experimental findings on the role of viscosity, flux velocity and conduit roughness on the degassing regime. In particular, based on SOM map results, four main clusters were identified (Figure 1). Cluster 1 mostly gathers seismo-acoustic events characterized by low viscous magma and smooth conduit, with few exceptions featuring 100 Pas viscosity and low (<60x10^{-3} l/s) gas flow rate. Cluster 2 and 3 are also characterized by low viscosity condition (10 Pas), but they are capable of separating different degrees of conduit roughness (FD=2.18 and FD=2.99, respectively). Finally, Cluster 4 features higher analogue magma viscosity (100 Pa s and few cases with 1000 Pa s) and gas flux generally above the threshold of 60 x10^{-3} l/s. It is likely that clusters associating 10 Pa s events (Cluster 1, 2, 3) and the one (Cluster 4) grouping high viscosity (100-1000 Pa s) and moderate to high gas flux events might actually reflect different degassing regimes, i.e. slug or churn-annular flow.

The neural network has proven to be capable of separating events generated under different experimental conditions. This suggests that the SOM is appropriate for clustering natural events such as the seismo-acoustic transients accompanying Strombolian explosions and that the adopted parameterization strategy may be suitable to extract the significant features of the seismo-acoustic (and/or infrasound) signals linked to the physical conditions of the volcanic system.

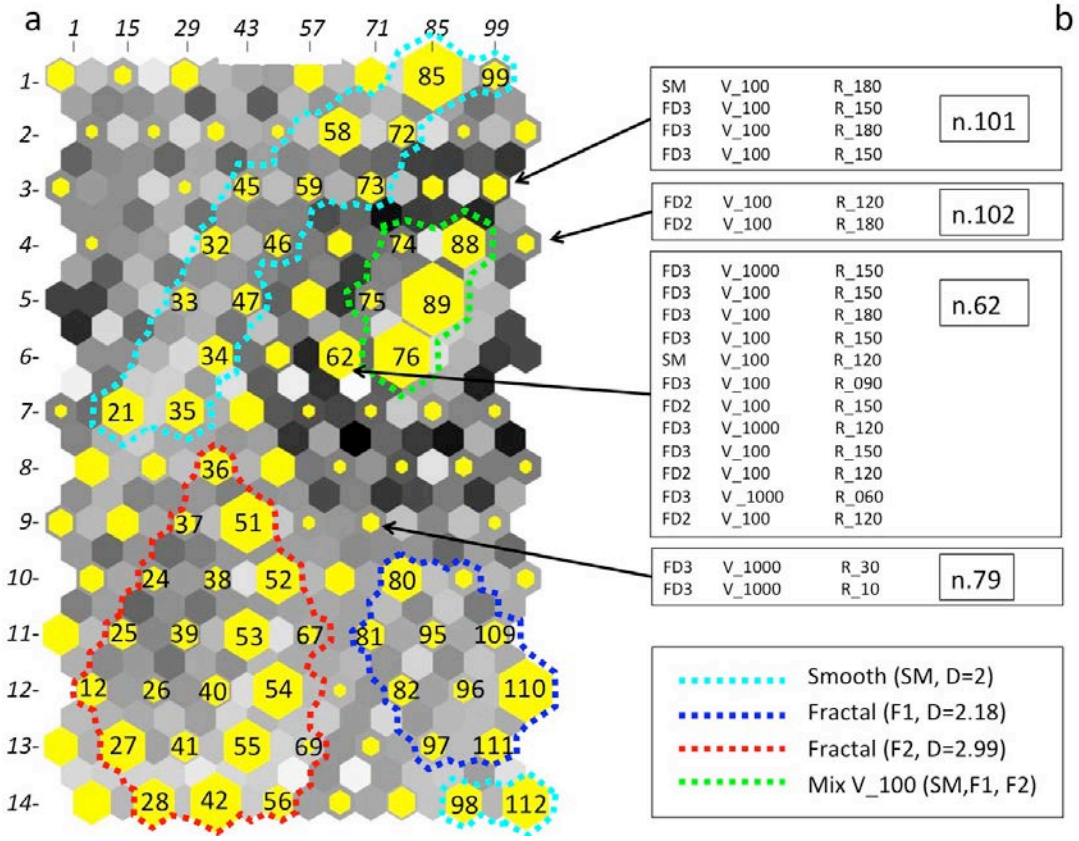

Fig. 1l a) The SOM Map with 14 x 8 =112 nodes. Not-empty nodes are shown as yellow hexagons and their size represents the data density. The numbers on the outside of the map indicate the numbering of the nodes that is also reported in some significant nodes. The grey hexagons interposed between the yellow ones indicate the Euclidean distance between the nodes according to a grey scale. Cluster 1 (cyan), Cluster 2 (blue), Cluster 3 (red) and Cluster 4 (green) are highlighted by dotted outlines. On the right (b) the compositions of nodes n.62, n.79, n.101 and n.102 are shown. The labels SM, F1 and F2 indicate SM (smooth), F1 (FD=2.18) and F2 (FD=2.99) conduit roughness, respectively.
The number preceded by V indicates the viscosity in Pa s and the number preceded by R indicates the gas flow rate in 10^{-3} l / s.

Carrier and dilution effects of CO_2 on thoron emissions from a zeolitised tuff exposed to subvolcanic temperatures

Mollo S., Moschini P., Galli G., Tuccimei P., Lucchetti C., Iezzi G., Scarlato P.

Radon (^{222}Rn) and thoron (^{220}Rn) are two isotopes belonging to the noble gas radon (sensu lato) that is frequently employed for the geochemical surveillance of active volcanoes. Temperature gradients operating at subvolcanic conditions may induce chemical and structural modifications in rock-forming minerals and their related ^{222}Rn-^{220}Rn emissions. Additionally, CO_2 fluxes may also contribute enormously to the transport of radionuclides through the microcracks and pores of subvolcanic rocks. In view of these articulated phenomena, we have experimentally quantified the changes of ^{220}Rn signal caused by dehydration of a zeolitised tuff exposed to variable CO_2 fluxes.

Results indicate that, at low CO_2 fluxes, water molecules and hydroxyl groups adsorbed on the glassy surface of macro- and micropores are physically removed by an intermolecular proton transfer mechanism, leading to an increase of the ^{220}Rn signal. In contrast, at high CO_2 fluxes, ^{220}Rn emissions dramatically decrease because of the strong dilution capacity of CO_2 that overprints the advective effect of carrier fluids (Figure 1). We conclude that the sign and magnitude of radon (sensu lato) changes observed in volcanic settings depend on the flux rate of carrier fluids and the rival effects between advective transport and radionuclide dilution

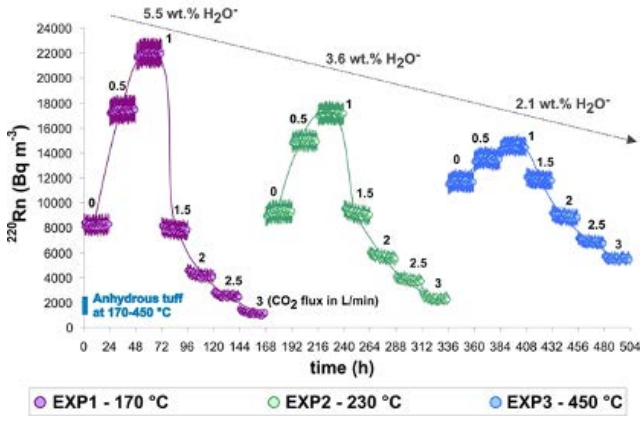

Fig. 1| ^{220}Rn vs. time diagram showing the effect of temperature, water vapour release and CO_2 flux rate on the thoron signal.

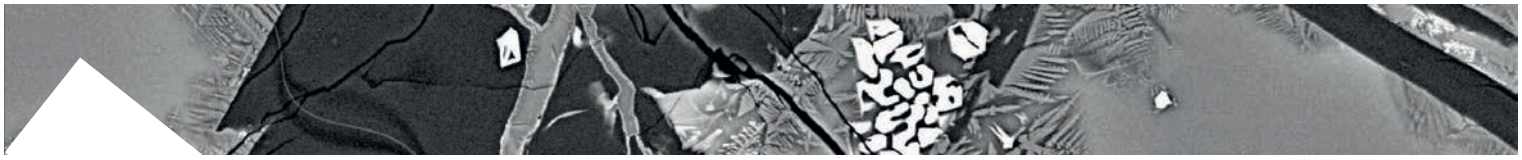

Parameterization of clinopyroxene growth kinetics via crystal size distribution (CSD) analysis: Insights into the temporal scales of magma dynamics at Mt. Etna volcano

Moschini P., Mollo S., Gaeta M., Fanara S., Nazzari M., Petrone C.M., Scarlato P.

There is increasing recognition that both textural and compositional changes of clinopyroxene crystallizing from mafic alkaline magmas are the direct expression of complex dynamic processes extending over a broad range of spatial and temporal scales. Among others, supersaturation and relaxation phenomena play a key role in controlling the final crystal cargo of variably undercooled magmas erupted from active alkaline volcanoes. In this context, we have carried out isothermal-isobaric, decompression, and cooling rate experiments on a basalt interpreted as the progenitor of mafic alkaline eruptions at Mt. Etna volcano (Sicily, Italy). The main purpose is to reconstruct and quantify the textural changes (i.e., length of major and minor axes, surface area per unit volume, area fraction, and maximum growth rate) of clinopyroxene upon variable pressures (30-300 MPa), temperatures (1,050-1,100°C), volatile contents (0-5 H_2O and 0-0.2 wt.% CO_2), and equilibration times (0.25-72 h). By integrating experimental data and thermodynamic modeling, the transition between interface-controlled (euhedral morphologies) and diffusion-controlled (anhedral morphologies) growth regimes has been determined at an undercooling threshold value of ~33 °C. Early melt supersaturation causes the fast growth of tiny clinopyroxenes with strong disequilibrium shapes, whereas an increasing relaxation time leads to the slow growth of large clinopyroxenes showing textural equilibration. According to these kinetic principles, both growth rate and relaxation time have been parameterized in relation to the crystal size distribution (CSD) analysis of naturally undercooled clinopyroxenes erupted during 2011-2012 lava fountain episodes at Mt. Etna volcano. Results indicate that the crystallization of microphenocrysts and microlites takes place by (dis)equilibrium growth conditions in the order of ~100-101 min (large undercooling, short equilibration time) and ~101-102 hours (small undercooling, long equilibration time), respectively (Figure 1). This temporal information allows to disentangle the cooling and decompression paths of Etnean magmas rising and accelerating along a vertically extended, highly dynamic plumbing system. While clinopyroxene microlites develop during the fast ascent of magmas (~100-101 m s^{-1}) within the uppermost part of the conduit or immediately before ejection from the vent, the onset of microphenocryst crystallization occurs at depth and continues within the plumbing system during the slow ascent of magmas (~10^{-2} m s^{-1}) that migrate through interconnected storage regions (Figure 1).

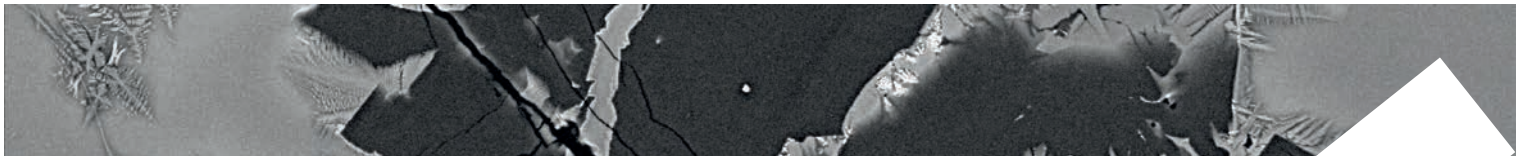

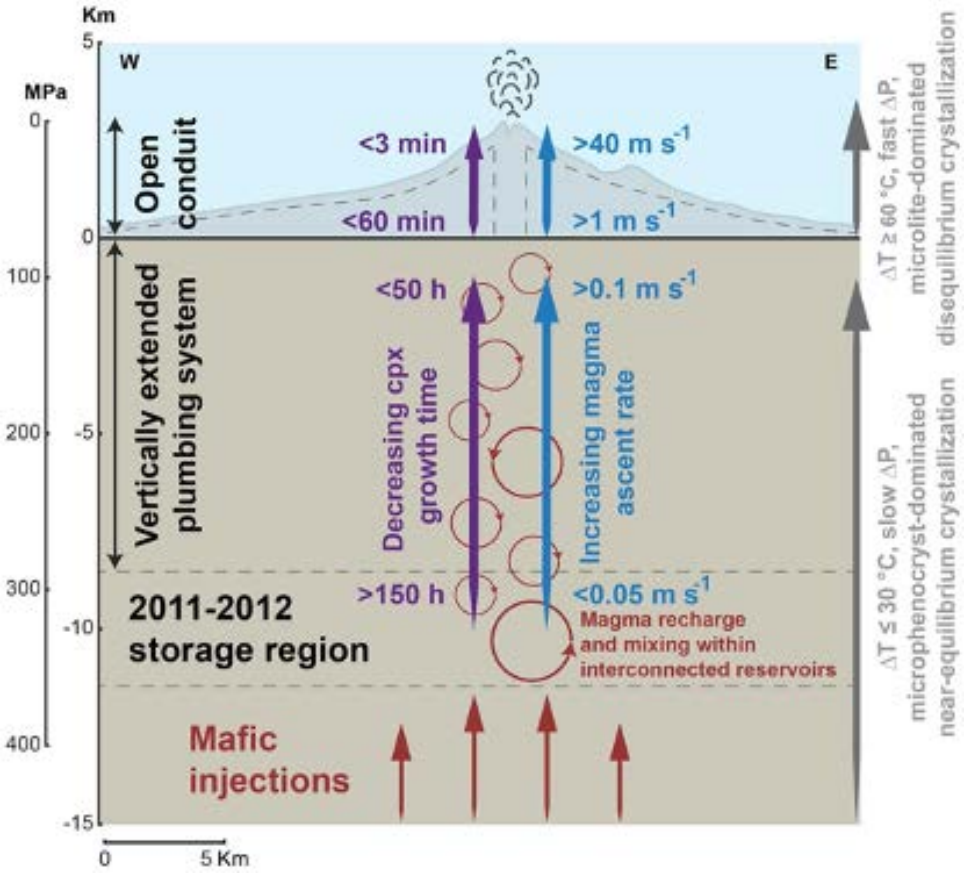

Fig. 1| Conceptual model of magma dynamics at Mt. Etna volcano describing the different time scales estimated for microlite and microphenocryst crystallization. Magma ascent velocities are also modeled accounting for either slow magma ascent rates within the interconnected storage regions forming the plumbing system architecture at depth or fast magma ascent rates within the uppermost part of the volcanic conduit and before eruption at the vent.

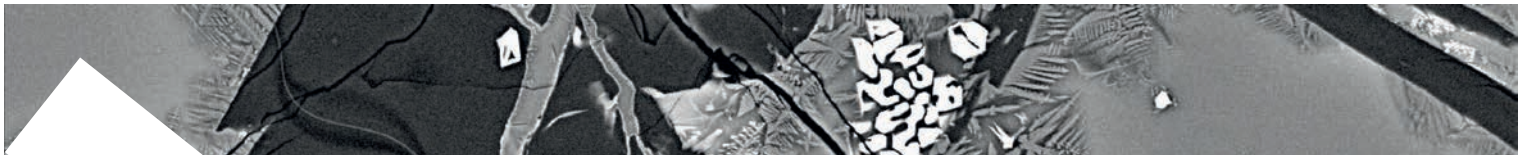

Petrological and geochemical modeling of magmas erupted at Vulcano Island in the period 54-8 ka: Quantitative constraints on the sub-volcanic architecture of the plumbing system

Palummo F., Mollo S., De Astis G., Di Stefano F., Nazzari M., Scarlato P.

In this study, we present new mineralogical and petrological data on olivine, clinopyroxene, plagioclase, and titanomagnetite phenocrysts from fifteen eruptive products (i.e., scoriae, lava flows, lava domes, and lava dykes) erupted at Vulcano Island (Aeolian Arc, Italy) over a long period of time from 54 to 8 ka and representative of Eruptive Epochs from 5 to 8, according to the chronostratigraphy of the last geological map. These rocks show shoshonitic (SHO) to high-K calc-alkaline (HKCA) affinity, with compositions changing from primitive basalts-shoshonites ($Mg\#_{35-60}$) to intermediate latites ($Mg\#_{32-54}$) to evolved trachytes-rhyolites ($Mg\#_{23-40}$).

The intensive variables driving the crystallization path of magmas were reconstructed through mineral-melt equilibrium and thermodynamic models, as well as barometers, thermometers, hygrometers and oxygen barometers. The stability of olivine (Fo_{59-91}), as first phase on liquidus, is more favored at low-*P* (100-300 MPa) and high-H_2O (4 wt.%) contents dissolved in the melt. Afterwards, the melt is co-saturated with clinopyroxene ($Mg\#_{92}$, diopside), which composition progressively evolves ($Mg\#_{71}$, augite) as the temperature decreases to 1,100 °C. The jadeite exchange between clinopyroxene and melt indicates that the crystallization pressure of magmas decreases from basalts (550-750 MPa) to shoshonites-latites-trachytes (100-450 MPa) to rhyolites (~50 MPa). The melt-H_2O content (0.5-4.2 wt.%) is sensitive to either pressure or melt composition, thereby controlling the plagioclase stability and chemistry (An_{13-77}) within a thermal path of ~860-1,100 °C. Titanomagnetite (Usp_{11-39}) equilibrates with progressively more oxidized melts as the magma composition changes from basalt (ΔQFM+1.5) to rhyolite (ΔQFM+3). Mass balance calculations and trace element modeling indicate that basaltic to trachytic magmas are prevalently controlled by fractional crystallization processes, in concert with variable degrees of assimilation of crustal rocks. Conversely, rhyolitic and highly differentiated trachytic magmas are generated by extraction of interstitial melts from shallow mush zones dominated by feldspar and titanomagnetite saturation. We conclude that the architecture of the plumbing system at Vulcano Island is characterized by multiple reservoirs in which compositionally distinct magmas pond and undergo polybaric-polythermal differentiation, before erupting to the surface (Figure 1).

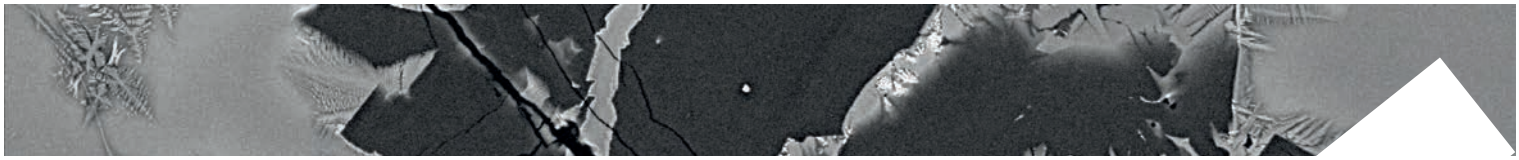

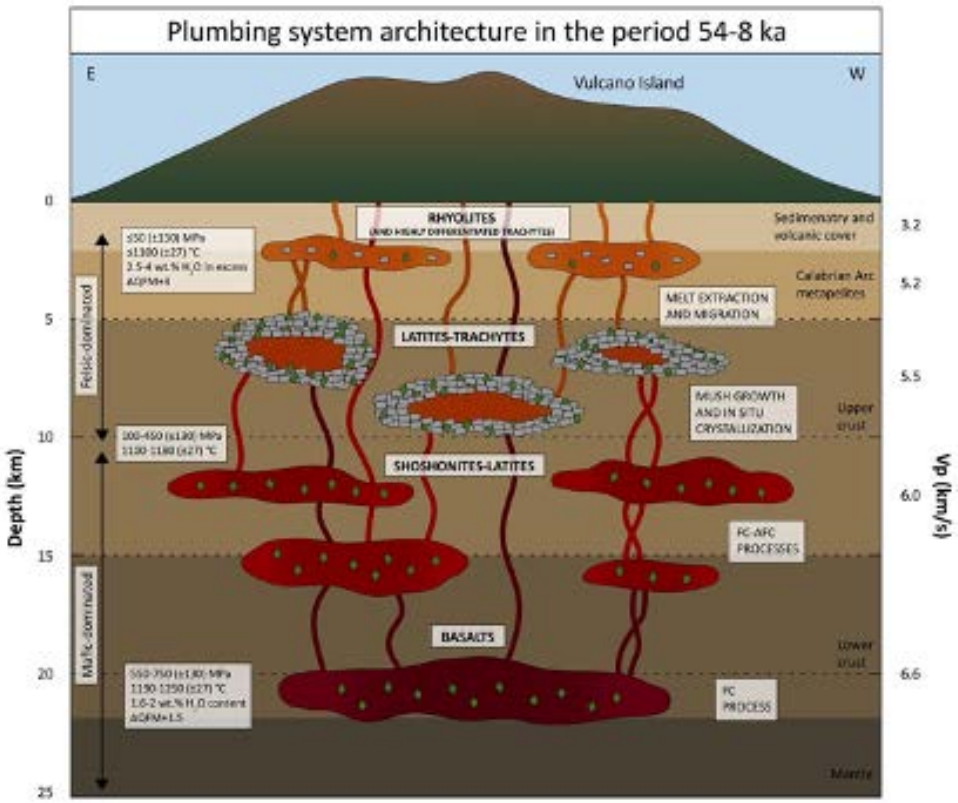

Fig. 1| Plumbing system architecture of Vulcano Island in the period 54-8 ka. A deep level of magma storage is located at depth 19 km and close to the Moho transition zone, hosting hot (1,190-1,250 °C), H_2O undersaturated (1.6-2.0 wt.%) basaltic melts. Shallower shoshonitic-latitic reservoirs and latitic-trachytic crystal mushes are located between 5.5 and 16 km of depth, crystallizing at temperature between 1,100 and 1,180 °C. Rhyolitic reservoirs, at about 2 km of depth, are prevalently generated by extraction of evolved melts from crystal mushes. Rhyolitic melts stall at temperatures lower than 1,100 °C and close to H_2O (2.5-4.0 wt.%) saturation.

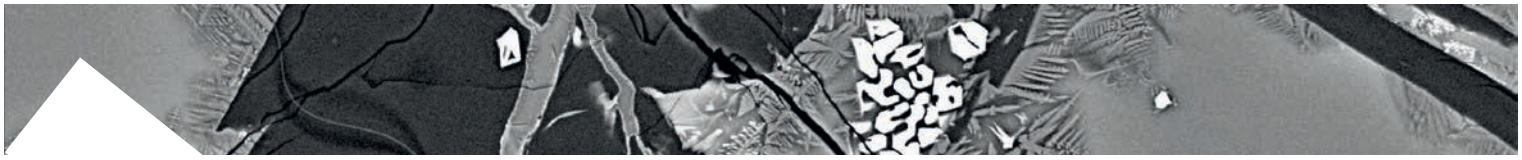

A review of the lattice strain and electrostatic effects on trace element partitioning between clinopyroxene and melt: Applications to magmatic systems saturated with Tschermak-rich clinopyroxenes

Mollo S., Blundy J., Scarlato P., Vetere F., Holtz F., Bachmann O., Gaeta M.

The partitioning energetics controlling the crystal-melt exchange are described by two distinct but complementary contributions: Gpartitioning = Gstrain + Gelectrostatic. Gstrain is the excess of strain energy quantifying the elastic response of the crystallographic site to insertion of trace cations with radius different from that of the major cation at the site. Gelectrostatic is the excess of electrostatic energy requiring that an electrostatic energy penalty is paid when a trace cation entering the lattice site without strain has charge different from that of the resident cation. Lattice strain and electrostatic parameters for different isovalent groups of cations hosting the same lattice site from literature have been discussed in comparison with new partitioning data measured between Tschermak-rich clinopyroxenes and a primitive phonotephritic melt assimilating variable amounts of carbonate material. Through such a comparatively approach, we illustrate that the type and number of trace cation substitutions are controlled by both charge-balanced and -imbalanced configurations taking place in the structural sites of Tschermak-rich clinopyroxenes. A virtue of this complementary relationship is that the control of melt composition on the partitioning of highly charged cations is almost entirely embodied in the crystal chemistry and structure, as long as these crystallochemical aspects are the direct expression of both Gstrain and Gelectrostatic. A size mismatch caused by cation substitution is accommodated by elastic strain in the surrounding lattice of clinopyroxene (Figure 1), whereas the charge mismatch is enabled via increasing amounts of charge-balancing Tschermak components, as well as the electrostatic work done on transferring the trace cations from melt to crystallographic sites, and vice versa. The influence of the melt chemistry on highly-charged (3^+ and 4^+) cation partitioning is greatly subordinate to the lattice strain and electrostatic energies of substitutions, in agreement with the thermodynamic premise that both these energetic quantities represent simple-activity composition models for the crystal phase. The various charge-balanced and -imbalanced configurations change principally with aluminium in tetrahedral coordination and the clinopyroxene volume change produced by heterovalent cation substitutions. In contrast, for low-charged (1^+ and 2^+) cations, the role of melt chemistry cannot be properly deconvoluted from the structural changes of the crystal lattice. The incorporation of these cations into the clinopyroxene lattice depends on the number of structural sites critically important to accommodating network-modifying cations

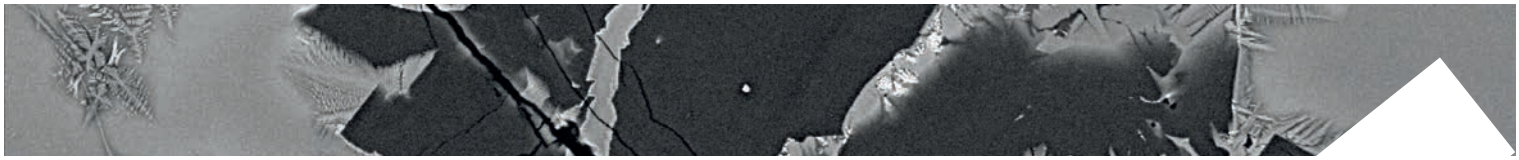

in the melt structure, implying that the partitioning energetics of monovalent and divalent cations are strictly controlled by both crystal and melt properties.
We conclude that the competition between charge-balanced and charge-imbalanced substitutions may selectively change the ability of trace elements to be compatible or incompatible in the clinopyroxene structure, with important ramifications for the modeling of natural igneous processes in crustal magma reservoirs which differentiate under closed- and open-system conditions.

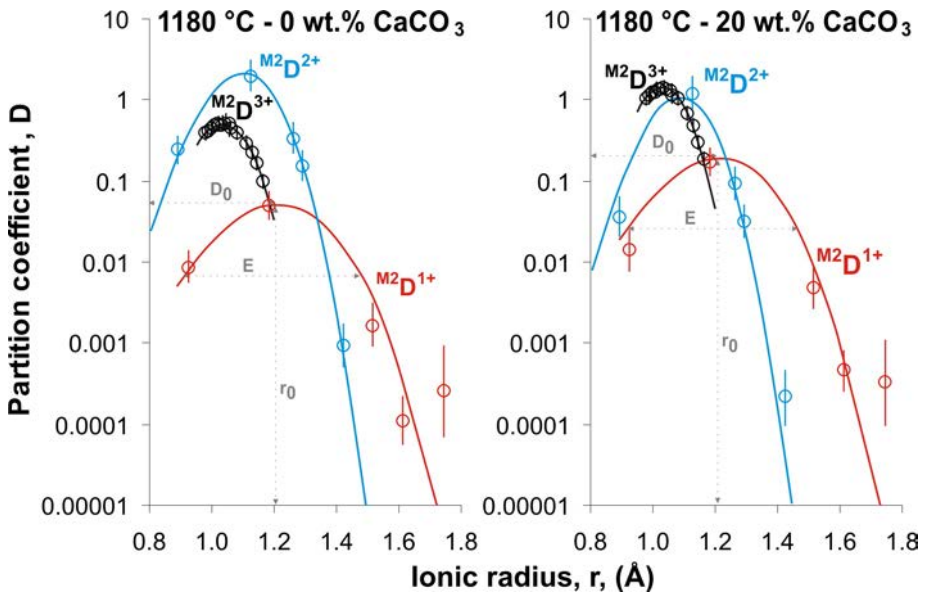

Fig. 1 | Example of lattice strain parabolas for monovalent, divalent and trivalent cations in M2-site modeled according to the lattice strain equation. Data refers to experiments conducted at 1,180 °C and doped with 0 and 20 wt.% $CaCO_3$

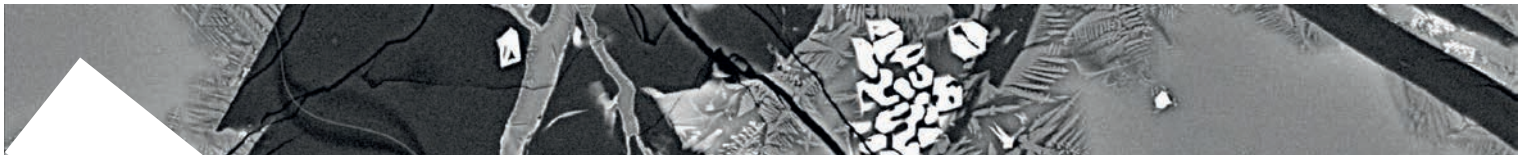

Zoned clinopyroxene crystals as tracers of magmatic components involved in mixing/mingling processes occurred in the plumbing system of Zaro (Ischia island, Italy)

Pelullo C., Arienzo I., Chakraborty S., D'Antonio M., Dohmen R., Nazzari M., Pappalardo L., Petrosino P.

In the framework of the "*Timescales of magmatic processes*", detailed mineral compositions have been obtained along transects of length varying from 20 µm to 800 µm, on zoned clinopyroxene crystals of selected eruptive products, belonging to the Zaro lava complex (<7 ka; Ischia island, South Italy). This project involves a collaboration between INGV, the Department of Earth, Environment and Resources Sciences of the University of Naples Federico II and the Institute of Geology, Mineralogy und Geophysics of the Ruhr-Universität (Bochum, Germany).The main Zaro lava body is trachyte and hosts abundant mafic to felsic enclaves, whose chemical and isotopic characteristics suggest mixing/mingling processes occurred before eruption.
A selection of zoned clinopyroxene crystals from both host lava and enclaves was thus analyzed by acquiring major and minor elements (Si, Ti, Al, Fe, Mg, Mn, Ca, Na, K, Ni and Cr; Figure 1a) along core-to-rim or rim-to rim transects crosscutting the centers of crystals (Figure 1b). The data were collected at the HP-HT Laboratory of Experimental Volcanology and Geophysics of INGV in Rome (Italy), using a Jeol-JXA8200 electron microprobe equipped with five wavelength dispersive spectrometers.
The zoning pattern of the Zaro clinopyroxene consists of two or more plateaus with a constant composition separated by either sharp or gradual boundaries (Figure 1c). The 83% of crystals are characterized by reverse zoning, whereas only 17% of crystals show normal zoning. Different compositional populations can be recognized in the whole variation of the chemical composition of the Zaro clinopyroxenes (Figure 1d), with significant differences among clinopyroxene of the various lithotypes; e.g. the most mafic components (high Mg#) have been detected almost exclusively in mantles of clinopyroxenes belonging to the less evolved enclaves (Figure 1a-c).
Each compositional population can be attributed to a specific set of magmatic variables, which represent a defined magmatic environment (ME; Figure 1d). Clinopyroxene-liquid thermometers and barometers have been used in order to investigate the crystallization conditions of the different magmatic environments detected in the Zaro clinopyroxenes. The investigation of relationships among the magmatic environments enables to: 1) accurately characterize the magmatic component (end-members) involved in the mingling/mixing process and 2) precisely record fluctuations inside the Zaro magmatic system.

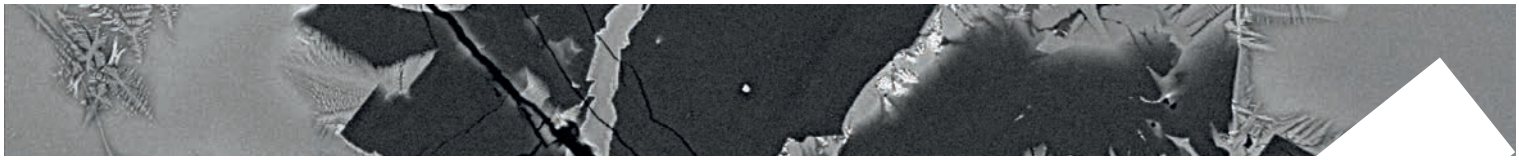

Lastly, the application of different diffusion modelling approaches allowed estimating the timescales over which the processes that created the zoning occurred.

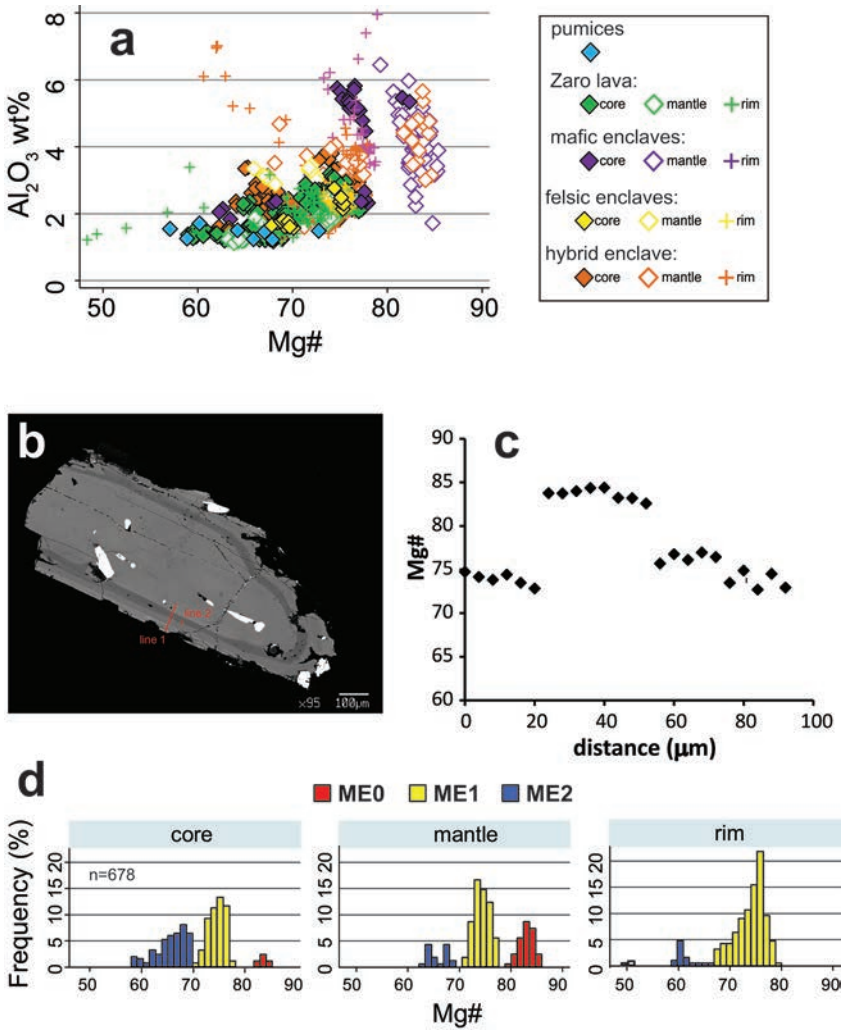

Fig. 1l a) Mg# vs Al_2O_3 (wt%) variation diagram for clinopyroxene crystals belonging to different lithotypes of the Zaro eruptive complex; b) BSE image of a clinopyroxene crystal from Zaro eruption; c) Mg# variation along the line 1 of the clinopyroxene crystal in Fig.1a; d) Mg# frequency histograms of core, mantle and rim of the Zaro zoned clinopyroxenes

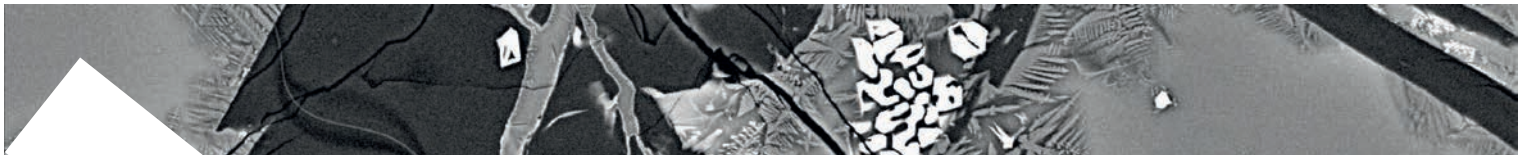

Jadeite and Ca-Tschermak decoupling in clinopyroxene as a function of depth: Implications for trace element partitioning through the plumbing system at Mt. Etna

Mollo S., Ubide T., Di Stefano F., Nazzari M., Scarlato M.

We present elemental maps and intra-crystal compositional profiles conducted on a representative clinopyroxene phenocryst from the 1974 eccentric lava flows at Mt. Etna volcano (Sicily, Italy).
This eruption was fed by deep-seated magmas ascending through pathways bypassing the central volcanic conduits. Mafic recharge episodes are recorded by the complex textural features of the clinopyroxene, showing a subrounded core enclosed within a concentrically zoned mantle. The core is enriched in $Mg^{+}Fe^{2+}Na^{+}$ and depleted in $Fe^{3+}Ca^{+}$ relative to the mantle. The jadeite (Jd) component decreases from core to mantle and is counterbalanced by higher Ca-Tschermak (CaTs) contents, as the number of TAl cations in tetrahedral coordination increases. Jd-rich core incorporates high proportions of rare earth elements and Y (REE+Y) and low concentrations of high field strength elements (HFSE) and transition elements (TE), whereas the opposite occurs for the CaTs-rich mantle. This marked decoupling between trivalent cations in the M2 site and heterovalent cations in the M1 site is due to the inverse Jd-CaTs relationship, testifying to polybaric-polythermal magma crystallization conditions. Coherently, thermobarometric calculations indicate that the early-formed Jd-rich core equilibrated with the host magma at mantle depths (750-950 MPa and 1,190-1,210 °C), whereas the later CaTs-rich mantle formed at shallow crustal levels (400-700 MPa and 1,150-1,180 °C) after magma recharge. Quantitative modeling of apparent cation partitioning (Di) indicates that higher TAl cations in CaTs-rich mantle promote lattice strain and electrostatic compensation effects to maintain local charge electroneutrality. D_{HFSE} and D_{TE} increase from Jd-rich core to CaTs-rich mantle, obeying to local charge-balanced/imbalanced configurations where highly charged cations enter the M1 site more easily to balance the charge deficit left by the replacement of Si for TAl. On the other hand, DNa increases with increasing pressure, due to the higher solubility of Jd in clinopyroxene crystal lattice. The values of D_{REE+Y} also increase up to one order of magnitude at the Jd-rich core due to the enhanced stability of the $Na_{0.5}REE+Y_{0.5}MgSiO_6$ end-member, prompted by Ca-Na substitutions. Using D_{REE+Y} measured across the core-mantle interface, we constrain the geochemical evolution of recent (2000-2013) magmas at Mt. Etna volcano by Rayleigh fractional crystallization. Results indicate that magma dynamics proceed via a stepwise polybaric-polythermal process accounting for 1) crystallization of Jd-rich clinopyroxenes at high-P, high-T conditions and 2) upward migration of crystal-bearing

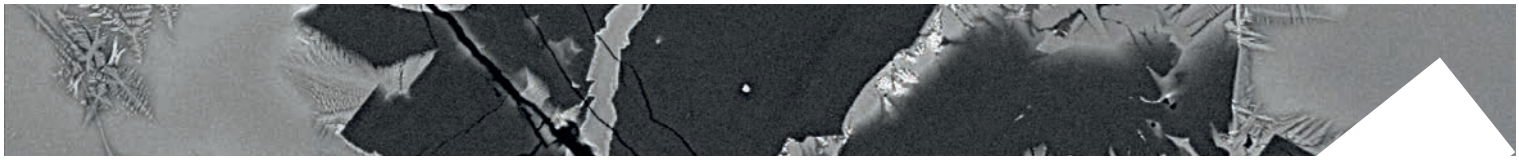

magmas due to replenishment phenomena with input of fresh magmas, crystallizing CaTs-rich clinopyroxene in low-P, low-T reservoirs. Intriguingly, the total amount (~15 vol.%) of clinopyroxene formed at depth is much lower than that (at least 25 vol.%) quantified at shallow crustal levels. Abundant crystallization and accumulation phenomena at low-P, low-T conditions are needed to explain the typical crystal cargoes in Etnean magmas, and can be easily related to enhanced crystallization by degassing and cooling phenomena at shallow depths. These results are in good agreement with geophysical signals suggesting the presence of highly crystalline magmatic bodies at shallow to intermediate crustal levels below Mt. Etna.

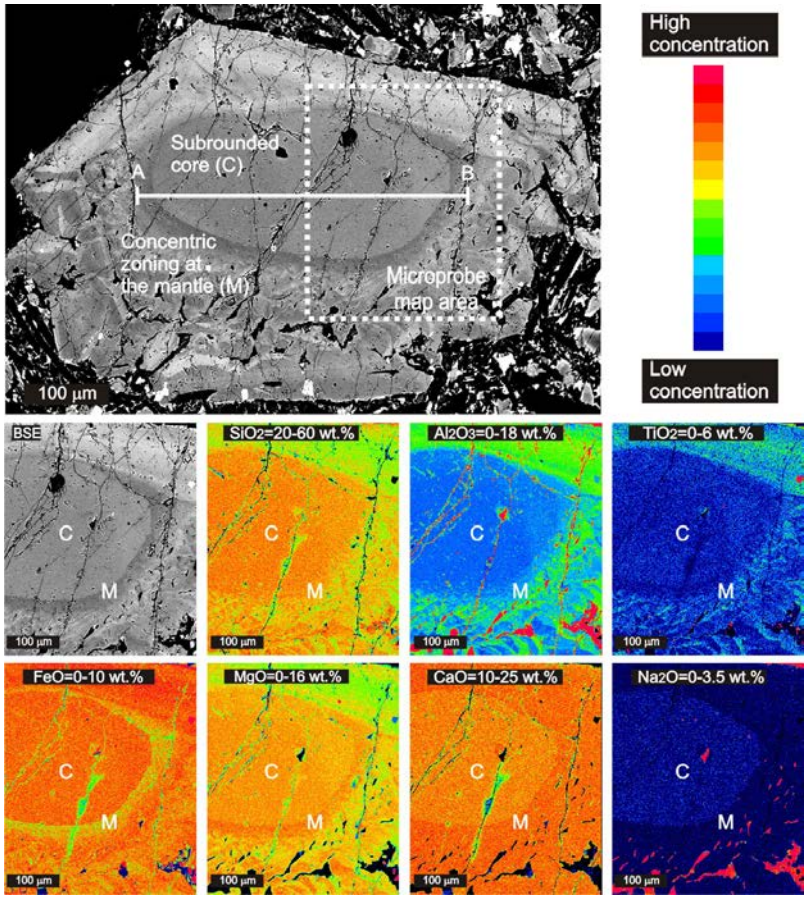

Fig. 11 Backscattered electron (BSE) imaging and electron microprobe mapping of the studied 1974 Etna clinopyroxene phenocryst. The grayscale and false-color compositional images illustrate the distinctively large subrounded core (C) enclosed within a concentric zone from which the crystal mantle (M) develops.

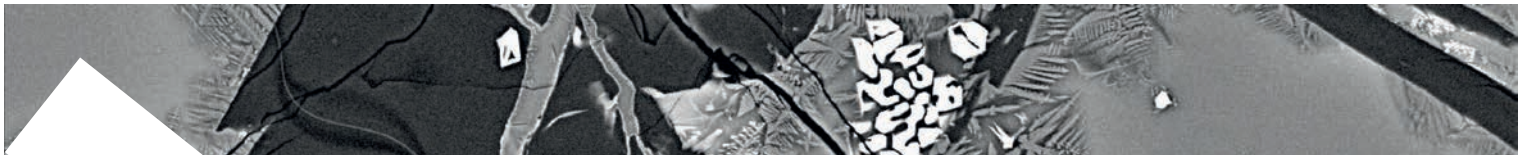

The onset and solidification path of a basaltic melt by in-situ Differential Scanning Calorimetry (DSC) and ex-situ investigations

Giuliani L., Iezzi G., Hippeli T., Davis M., Elbrecht A., Vetere F., Nazzari M., Mollo S.

To investigate the kinetic solidification path of basaltic systems, a tholeiitic MORB has been heated at 420 °C/h in a differential scanning calorimetry (DSC), from ambient T to 1,300 °C (*superliquidus*), at P and fO_2 of air. After a dwell time of 2 h at 1300 °C, the melt was cooled at rates ($\Delta T/\Delta t$) of 7, 60, 180, 1,000 and 1,800 °C/h, up to the quenching at 800 and 600 °C. The acquisition of the *in-situ* DSC spectra allows to measure the T_g (the glass transition temperature) and T_m (the melting temperature) during heating, and T_x (the onset of crystallization) both on heating and cooling. The values of T_g and T_m are almost close to 700 and 1,200 °C, while Tx progressively decreases as the $\Delta T/\Delta t$ increases. The DSC-spectra of the runs at 7 and 60 °C/h display a single asymmetric peak that evolves to a two-component path at 180-1,000 and 1,800 °C/h. The paragenesis of the run products is clinopyroxene (cpx), spinel (sp) and melilite (mel); plagioclase (plg) nucleates only at 7 °C/h with tiny sizes and skeletal-like shapes. Textural and chemical features of all crystals have been quantified ex-situ, combining SEM and EPMA analysis. Generally, the increase of $\Delta T/\Delta t$ causes a slight increment of the crystal content (area%) from 7 to 1,800 °C/h. Faceted sp are present in all the run products with an amount always < 2 area%. Cpx increases from 7 to 1,800 °C/h, changing its texture from almost faceted to dendritic between 60 and 180 °C/h. The area% of mel follows an asymmetric Gaussian trend, while plg nucleates only at 7 °C/h with a content < 2 area%. The CSDs - analyses suggest multiple nucleation events and crystal growth by coarsening at $\Delta T/\Delta t \geq$ 60 °C/h. Parallelly, maximum and minimum growth rates (Gmax and GCSD) were estimated for cpx and sp using the crystallization time directly measured in-situ on the DSC-spectra. Both the Gs parameters increase with the increasing of $\Delta T/\Delta t$.

The onset of nucleation (T_{xi}) has been computed also considering the temperature-values at the 10% of the maximum intensity of the first peak base. In this manner, we found both a linear (R_2 = 0.97) and exponential functions (R_2 = 0.99) that analytically describe the kinetic decreasing of T_{xi}. These functions allow us to determine the values of T_{xi} at any cooling-rates condition. The plot of T_{xi} versus time reflects the uppermost portion of a typical TTT trend (Figure 1). This analytical model allows to quantitatively model the kinetic crystallization paths of dry basalts.

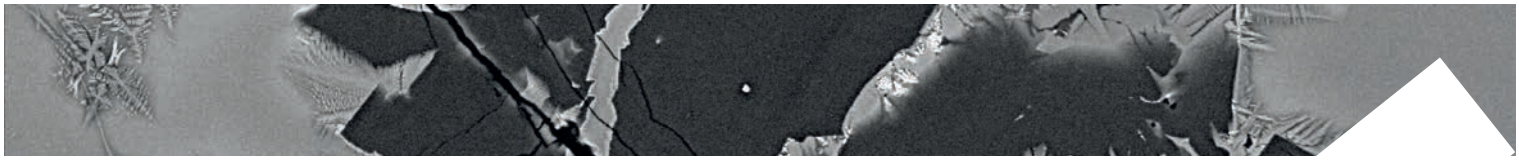

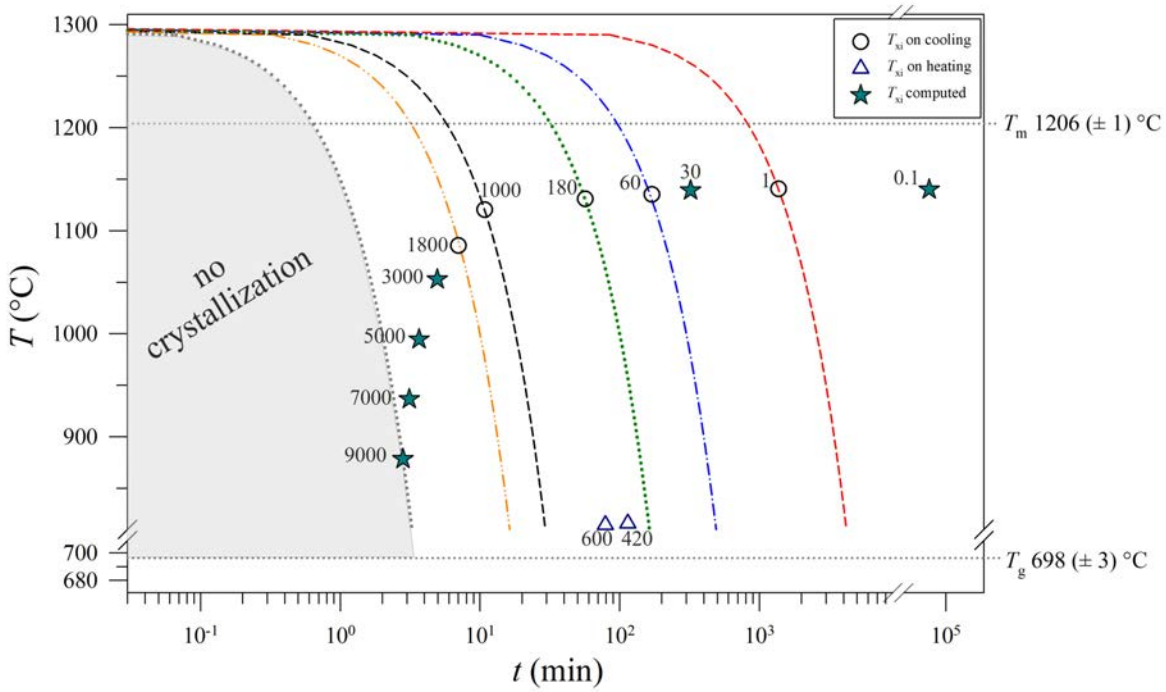

Fig. 1 | Backscattered electron (BSE) imaging and electron microprobe mapping of the studied 1974 Etna clinopyroxene phenocryst. The grayscale and false-color compositional images illustrate the distinctively large subrounded core (C) enclosed within a concentric zone from which the crystal mantle (M) develops.

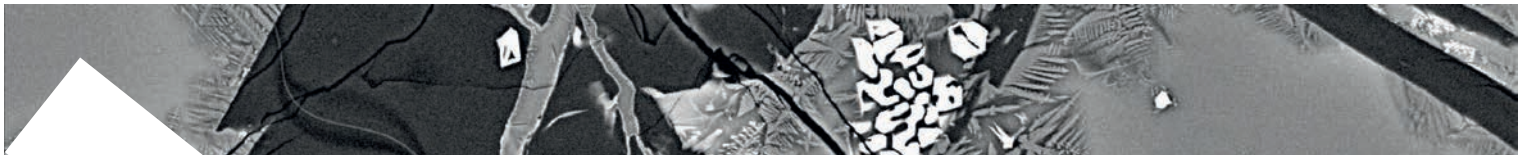

Chemical variations of clinopyroxene, spinel and plagioclase solidified at variable cooling rates from a MORB liquid revealed by X-Ray chemical mapping

Giuliani L., Iezzi G., Nazzari M., Vetere F., Mollo S., Scarlato P.

X-Ray chemical maps were performed to quantify accurately chemical variations of plagioclases (plg), clinopyroxenes (cpx) and spinel (sp) solidified in a MORB liquid (1,300 down to 800 °C, P and f_{O_2} of air) under variable cooling rates ($\Delta T/\Delta t$) of 1, 7, 60, 180, 1,800 and 9,000 °C/h. At $\Delta T/\Delta t \leq 60$ °C/h the run products are holocrystalline, while > 60 plg disappears and crystal shapes switch between faceted to dendritic. The increase of $\Delta T/\Delta t$ determines a decrease of crystal content (area%) and sizes (µm); accordingly, mapped areas were performed on run-products solidified from 1 to 180 °C/h. The EPMA-maps were acquired with step scans of 2/4 µm and 120–20 ms on peak and background, respectively, covering areas between 1000 to 500 μm^2. The resulting maps are shown in Fig. 1; FeO was split in two different maps due to its strong variation in plg, cpx and glass (FeO ≤ 15 wt.%) versus sp (50 < FeO ≤ 70 wt.%).
The Al_2O_3 and CaO contents in plg decrease when $\Delta T/\Delta t$ increases favoring more albitic composition. In parallel, when $\Delta T/\Delta t$ increases the MgO content decreases and those of CaO and FeO augment in cpx. By contrast, a defined evolution of FeO and TiO_2 contents as a function of $\Delta T/\Delta t$ is lacking (Figure 1).
On the whole, the SiO_2 amount slightly increases as a function of $\Delta T/\Delta t$, mirroring the increasing of glass amount (0 to 43 area%).
The acquired X-Ray chemical maps could represent the merging point between the textural and crystal-chemical features and their quantitative variations as a function of kinetics. This has important implications to quantitatively model the solidification conditions of dry basaltic melts.

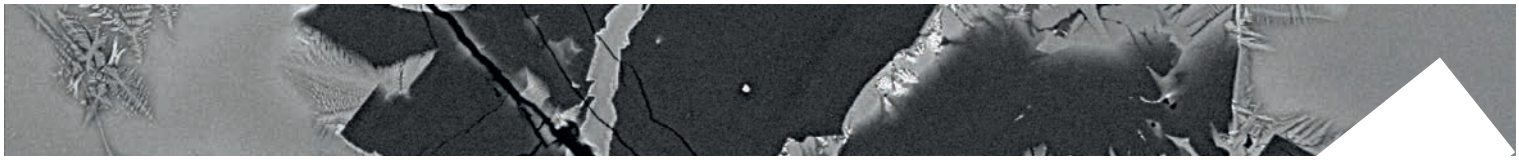

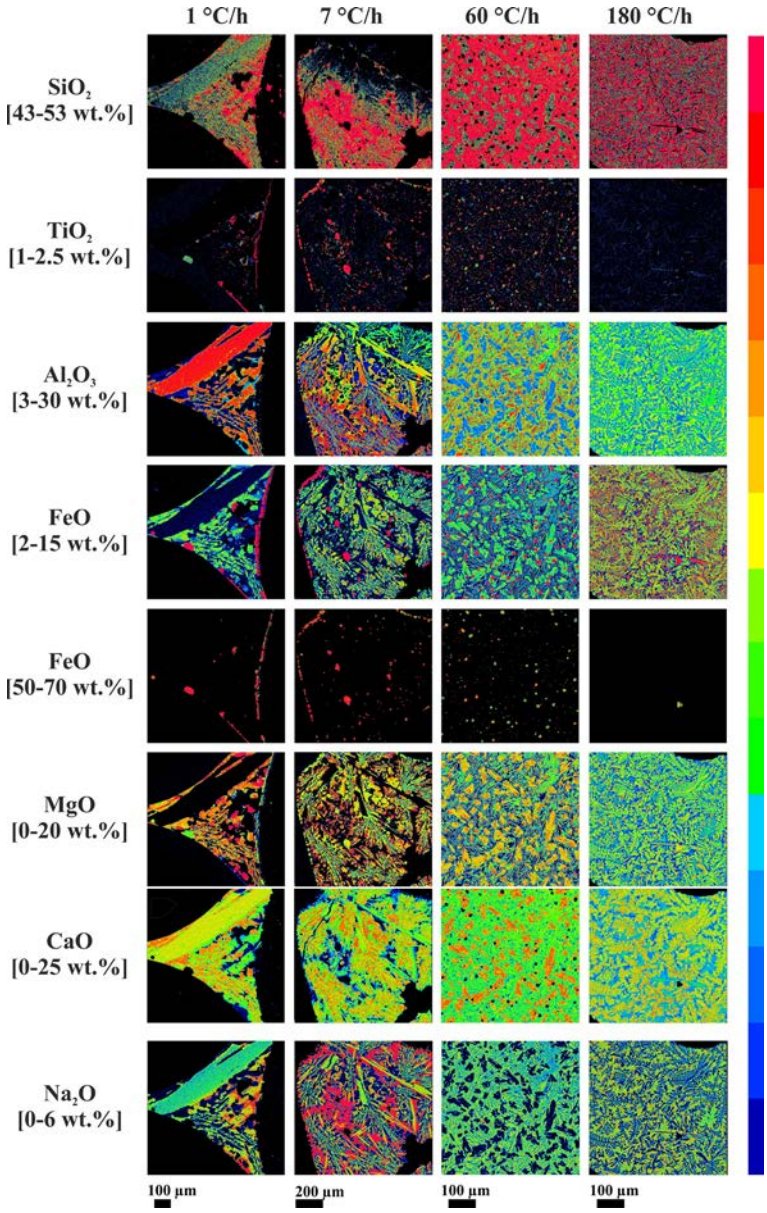

Fig. 1l X-Ray chemical maps of major oxides in plg, cpx and sp as a function of $\Delta T/\Delta t$. Range of each oxide corresponds to minimum versus maximum amounts measured in all the run-products, quantified via a single-analytical point. FeO is reported in two amps due to its high variation in plg, cpx plus glass (2 – 15 wt.%) versus sp (50 – 70 wt.%).

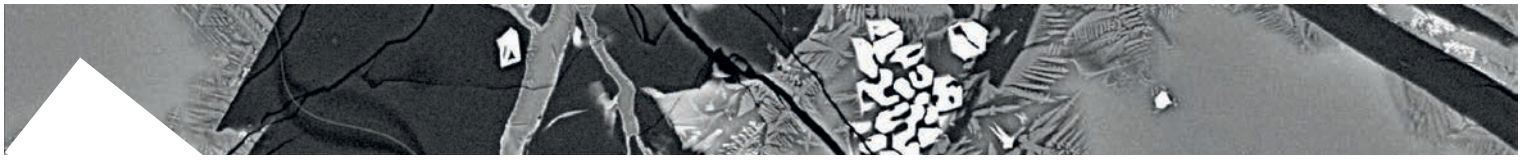

Basaltic crystal cargoes reveal alkalinity modulated by a lithospheric mantle filter in the intraplate Dunedin Volcano (New Zealand)

Pontesilli A., Brenna M., Ubide T., Mollo S., Masotta M., Caufield J., Nazzari M., Scott J.M., Scarlato P.

Systematic variations in the crystal cargo and whole rock isotopic compositions of primitive components reveal a complex mantle-to-crust polybaric plumbing system in the intraplate Dunedin Volcano (New Zealand). Basaltic rocks define a compositional spectrum from low-alkali basalts through mid-alkali basalts to high-alkali basalts. High-alkali basalts display clinopyroxene crystals with sector (hourglass) and oscillatory zoning ($Mg^{\#}_{65-82}$) as well as Fe-rich green cores ($Mg^{\#}_{43-69}$), whereas low-alkali basalts are characterised by unzoned clinopyroxenes ($Mg^{\#}_{69-84}$) with resorbed mafic cores ($Mg^{\#}_{78-88}$), coexisting with reversely zoned plagioclase crystals (An_{43-68} to An_{60-84} from core to rim). Complex magma dynamics within a polybaric plumbing system are indicated by distinctive compositional variations of clinopyroxene macrocrysts, such as Cr-rich zones and resorbed cores with $Mg^{\#}_{74-88}$, indicating continuous recharge by more mafic magmas. Crystallisation of olivine, clinopyroxene and titanomagnetite occurred from upper mantle to lower crustal depths (485-1059 MPa and 1,147-1,286 °C), whereas crystallisation of plagioclase with subordinate clinopyroxene and titanomagnetite proceeded at shallower crustal levels. The compositions of high-alkali basalts and mid-alkali basalts resemble ocean island basalts and are characterised by FOZO-HIMU isotopic signatures ($^{87}Sr/^{86}Sr_i$ = 0.70277-0.70315, $^{143}Nd/^{144}Nd_i$ = 0.51286-0.51294, and $^{206}Pb/^{204}Pb$ = 19.348-20.265), whereas low-alkali basalts have lower incompatible element abundances and isotopic compositions trending toward EMII ($^{87}Sr/^{86}Sr_i$ = 0.70327-70397, $^{143}Nd/^{144}Nd_i$ = 0.51282-0.51286, and $^{206}Pb/^{204}Pb$ = 19.278-19.793). High- and mid-alkali basalts crystallised in the lower crust, whereas low-alkali basalts recorded upper mantle clinopyroxene crystallisation. The variable alkalinity and isotope composition may result from interaction of low-alkaline melts derived from the asthenosphere with melts derived from lithospheric mantle, possibly initiated by the asthenospheric melt percolation. The transition to more alkaline compositions is accomplished by the lower degree of melting of metasomatic lithologies in the lithospheric mantle, leading to eruption of predominantly small-volume, high-alkali magmas at the periphery of the volcano. Moreover, the lithosphere imposed a filtering effect on the alkalinity of intraplate magmas. As a consequence, the eruption of low-alkali basalts of asthenospheric origin was prevalently concentrated at the centre of the volcano, where the plumbing system was more developed.

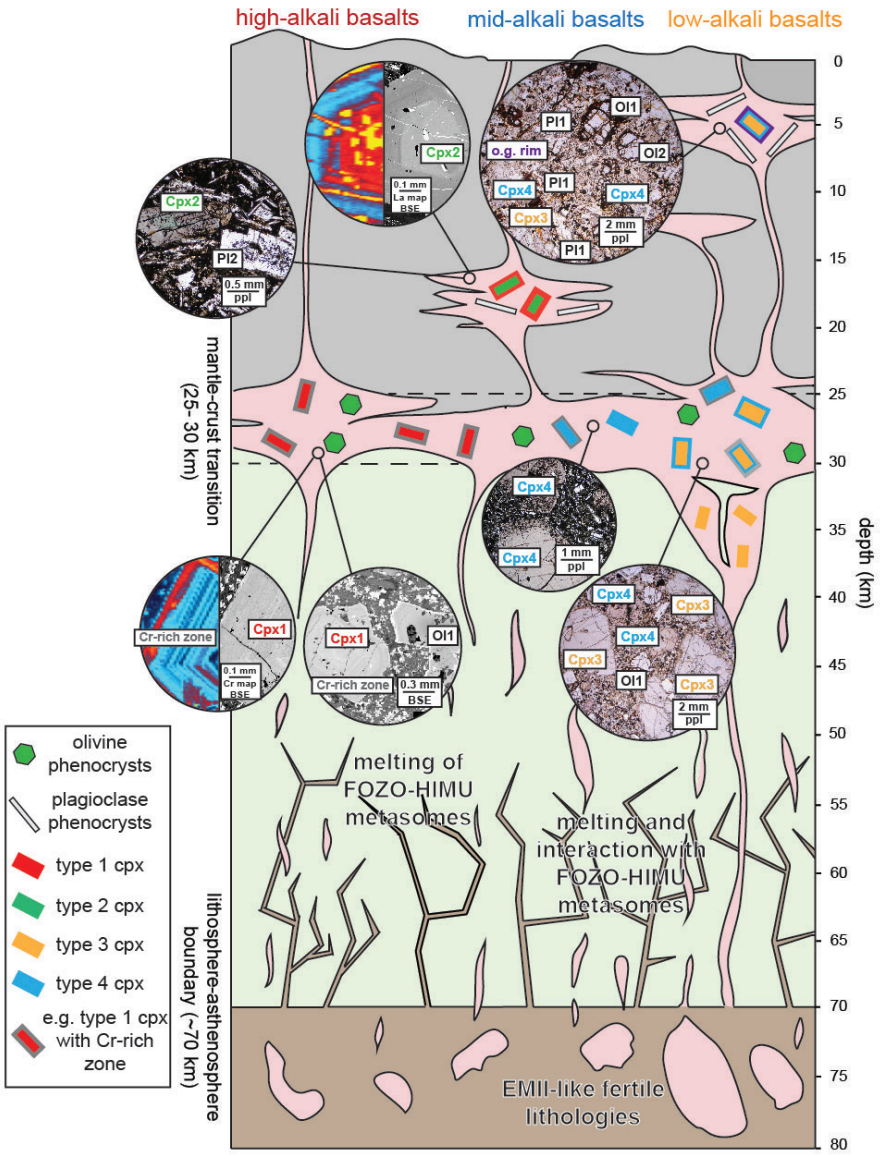

Fig. 1| Schematic representation of the complex plumbing system envisaged for the Dunedin Volcano. Different clinopyroxene types are distinguished according to the colour legend, while no colour distinctions are made for olivine and plagioclase crystals. Inset BSE photomicrographs and trace elements maps display the main textural features of low-, mid-, and high-alkali basalts. From left to right, higher degrees of interaction between asthenospheric derived melts and the lithospheric mantle generate peripheral high-alkali basalts. The increasing petrographic complexity of the crystalline cargo, with clinopyroxene green core type 2 and plagioclase type 2 from high- and mid-alkali basalts indicates the increasing development of the plumbing system at middle crustal depths, in the central sectors of the Dunedin Volcano. To the right, the central area of the volcano where low- and mid-alkali basalts were erupted, displays a more complex mantle to crust pathways, fed by inputs of asthenosphere-derived EMII-like melts.

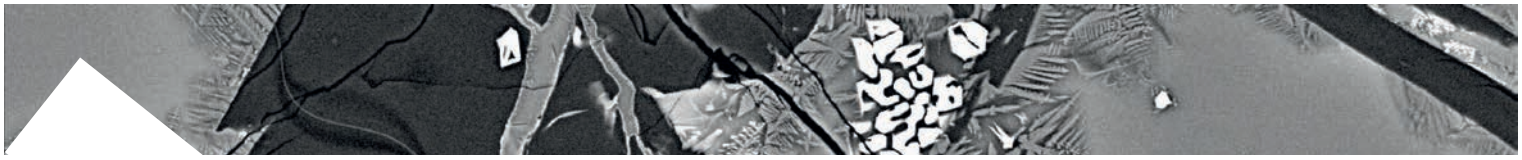

Experimental observation of seismo-acoustic harmonic tremor gliding during churn flow regime

Spina L., Cannata A., Morgavi D., Privitera E., Perugini D.

Harmonic tremor is a particular type of volcanic tremor, characterized by several regularly spaced spectral peaks and quite commonly observed at active volcanoes. The gradual evolution of spectral peaks, generating gliding lines on the spectrogram, known as "gliding", has been frequently reported and in several cases gliding tremor has been associated with explosive outbursts. Decoding such temporal variations of the spectral content of tremor has clear implications for both monitoring and research purposes, and depends on the assumed source model. Laboratory experiments, allowing for direct observation of degassing processes and of the related elastic radiation, are particularly helpful for constraining the generation mechanism of harmonic tremor and of associated gliding. Nonetheless, experimental observations on harmonic gliding tremor are lacking. We aim to fill this gap by providing a detailed analysis on gliding episodes and related source processes generated during scaled degassing experiments.
Our observation builds on the experimental dataset described in Spina et al. (2019).
The experiments consisted in reproducing different degassing regimes (from bubbly flow to slug and churn-annular flow) by injecting controlled air flux (5-180x10^{-3} l/s) in analogue conduits with variable roughness (fractal dimension changing from 2, 2.18 and 2.99) and analogue magma viscosity (10, 100 and 1000 Pas). The elastic radiation generated by degassing processes during the experiments was recorded by an accelerometer ICP J352C33 model (PCB Piezotronics; sensitivity of 0.1 V/g in the band 0.5–10,000 Hz) and a microphone ICP 378B02 model (PCB Piezotronics; sensitivity of 50 mV/Pa in the band 7–10,000 Hz). Both signals were acquired at a sampling rate of 50 kHz. A video-camera recording at 25 fps allowed for visual quantification of degassing patterns at different time steps. Spectral analyses (Short-Time Fourier Transform) performed on a 1-s-long sliding window, with an overlap of 0.9 s allowed visualization of tremor gliding. Several gliding episodes were investigated in detail to determine: i) which sets of experimental variables (and therefore degassing conditions) mostly affect gliding occurrence; ii) the most appropriate source model matching experimental observations. Acoustic signals exhibited the clearest gliding episodes and were taken as reference for manual picking of frequency for different harmonics at increasing time-steps. Interpolation of the obtained series allowed for a common time-frame.
In most cases gliding is related to the dominant set of harmonics featuring a positive trend; a secondary set of harmonics with smaller spectral amplitude and a negative

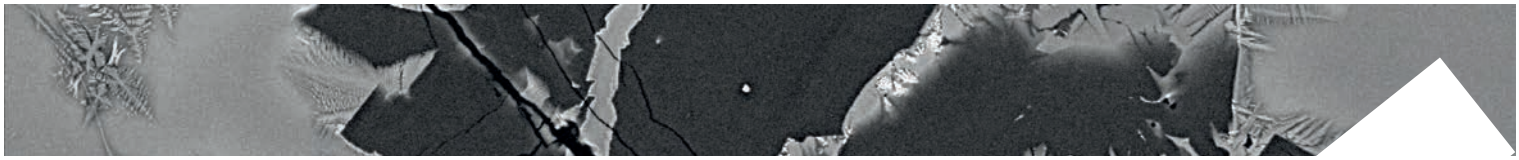

gliding trend was also observed. The clearest and more stable patterns of harmonic gliding were observed at intermediate-high viscosity and flux. The information on the temporal evolution of acoustic signals was compared against quantitative information on the degassing pattern from video analysis. Harmonic tremor gliding was mostly observed during churn-annular flow. Hence, we measured at different time steps i) the position of the termination and ii) the length of each churn unit. Finally, we tested the validity of a model based on the resonance of individual churn units. We assumed that a churn unit resonates as a closed-closed pipe resonator. Then, we first averaged the frequency spacing on the spectrogram between consecutive harmonics at each time step. Successively, we calculated the average length of the resonator L from the average spacing at a given time-step Δf by the following equation: $L=v/(2*\Delta f)$. The latter was compared against the temporal evolution of churn unit lengths. As shown in Figure 1, the modelled resonator length closely resembles the curve tracing the time evolution of the shallowest churn unit. Additionally, we observed that secondary sets of harmonics of smaller amplitude and negative gliding trend replicate the temporal progression of the length of the second to last churn units. This suggests that the progressive volume variation of the shallowest gas pockets in churn flow regime represents a valid source model for tremor gliding.

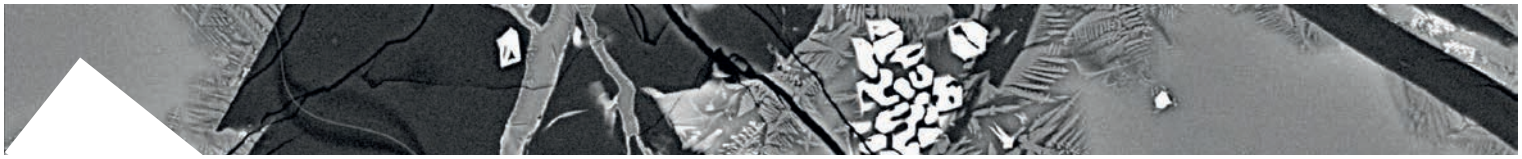

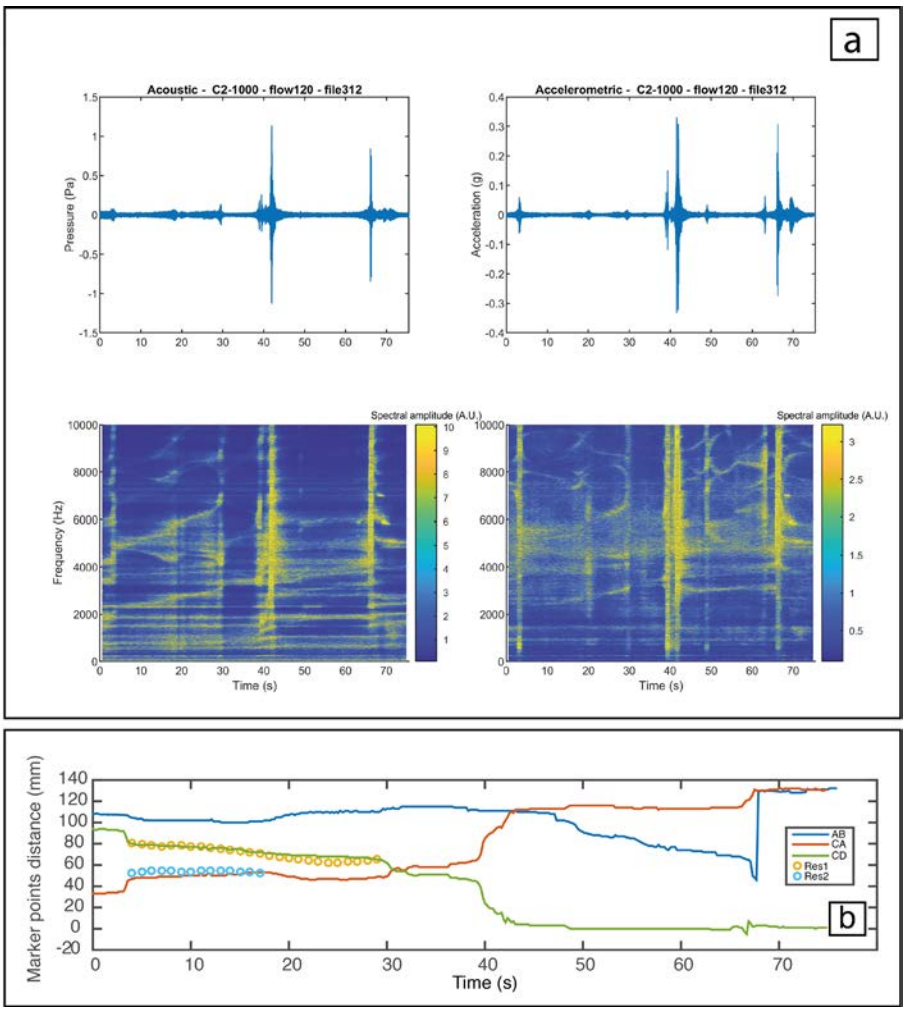

Fig. 11 a) Acoustic (left side top and bottom panels) and accelerometric (right side top and bottom panels) signals and short-time Fourier Transform of run 312 (viscosity 1000 Pa s, gas flux $120x10^{-3}$ l/s, conduit roughness equal to fractal dimension of 2). Spectral gliding lines are visible in both panels. b) Temporal evolution of the length of different churn units (AB, CA and CD) relative to run 312. Orange and blue dots represent the temporal progression of the length of the theoretical resonator (see the text for more details).

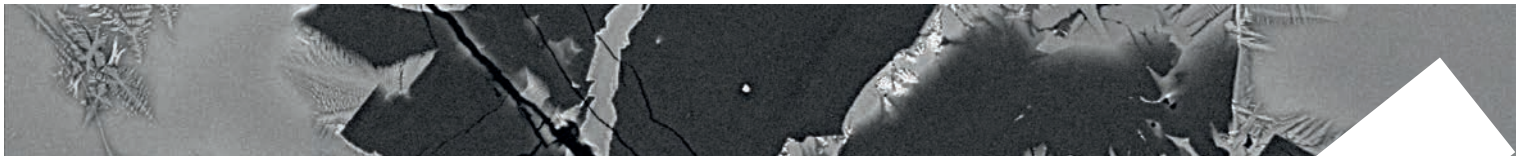

Field-based measurements of volcanic ash resuspension by wind

Del Bello E., Taddeucci J., Merrison J.P., Rasmussen K.R., Andronico D., Ricci T., Scarlato P., Iversen J.J.

The resuspension of volcanic ash by wind is a significant source of hazard during and after volcanic eruptions. Parameterizing and modeling ash resuspension requires direct measurement of the minimum wind shear stress required to move particles, usually expressed as the threshold friction velocity U*th, a parameter that, for volcanic ash, has been measured only scarcely and always in the laboratory. Here, we report the first field measurements of U*th for volcanic ash, with a portable wind tunnel specifically developed, calibrated, and tested. Field measurements, performed on natural reworked ash deposits from Sakurajima (Japan) and Cordón Caulle (Chile) volcanoes, agree well with our laboratory determinations on ash from the same deposits, with values of U*th ranging from 0.13 to 0.38 m/s. Our results show that the median grain size of the deposit and particle shape have a stronger control on U*th than the local substratum nature and deposit texture. This study provides the first systematic attempt to parameterize how naturally reworked ash can be resuspended by wind. Our calibrated small, portable wind tunnel provided an easy and efficient way to quantify the threshold friction speed for initiation of volcanic ash particle motion, directly in the field. Our field-based measurements agree well with measurements performed in the laboratory, showing the interchangeability of field-and laboratory-based measurements. We also show that ash layers from different eruptions are resuspended differently by wind, depending less on the heterogeneity of the deposit and the variability of the substra-tum on which they rest and more on the size, density, and shape of the particles.

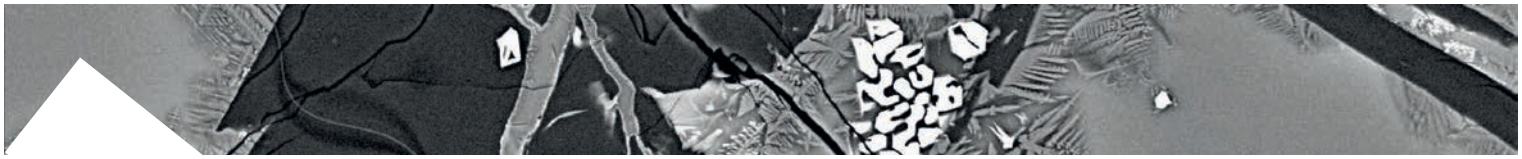

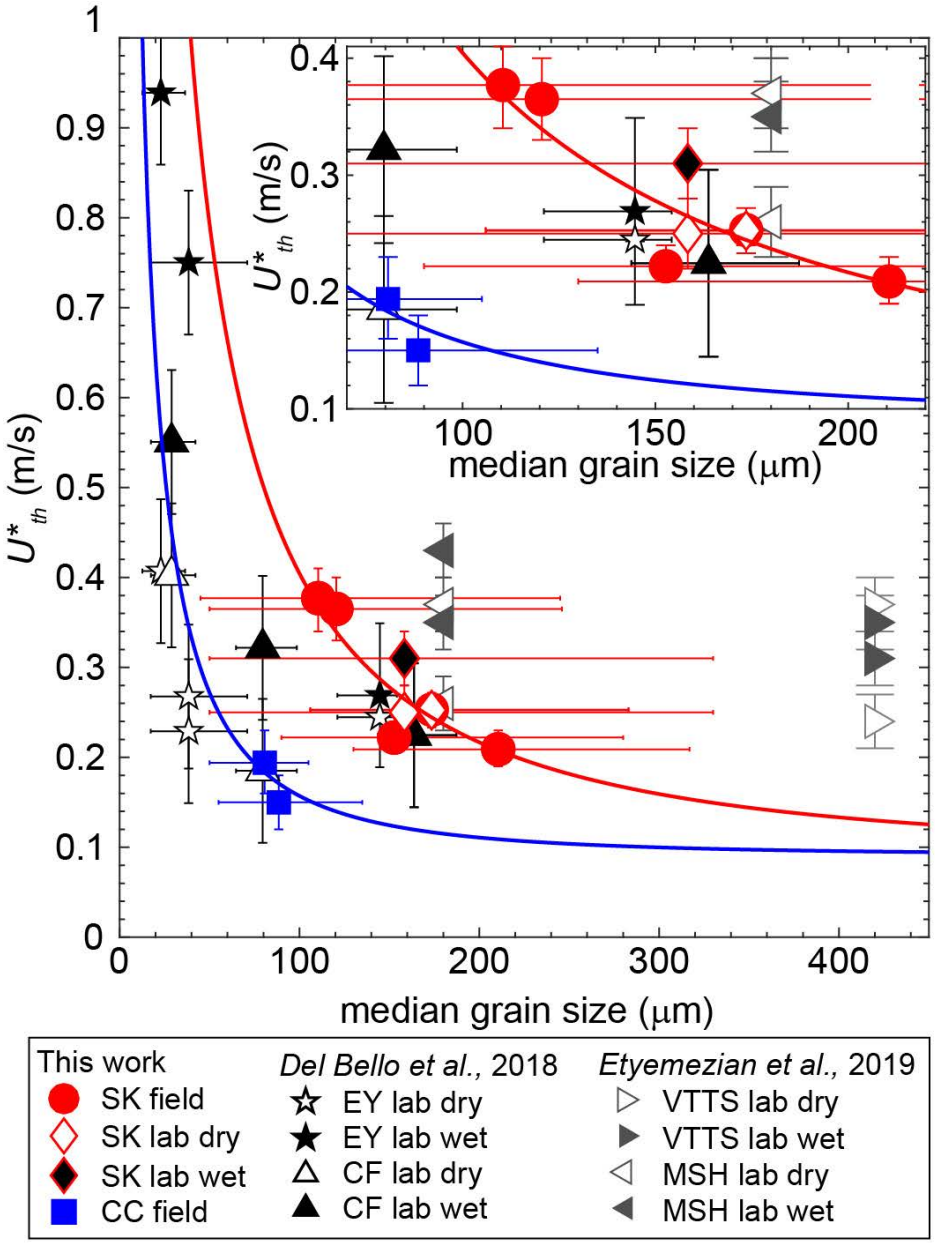

Fig. 1l a) U∗th values for Sakurajima (SK) and Cordón Caulle (CC) ash as a function of the median grain size distribution of our field experimental data (SK field and CC field), compared with our laboratory determinations (SK lab) and literature values. Horizontal and vertical error bars are the 25th-75thpercentiles of the grain size distribution and the RMSE of the calibration fit curve, respectively. Lines are force balance equation fits (Merrison et al., 2007) to SK (red) and CC (blue) ash deposits considering three fitting parameters (see text). Inset shows a closer view of the central part of the main panel.

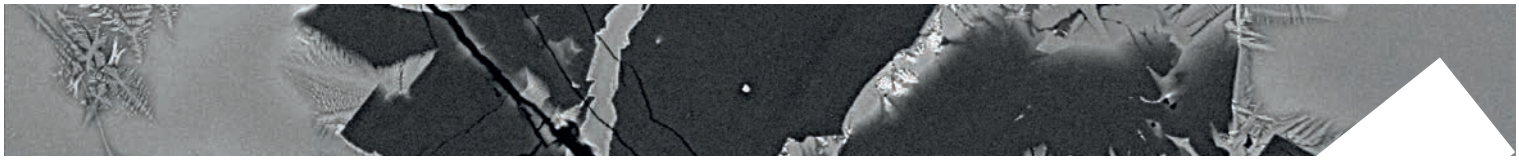

Space-time variations of ordinary explosive activity at Stromboli by high frequency IR thermal image analysis

Del Bello E., Falcone E., Taddeucci J., Scarlato P.

The persistent ordinary explosive activity observed at Stromboli consists of a plethora of phenomena. 'Normal' strombolian explosions are impulsive releases launching variable proportions of incandescent magma fragments, gas and ash, up to a few hundred meters high, with durations ranging from seconds to minutes. According to the dominant erupted component they range from pure gas (Type 0) to pure bomb (Type1) to pure ash (Type 3) explosions, with all gradations in between. According to the volatile phase volume and the frequency of impulses, gas rich explosions further range from puffing to rapid explosions occurring at multiple vents.
A systematic and temporal resolved analysis of normal explosive activity parameters is fundamental for understanding and modeling the relevant physical processes of its activity and for studying its changes. To this end, in this work, a database of Strombolian explosions is developed, obtained through direct and continuous observation of the eruptive vents at the summit craters through thermal infrared videos acquired at 50 Hz.
The data used, relating to continuous 1 to 5 hours long intervals recorded in 5 different days of 2019-2020, were processed and analyzed, also with algorithms developed in MatLab, in order to identify key eruptive parameters, such as height of the incandescent ballistics, the duration, the average speed of the pyroclasts exiting the eruptive vent, and the eruptive frequency. The analysis of the evolution over time of these parameters at the different vents has shown how the explosive activity diversifies across time and space and what are the interactions between different vents. Quantitative analysis has also made it possible to classify eruptive styles as well as their spatial and temporal distribution.
In particular, it was possible to document that the occurrence of a high frequency of occurrence per hour, a greater intensity of the explosions, the variation of eruptive styles, and the co-presence of an intense degassing activity could represent relevant indicators of a change the state of equilibrium of the volcanic system, to be subjected to even more stringent monitoring.

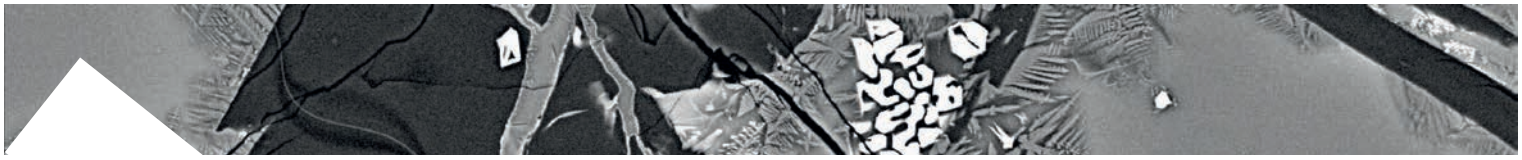

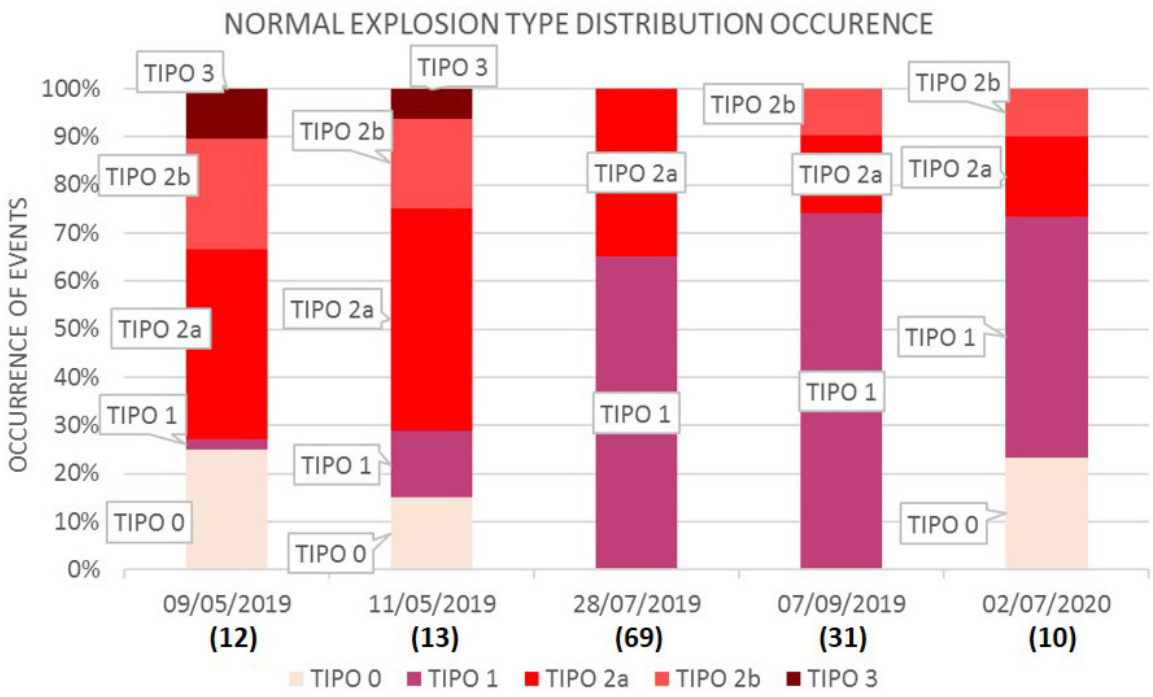

Fig. 1l : Distribution of normal explosion types observed for each day of thermal analysis. Explosion types are as follows: gas dominated (Type 0), bomb and gas dominated (Type 1), bomb and ash dominated (Type 2a) ash and bomb dominated (Type 2b), ash dominated (Type 3).

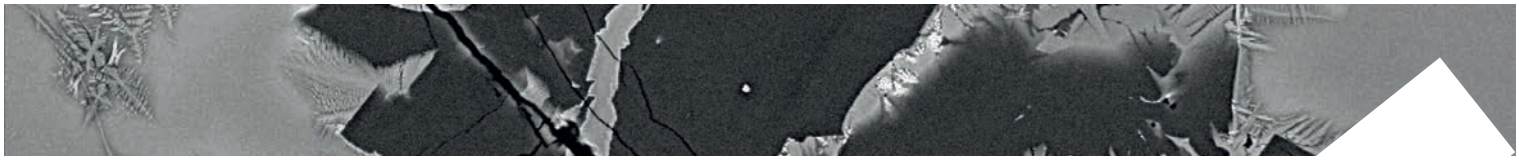

A Tale of Two Paroxysms: The 3 July and 28 August 2019 explosive eruptions at Stromboli Volcano

Andronico D., Del Bello E., D'Oriano C., Landi P., Pardini F., Scarlato P., de' Michieli Vitturi M., Taddeucci J., Cristaldi A., Ciancitto F., Pennacchia F., Ricci T., Valentini F.

In 2019, Stromboli volcano experienced one of the most violent eruptive crises in the last hundred years. Two paroxysmal explosions interrupted the 'normal' mild explosive activity during the tourist season, causing shock-waves, ballistic and tephra fallout, pyroclastic density currents, wildfires and small tsunami-waves. Heralded by three weeks of intensified ordinary activity and 45 minutes of lava outpouring, on 3 July a first paroxysm ejected ~10^7 kg of bombs and ash up to 6 km high, damaging the monitoring network and falling on the SW inhabited sector of the island. Intensified activity continued until the second, 28 August paroxysm, which dispersed tephra mainly towards NE. Our critical analysis of the recent data on paroxysms point to an urgent review of the volcanic hazard assessment at Stromboli. It is known that Stromboli's normal eruptive pattern is episodically perturbed by paroxysmal eruptions whose frequency and magnitude vary widely. It is however still unclear whether these events happen without prior notice or if they are preceded by reliable precursors in the normal activity. Although all the paroxysms are preceded by periods of anomalous changes in the shallow volcanic activity, an unambiguous eruptive pattern heralding a paroxysmal explosion cannot be recognized. However, a re-analysis of geochemical and geophysical parameters from the monitoring network detected some medium term (weeks) variation pointing to a destabilization of the deep magmatic system preceding violent explosions. Therefore, the ability to correctly recognize precursors heralding changes in the magma system in the medium term is crucial for estimating the potential occurrence of such events. We think that such changes could be efficiently detected in the magma system by running, on a daily basis, petrological and textural monitoring of eruptive products of the normal explosive activity, as well as high-frequency, systematic monitoring of a larger number of eruptions parameters (explosion type, elevation, duration, ejection velocity, frequency and number of active vents).

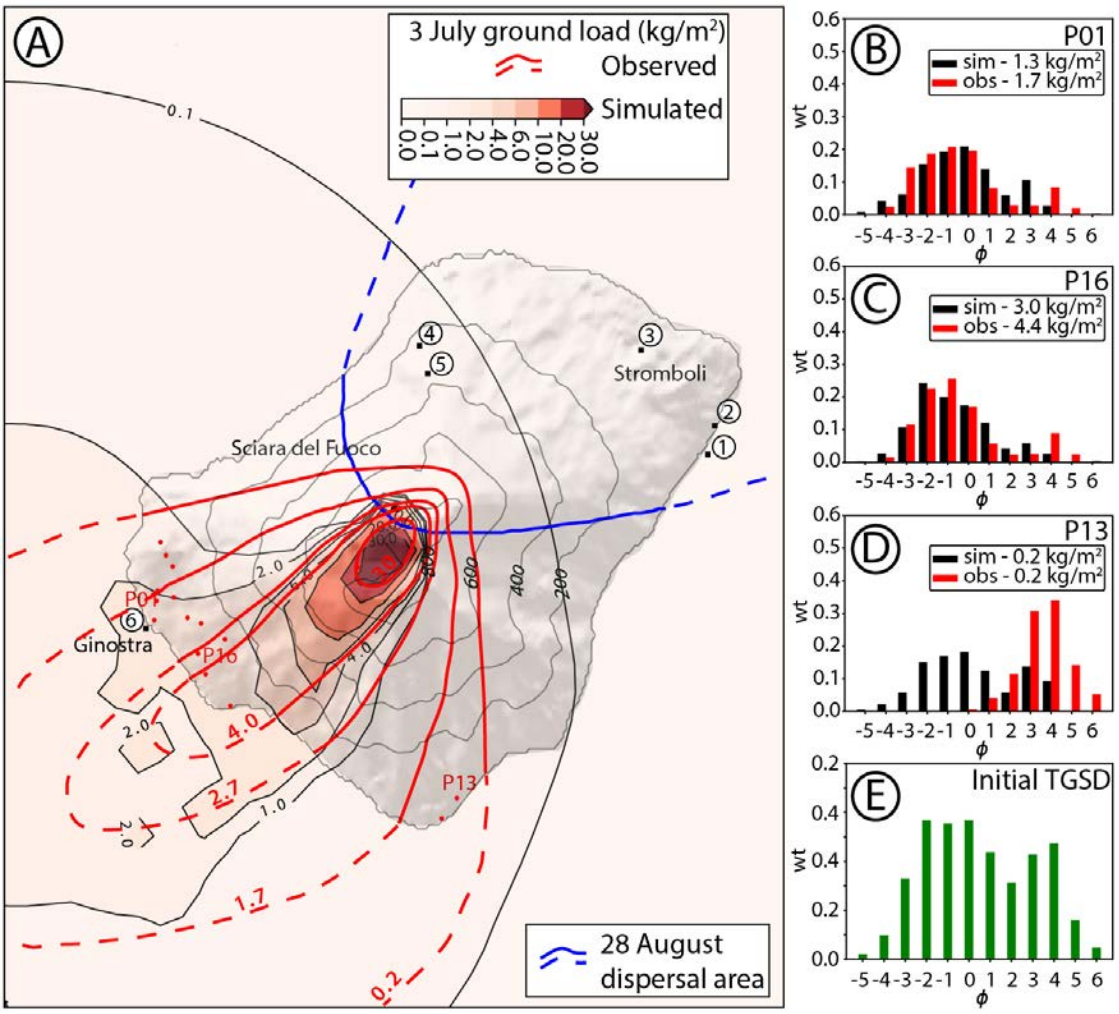

Fig. 11 Observed and simulated dispersal of tephra. (A) Sample locations of 3 July erupted deposits (red points) used for the estimate of observed isomass lines (red) and deposit ground load simulated by PLUME-MoM-TSM/HYSPLIT initialized with the eruptive source parameters inferred by the inversion procedure (pink-shaded areas). The deposit is simulated at 18:00 UTC (more than three hours after the explosion) and reveals a maximum ground load of about 30 kg/m^2. The circled numbers indicate 6 high-risk sites considered in the discussion. The inferred dispersal area for 28 August deposits is also shown (blue line). (B-E) Simulated (sim) and observed (obs) grain-size distributions at three sampling points (P01, P13 and P16, location shown in map), and Initial Total Grain-Size Distribution (TGSD) at the volcanic vent resulting from the inversion.

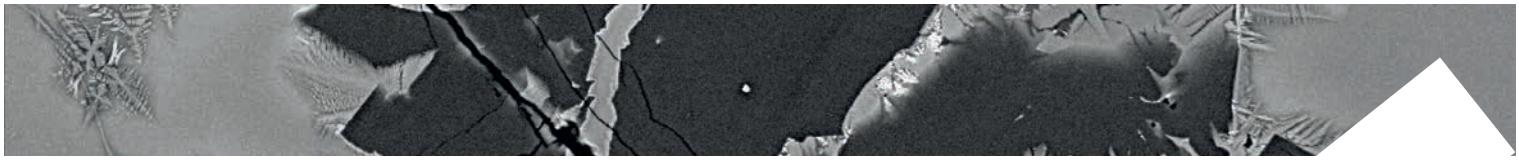

UAV surveys illuminate the morpho-structural and volume changes from the 2019 paroxysmal eruptions of Stromboli volcano (Italy)

De Beni E., Andronico D., Cantarero M., Civico R., Del Bello E., Di Traglia F., Eggersglüß M., Hansteen T., Hoernle K., Johnson J., Kwasnitschka T., Pizzimenti L., Ricci T., Scarlato P., Strehlow K., Taddeucci J.

Stromboli Volcano was very active in the summer of 2019: Two paroxysms dramatically changed the summit craters of the volcano on July 3 and August 28. The first intense paroxysmal eruptive sequence involved both the North and the Central-South (C-S) crater areas and has generated an eruptive plume rising 4 km above the summit (924 m a.s.l.) while the incandescent material set fire to vegetation on the flanks of the volcano. Volcanic products from the laterally directed explosions and from the collapse of the external crater terrace generated two pyroclastic flows that travelled down the Sciara del Fuoco (SdF) and for several hundred of meters out to sea. Between July 3 and August 28, the activity was characterised by lava flows in the Southern sector of the SdF and by very intense Strombolian activity at a set of small scoria cones that grew around the vents, particularly in the N crater area. The second paroxysmal eruption occurred on August 28 again involving the two crater areas and producing an eruptive column that rose 4 km above the summit. Material from the eruption and from the collapse of the rim of the C-S area contributed to the generation of a pyroclastic flow that travelled down the SdF and out to sea. Important morphological variations to the crater terrace were evident after the two paroxysms.We used UAVs to monitor morpho-structural changes of the Stromboli volcano following the paroxysmal eruptions; in particular, five high-resolution UAV survey campaigns have been performed since May 2019. The aerial images were acquired using two different UAVs, a DJI Mavic 2 Pro and a Wingcopter.

Using Structure-from-Motion (SfM) techniques we generated DEMs (Digital Elevation Model) and orthoimages with a resolution ranging between 0.2 and 0.5 m. An additional 1 m-resolution DEM was extracted from available tri-stereo Pleiades satellite imagery and chosen as a pre-paroxysm surface. Using the orthoimages it was possible to map the distribution of eruption products and determine the morpho-structural changes. Furthermore, the topographic approach (subtraction between two different surfaces DEMs) with a cut-and-fill procedure was chosen to calculate the volume gain (in the southern sector of the SdF) and loss (in the crater areas).

This work demonstrates the usefulness of the combined use of UAVs and SfM techniques

to map volcanic products, to highlight morphological changes and perform volume estimations. The data collected during these field efforts and the temporal comparisons of the DEMs represent a fundamental contribution to both volcanic hazard assessment and risk mitigation, and can be used to support civil protection operations.

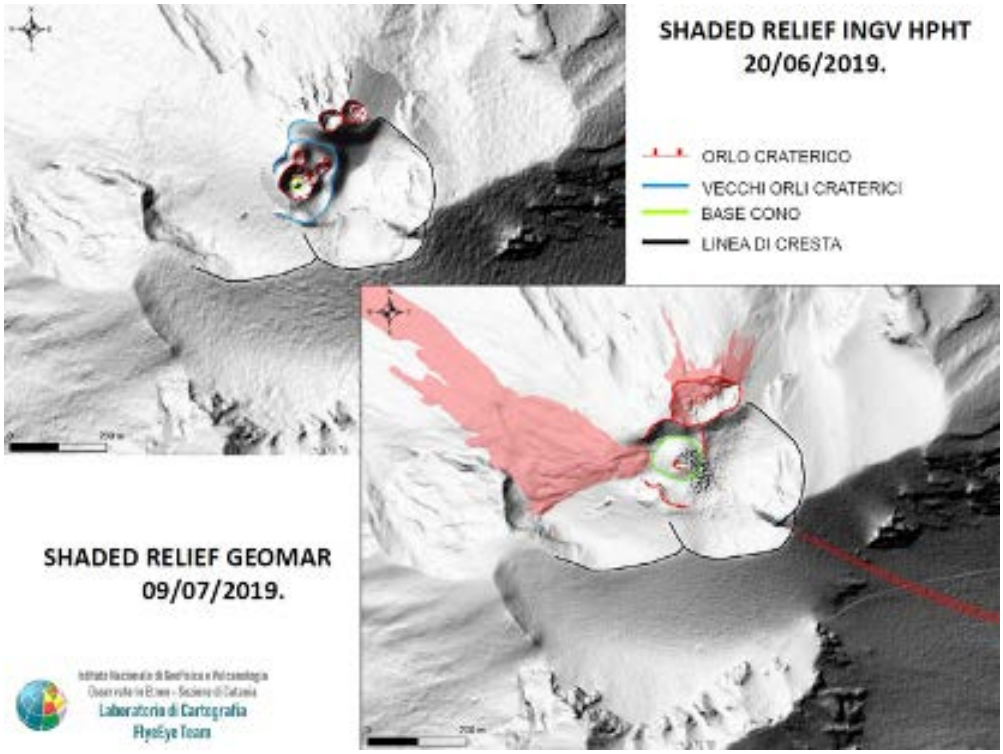

Fig. 11 Shaded relief maps showing changes of the pre- and post- July 3 paroxysmal eruption in the crater terrace of Stromboli.

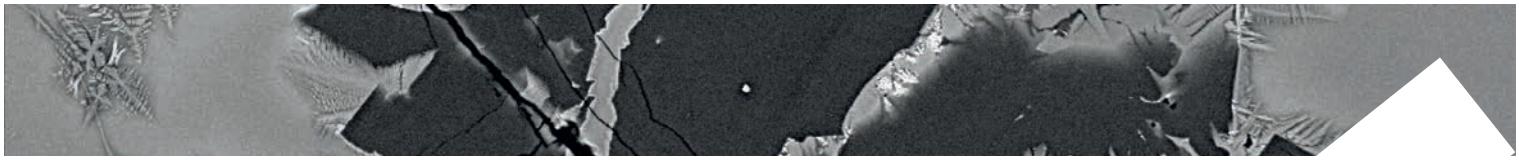

Observing volcanic activity and morphological changes associated with the 3 July and 28 August 2019 paroxysmal eruptions at Stromboli volcano (Italy) using UAVs

Ricci T., Andronico D., Civico R., Del Bello E., Di Traglia F., Johnson J.B., Pizzimenti L., Scarlato P., Taddeucci J.

Observing volcanic activity and resolving morphological changes on active volcanoes through time is key to understanding active volcanic processes. Unmanned Aerial Vehicles (UAVs) have recently become a powerful platform for aerial observation and data acquisition allowing close and detailed observation of the volcanic activity up to the eruptive vents. Moreover, they permit a rapidly-deployable, low-cost alternative to both classical manned aerial photogrammetry and airborne lidar. We, therefore, decided to use UAVs at Stromboli for a twofold objective: to monitor morphological changes of the volcanic edifice producing accurate, high-resolution digital elevation models (DEMs) and to observe the volcanic activity. Five high-resolution UAV surveys have been performed since May 2019. Using Structure-from-Motion (SfM) techniques we generated DEMs of the crater terrace area, lava flows and Sciara del Fuoco. The obtained DEMs have a resolution of 0.2-0.5 m. The comparison of the multi-temporal DEMs allowed for the evaluation of the height and volume variations due to the 3 July and 28 August paroxysms as well as for the months before and after these two events, for the morphological variations occurred in the crater terrace and for the evolution of the lava flow field. Since the 3 July paroxysm, UAVs revealed to be fundamental for the observation of the volcanic activity reducing the exposure of operators to volcanic hazards when the INGV video surveillance network (both thermal and visible) in the summit area of the volcano was destroyed. The combined use of UAVs and SfM techniques is crucial for improving our capabilities to collect frequent and low-cost measures on landscape changes associated with active volcanoes dynamics. The observation of volcanic activity and the data collection, as well as the temporal comparisons of the DEMs, represent a fundamental contribution to volcanic hazard assessment and can support civil protection operations and risk mitigation actions.

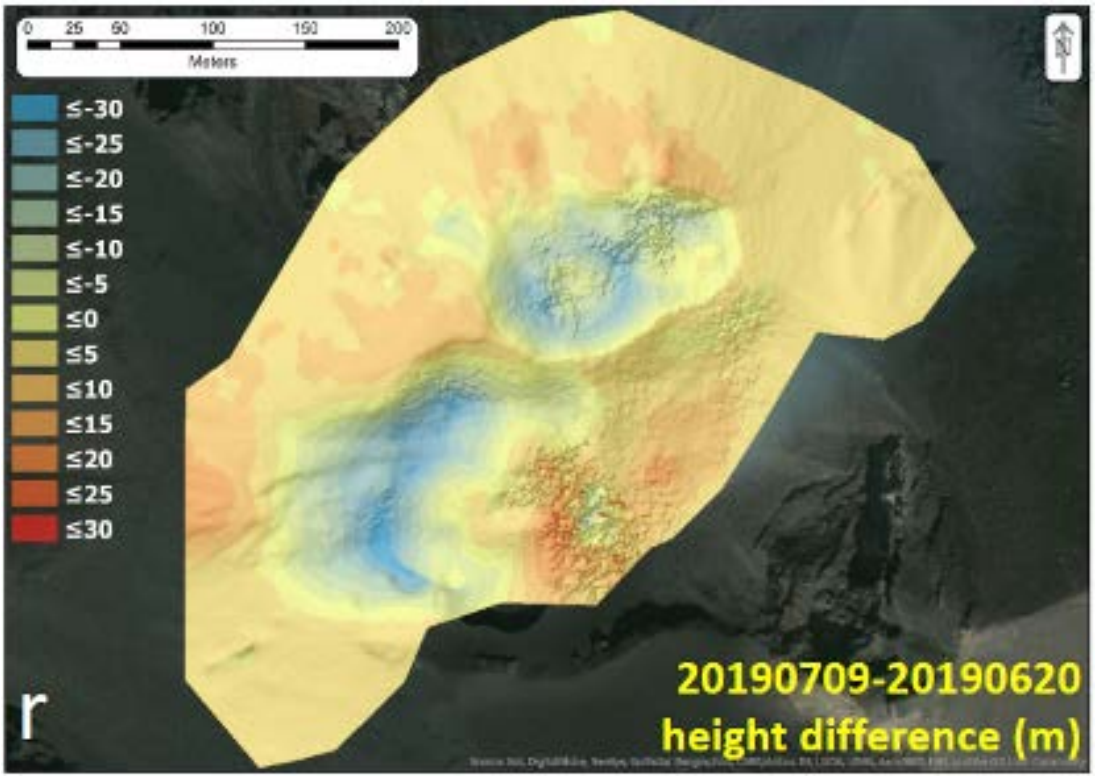

Fig. 1 | Elevation difference map highlighting changes at Stromboli crater terrace for the period 20 June - 9 July, 2019.

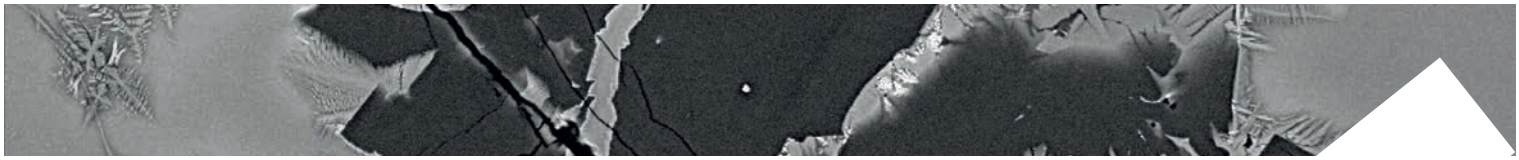

Significant changes in the magma dynamics of Stromboli steady-state volcano recorded by clinopyroxene crystals

Petrone C.M., Di Stefano F., Gertisser R., Mollo S., Tommasini S., Del Bello E., Andronico D., Scarlato P., Giacomoni P., Coltorti M.

Steady-state volcanic activity implies equilibrium between the rate of magma replenishment and eruption of compositionally homogeneous magmas, lasting for tens to thousands of years in an open conduit system. The Present-day activity of Stromboli volcano (Aeolian Islands, Southern Italy) has long been recognised as typical of a steady-state volcano, with a shallow magmatic reservoir (highly porphyritic or hp-magma) continuously refilled by more mafic magma (with low phenocryst content or lp-magma) at a constant rate and accompanied by mixing, crystallisation and eruption. The lp-magma is erupted only during more violent explosive events (paroxysms), which usually occur at intervals of a few years. However, the two most recent paroxysms occurred at very short timescales on 3 July and 28 August 2019 offering the unique opportunity of obtaining crucial information on the current magma dynamics of Stromboli. Albeit the plumbing system shows such uniformity, clinopyroxene phenocrysts exhibit marked chemical heterogeneities and complex textures caused by continuous lp-hp magma mixing as well as antecryst recycling from different mush portions. The compositional zoning in clinopyroxene provides essential information on pre-eruptive magma dynamics, indicating multi-stage crystallization across the lp-hp-reservoirs, where diopsidic compositions are markers of more primitive, high-T magmas injecting into shallow, low-T domains of the plumbing system. By comparing clinopyroxene texture, chemistry and residence times from the Present-day eruptions with the previous Post-Pizzo activity, we conclude that a distinct phase in the life of Stromboli volcano commenced after the violent 2003 paroxysm. Our observations suggest there are more efficient mechanisms of mush disruption and cannibalization, in which old diopsidic antecrysts are continuously remobilized and transported by the lp-magmas permeating the mush. The disappearance of diopsidic recharge bands within augitic overgrowths indicates that over time, magmatic injections feeding the persistent Present-day activity are more intensively mixed and homogenized prior to eruption (Figure 1).

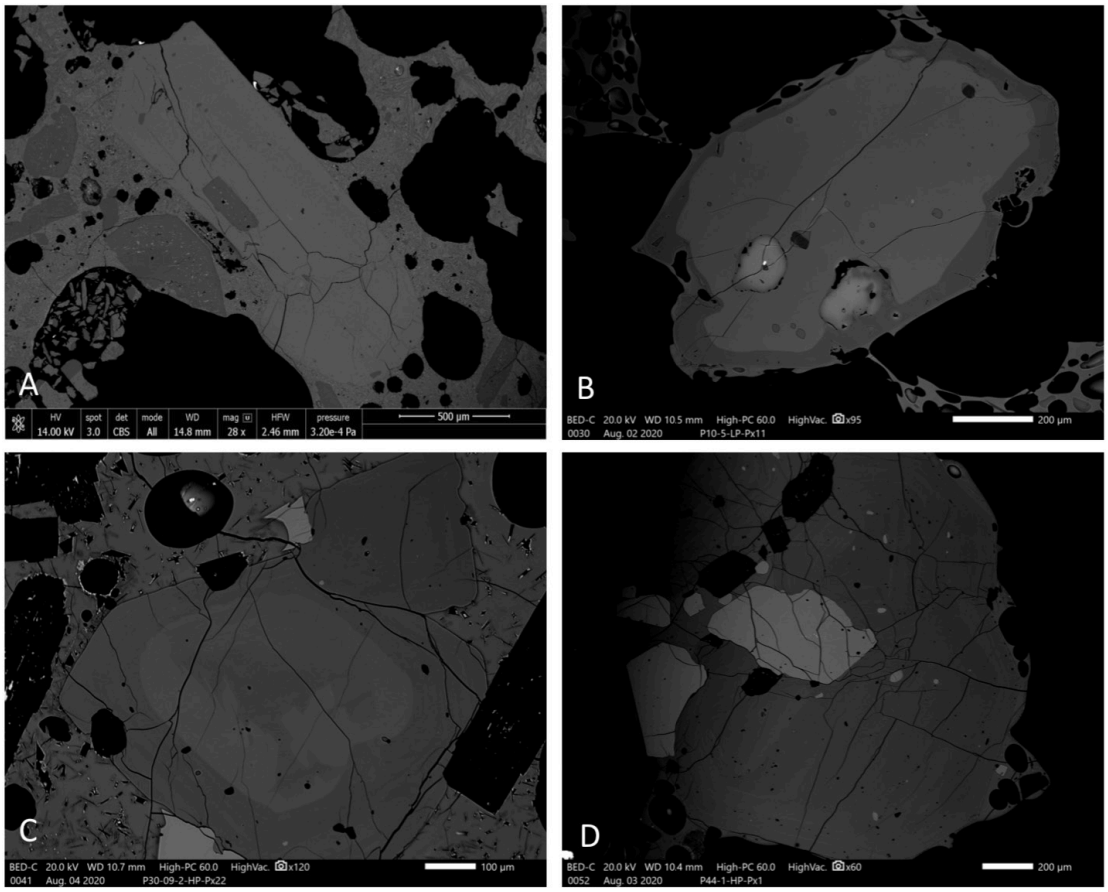

Fig. 1l Textural variability of Stromboli clinopyroxene in the volcanic products erupted during the summer 2019. A) homogeneous augitic crystal; B) augitic core with diopside rim; C) complex zoning in clinopyroxene with patchy core, augitic mantle and diopside rim; D) glomerocrysts of clinopyroxene and olivine.

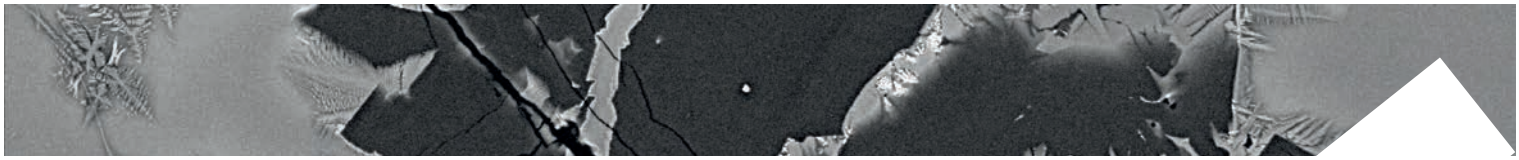

Atomic structure of a picritic melt as function of pressure and temperature

Stopponi V., Hrubiak R., Misiti V., Nazzari, M., Scarlato P., Stagno V.

The investigation of the atomic structure of silicate melts as a function of pressure (P) and temperature (T) broadens our knowledge of magma mobility at conditions of the Earth's upper mantle and how this changes during ascent to the surface. In this study, we determined the atomic structure of a synthetic picritic melt by in-situ multi-angle energy-dispersive X-ray diffraction (MA-EDXRD). The employed starting material is a synthetic glass (FS DRY) that was taken as analogue of natural picrite retrieved from olivine-hosted melt inclusions of Fall Stratified (FS) tephra deposit erupted by Mt. Etna, i.e. the known most primitive Etnean composition of mantle origin. FS DRY was prepared by melting a mixture of SiO_2, Fe_2O_3, Al_2O_3, MgO, $CaCO_3$, Na_2O and K_2O in a Pt crucible at 1,450°C. The quenched product was analyzed using the JEOL JXA-8200 Superprobe available at the HP-HT laboratory of the National Institute of Geophysics and Volcanology (INGV) in Rome, Italy. In-situ multi-angle X-ray diffraction measurements were performed in a pressure range of 2.4-6.7 GPa and temperature varying from 1,500-1,750 °C using the Paris-Edinburgh press installed at beamline 16 BM-B at the synchrotron radiation facility of Advanced Photon Source (Lemont, IL, USA). Our in-situ experiments allowed the determination of the structure factor S(q), indicative of the intermediate range order (IRO) of the melt structure in real space, i.e. silicate network compaction, and the local structure, i.e. interatomic distances, by Fourier Transformation of S(q) to obtain the radial distribution function G(r). Preliminary results are shown in Figure 1 along with data collected at ambient P/high T and ambient P/room T. The first sharp diffraction peak (FSDP) of S(q) shifts linearly from 1.97 $Å^{-1}$ to 2.25 $Å^{-1}$ as a function of increasing P (Figure 1a, c). This linear correlation reflects the decrease in IRO from 3.17 Å to 2.84 Å within the investigated pressure range. In addition, the second peak (SSDP) in the structure factor becomes more and more intense as P increases, implying a considerable diminution of the volume in the silicate network.The local structure was determined through G(r) (Figure 1b) in terms of interatomic distances between tetrahedrally coordinated cation (T= Si^{4+} and Al^{3+}) and oxygen (T-O), tetrahedron-tetrahedron (T-T) and T-O-T angle. Distances between tetrahedra vary between 3.21 and 3.15 Å up to 5 GPa, followed by a sudden shrinkage to 2.91 Å at pressures greater than 6 GPa. The pressure-dependent variation of interatomic distances implies a change of the T-O-T angle from 154° to ~118° (Figure 1d). The observed increase in T-O bond length upon compression is in contrast to that of mid-ocean ridge and alkali basalt.

The structure of picritic melt at HP-HT shows unique features among silicate melts and glasses investigated so far.

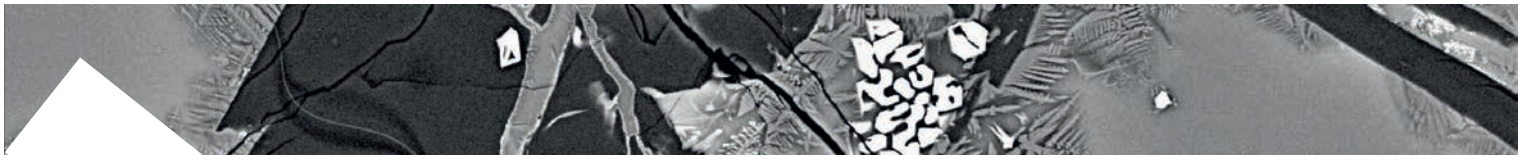

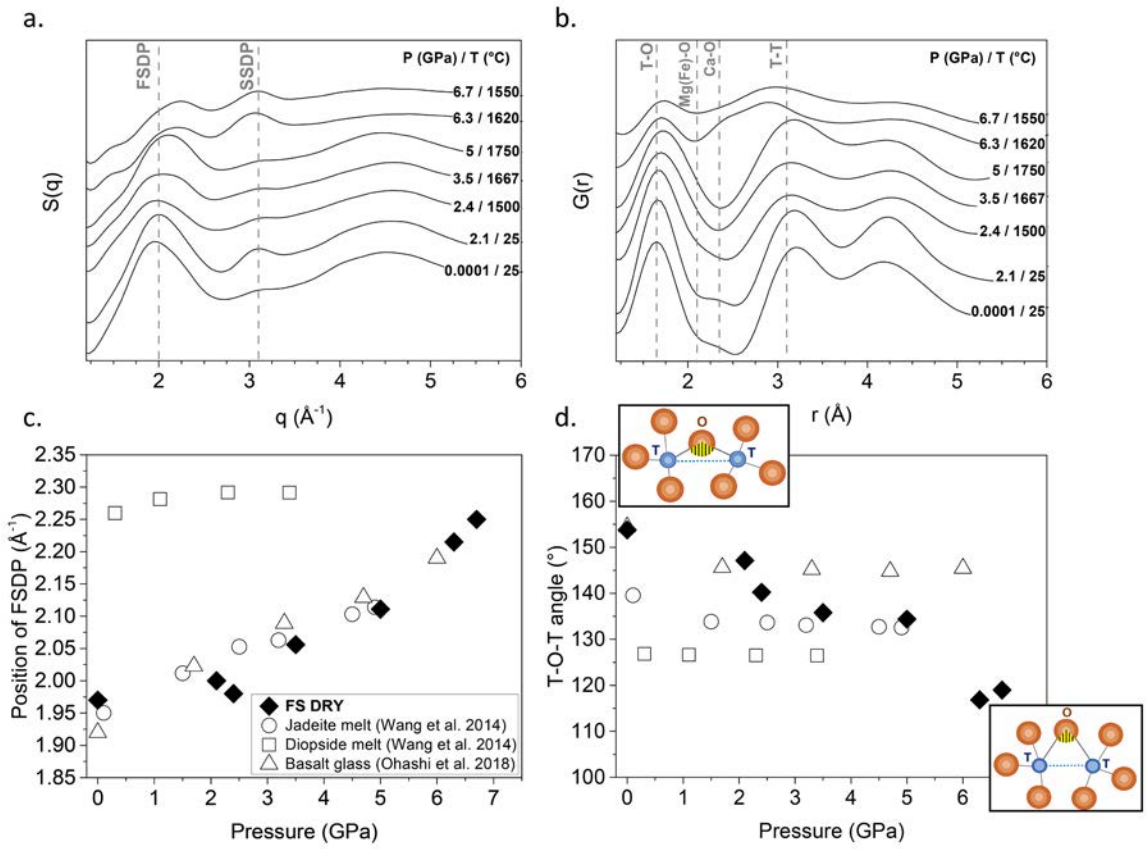

Fig. 1l The structure of FS picritic melt determined in-situ by EDXD measurements: structure factor S(q) (a), radial distribution function G(r) (b) and variation of FSDP positions (c) and TOT angle (d) as a function of pressure, with a schematic representation of TOT shown in the insets

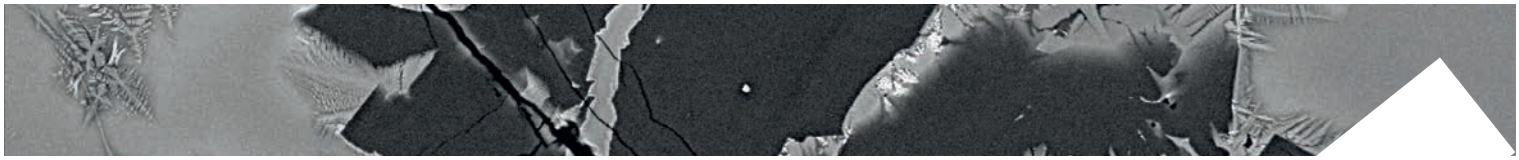

Constraining schorl stability field through the definition of its structural breakdown temperature at 3.5 GPa

Celata B., Andreozzi G.B., Ballirano P., Bosi F., Capizzi L., Scarlato P., Stagno V.

Tourmalines, boron-rich cyclosilicates (borosilicates), are fascinating and colourful accessory minerals occurring in a variety of geological environments, from diagenetic stages to granulite facies grade. Tourmaline gained more and more interest along the years surely because of its remarkable power to carry a lot of information about its genetic conditions but its relevance stands owing to its role of boron and water carrier from the crust deep down the mantle through subduction zones. When breakdown conditions are reached, the crystal structure collapses and boron and water are released with boron being strongly partitioned in the aqueous phase, affecting, therefore, the rheology of the surrounding host rock and the composition of metasomatic fluids.

To date, the conditions and mechanism controlling the breakdown of tourmaline are unclear with respect to structural variations and resulting phase equilibria with emphasis for the deprotonation process, i.e. whether "water" is fully released way before the structural collapse or throughout the whole breakdown process.

An Fe-rich tourmaline (schorl) hosted in a leucogranite from the Seagull batholith (Yukon Territory, Canada), chemically characterized by Andreozzi et al. (2020), was used as starting material.

Eight experimental runs were performed at a pressure of 3.5 GPa and temperatures ranging from 500 °C up to 950 °C to fix the schorl breakdown conditions. The crystal fragments were grounded and blended with buffer compounds, then placed in cell assemblies made of MgO doped with 5 wt.% of Cr_2O_3 with 18-mm octahedra edge length (OEL) in combination with tungsten carbide second stage anvils (F-grade) of 11-mm truncation edge length (TEL). Such assemblies were used to perform *HP-T* experiments with the 840-ton Walker-type multi anvil press available at National Institute of Geophysics and Volcanology (INGV) in Rome (Italy). Rhenium and graphite capsules with a diameter of 2 mm, filled by starting material, were used. The experiments were finally quenched by shutting down the electrical power. The experimental products were recovered and analyzed through a multi-analytical approach: SEM imaging, EMP point analysis and XRPD. At 750 °C and 3.5 GPa several garnet crystals were clearly visible from SEM images (Figure 1 a and b) together with the appearance of topaz, even if garnet was already detected at 700 °C by EMPA. Such a mineral assemblage is consistent with the first breakdown products of the schorl, so the breakdown conditions can be fixed at 3.5 GPa and at about 700 °C. The first appearance of glass is recorded at 800 °C by EMP analysis which show a hydrous melt portion (about 32 wt.% of water and likely boron). The lacking of

intergranular boundaries among tourmaline crystals was though detected by textural analysis on SEM images already at 750 °C. All the aforementioned phases were also identified through XRPD, exception made for the glass portion which diffraction effect is likely to be mixed up with the broad diffraction peak of the capillary.

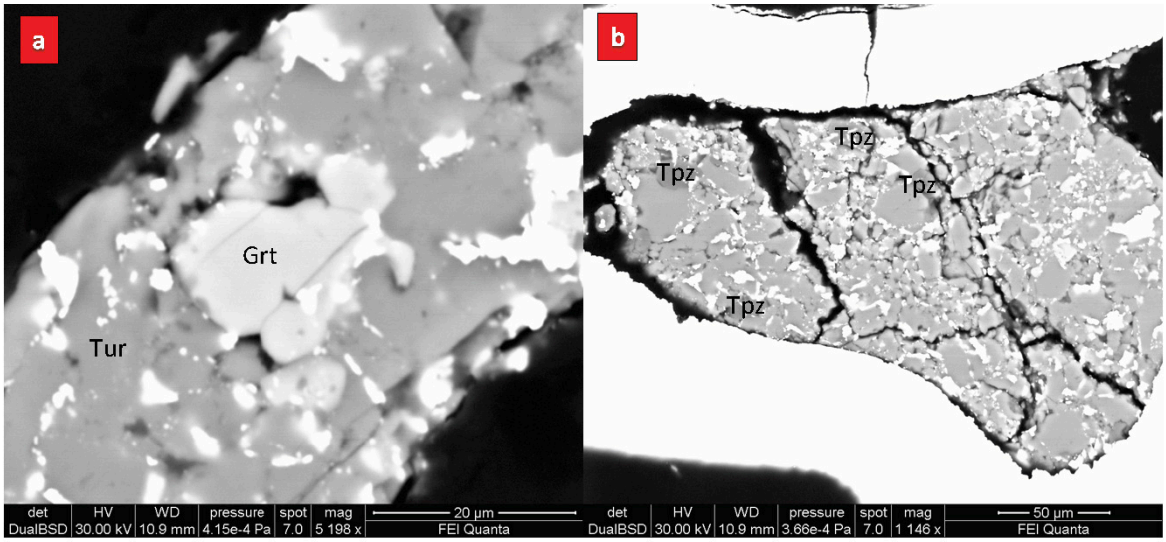

Fig. 1l a) A large single crystal of garnet (Grt) surrounded by tourmaline (Tur) from the 750 °C run. The brightest portions are the disseminated Re and ReO_2 buffer material. Intergranular boundaries are noticeably lacking.
b) Distribution of some small topaz crystals in a portion of the sample from the 750 °C run.

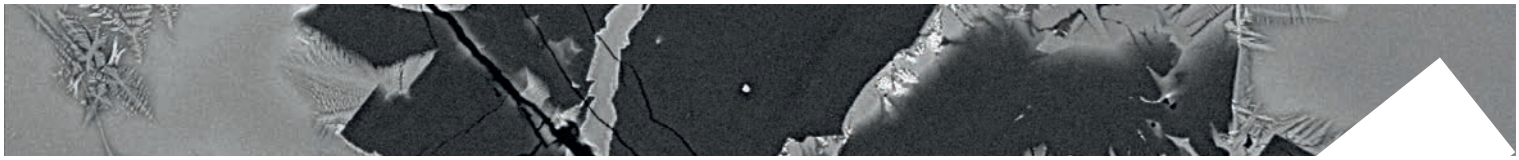

The Stromboli activity in the summer 2019: field-data and magma textures as a key to better understand the open-conduit basaltic volcanism

De Astis G., Giordano G., Piochi M.

During summer 2019, Stromboli volcano experienced a prolonged and very sustained ordinary activity, a major explosion (June 25) and two vulcanian eruptions generated by a basaltic magma (July 3 and August 28 "paroxysms"), which was constantly very high in the shallow system (i.e. 25-35 VLP/h daily events until early September). Afterwards, the mild ordinary Strombolian-type explosive activity was restored in about two months. Volcanological parameters as plume height (≈8.4 km) and MER ($1.1*10^6$ kg/sec) indicate the July 3 eruption as the highest in energy since 1930. Volcanic phenomena for both vulcanian events include: formation of PDCs; tephra fallout on Stromboli villages; severe changes in the crater's morphology due to both flaring and rims increase for tephra accumulation.

Shoshonitic to high-K basaltic as bulk-rock compositions, the collected juvenile fragments are frequently represented by LP-pumice/HP-scoria intimately-mingled fragments, assuming a large variety of shapes. This mingling can be seen from large (field) to very small (SEM) scale and probably is a process that is most evident for the 28 August products. Here we remember that: i) LP products consist of golden-brown and highly vesiculated pumices, crystal-poor (percentage is variable according to the amount of embedded xenocrysts); ii) HP products are dense, grey to dark black scoriae, crystal-rich (45-55% vol.), representative of a largely degassed magma. The glass compositions achieved for our samples from both events have SiO_2 contents varying between 47-56 wt.% ca., whereas a typical geochemical parameter used to discriminate LP and HP magmas display a variation from 0.36 to 0.65, with LP typically between 0.5 and 0.6. (Figure 1).However, the Figure makes evident that more than one sample displays almost the whole spectrum of glass compositions, regardless if it is HP or LP. Crystals with zoning and disequilibrium features are quite common. These data suggest that a larger volume of HP viscous magma in the volcano upper portion formed a transient plug and prevented the normal melt/gas transfer dynamics from deeper reservoir(s), triggering a deep interaction between different rheologies. In addition, different behaviours of and texturally different juvenile products from SW and NE craters highlight the substantial role played by the shallow conduit geometries.

Compared to paroxysms occurred in 2003 and 2007, the 2019 ones mark a sharp difference in terms of eruptive pattern since they are not linked to the effusive emptying of the HP magma stored at shallow levels, allowing the decompression and fast rise of the deeper sited LP magma, as trigger mechanism.

The transition from ordinary to blast-like

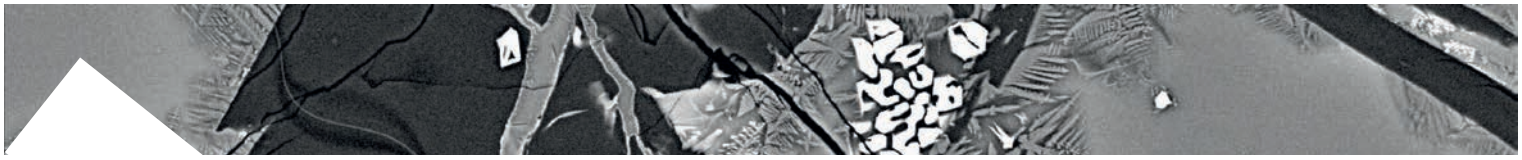

phenomenology depicts a different scenario that is probably associated with the quick arrival of LP magma at shallow levels, its interaction with the ponding/loading HP magma batch and the genesis of a violent explosive mechanism whose reasons are not clear, yet. Remarkably, the 2019 activity reveals that short lava effusion, major explosions and stronger vulcanian eruptions are able to occur with little or no warning along the ordinary spectrum of strombolian activity.

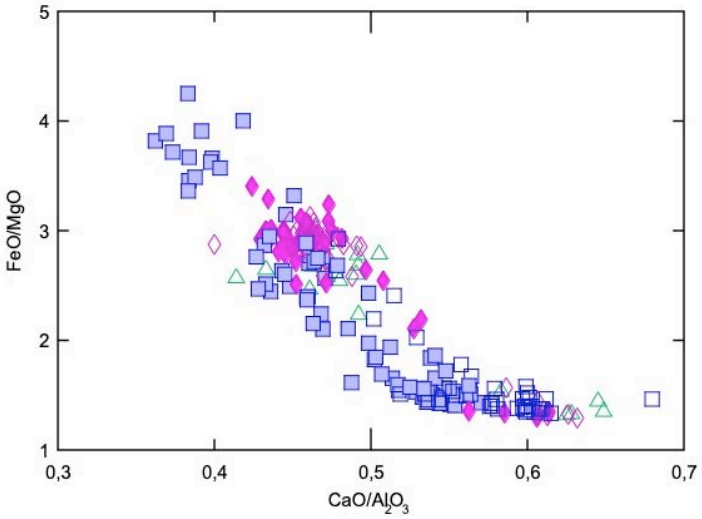

Fig. 11 CaO/Al_2O_3 vs. FeO/MgO diagram for 2019 HP and LP products (spatters, bombs, lapilli) collected during: June 25/26t major explosion, July 3 and August 28 "paroxysms". Symbols: Open triangles= Major Explosion sample; Open Diamonds= LP products from July 3; Full diamonds= HP products from July 3; Open Squares= LP products from August 28 (including the half "aphyric" portion analyzed in a HP sample); Full Squares= HP products from August 28.

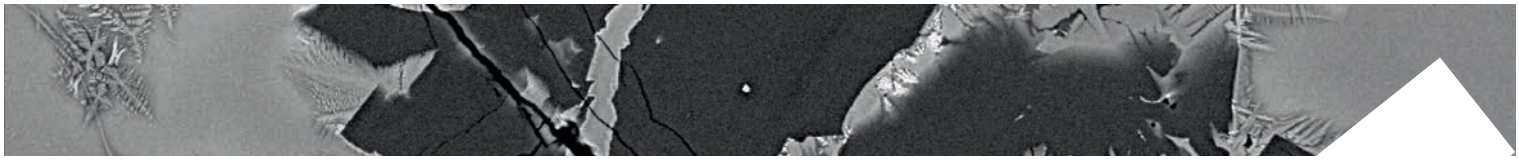

Kinetic partitioning of major-minor cations between olivine and Hawaiian tholeiitic basalt under variable undercooling and cooling rate conditions

Lang S., Mollo S., France L., Misiti V.,Nazzari M.

In order to elucidate the kinetic partitioning of cations between olivine and Hawaiian tholeiitic basalt, we performed undercooling (-ΔT) and cooling (CR) experiments at atmospheric pressure and QFM-2 buffer. Starting from the superliquidus temperature of 1,250 °C, the charges were cooled at the rates of 4 (CR4), 20 (CR20), and 60 (CR60) °C/h to the final target temperatures of 1,175 °C (-ΔT = 35 °C; -ΔT35) and 1,125 °C (-ΔT = 85 °C; -ΔT85). Results show that polyhedral olivine morphologies are obtained at -ΔT35, whereas strong disequilibrium skeletal and/or dendritic textures form at -ΔT85. The amount of forsterite in olivine decreases from to 85% to 78% with increasing both -ΔT and CR. A diffusive boundary layer also develops in the melt next to the olivine surface and its composition becomes progressively enriched in Ca, owing to its incompatible behavior with the lattice site. Residual melts are progressively depleted in silica and alkali from CR4 to CR60, but silica-rich melts are observed with increasing -ΔT. In terms of Fe-Mg exchange, olivines obtained at -ΔT35 are always in equilibrium with the diffusive boundary layer, comprising both the interface melt next to the olivine surface and the far-field melt where all chemical gradients cease. At -ΔT85, however, the Fe-Mg exchange indicates two distinct equilibration stages between olivine core and far-field melt, and between olivine rim and interface melt. Partition coefficients (K) of Mg, Fe, Mn, Ca, Cr, and Ni calculated at the olivine-melt interface preferentially change as a function of -ΔT rather than CR. From -ΔT35 to -ΔT85, K_{Mg}, K_{Fe}, K_{Mn}, and K_{Cr} remarkably increase, whereas the opposite applies to K_{Ni} and K_{Ca}. Through the application of equilibrium partitioning models, we found that Mg, Fe, Mn, and Ca are incorporated into the olivine lattice site at near-equilibrium proportions. This generally good agreement with modeling data demonstrates that diffusive mass transport of cations in our experiments occurred under the conditions of local equilibrium at the olivine surface. In contrast, marked deviations from the expected equilibrium are found for K_{Cr} and K_{Ni} in response to the major influence of crystal field stabilization energy on cation incorporation.

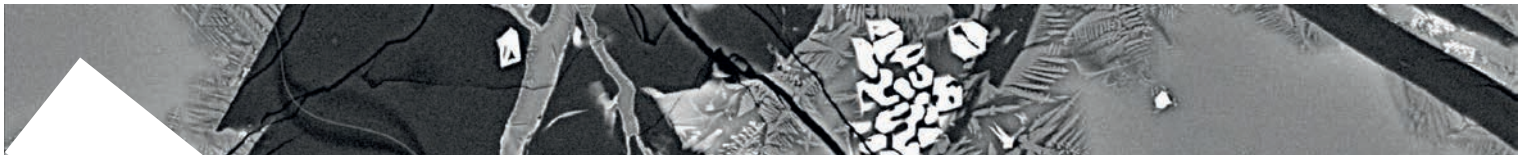

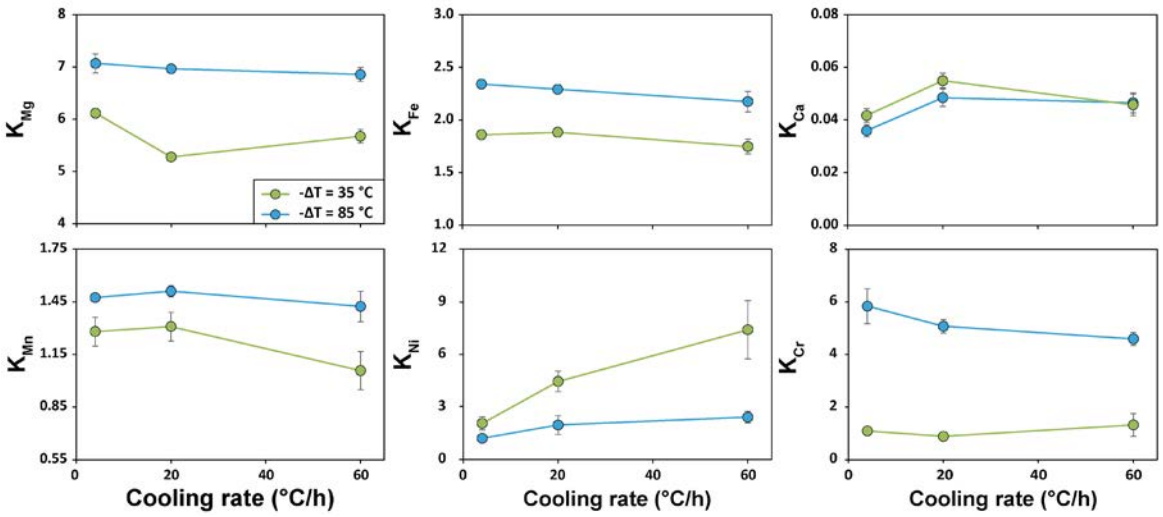

Fig. 11 Olivine-melt partition coefficients of major and minor elements versus cooling rate (4, 20, and 60 °C/h). Data are plotted for both undercooling conditions of 35 and 85 °C

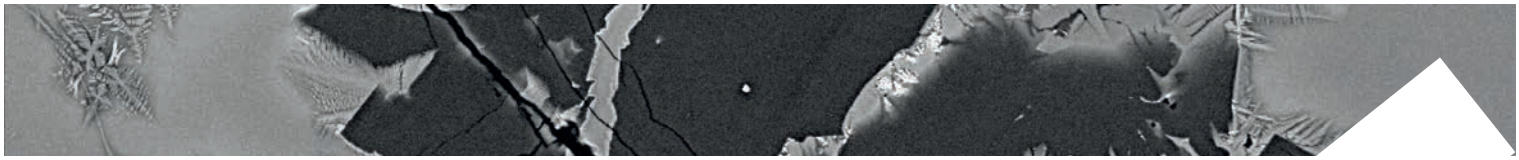

8.2 ROCK PHYSICS and EARTHQUAKES

Mirror-like slip surfaces in extensional faults cutting Bituminous dolostones (Fornaca Valley, Central Apennines, Abruzzo)

Bersan E., Fondriest M., Spagnuolo E., Nazzari M., Di Toro G.

Earthquakes and aseismic creep are due to slip along faults. The same fault can record short lasting slip events at slip rates of 1 m/s due to seismic slip, episodic to continuous creep events at slip rates < 0.1 µm/s and fault sealing during the interseismic phase. Given the broad range of loading conditions, a number of mechanical and chemical processes operate in fault zones such as fracturing, wear, frictional melting, fluid-rock interaction, crystal plastic deformation, dissolution and precipitation, etc. As a consequence, the resulting fault zone rock can be used to determine the processes operating during the seismic cycle. In particular, many faults in carbonate rocks are characterized by naturally polished and reflective surfaces ("mirror-like fault surfaces"). Recent experiments found that mirror-like slip surfaces can form during rapid fault sliding but also at sub-seismic slip rates; thus, they are not necessarily diagnostic of seismic slip. As a consequence, the origin of natural mirror-like surfaces in carbonate rocks is debated in the literature. This is not just an academic debate, as understanding the origin and age of mirror-like fault surfaces is relevant also for seismic hazard studies.
To contribute to the debate, we focused on recently found mirror-like fault surfaces hosted in bituminous dolostones of the Italian Central Apennines where ultra-polished slipping surfaces are characterized by the presence of smeared bitumen. We performed detailed structural geology surveys of the fault zone, optical and scanning electron microscope investigations of the wall rocks, fault slipping zones and "mirror-like" fault surfaces.
The field area in the Italian Central Apennines are one of the most seismically active areas in the Mediterranean (e.g. L'Aquila Mw 6.1, 2009; Avezzano Mw 7.0, 1915). Most of this continuous seismicity is produced by earthquake ruptures propagating along normal faults hosted in carbonate rocks (dolostones and limestones). However, several faults in Central Apennines may accommodate deformation also by aseismic creep. Here we investigated extensional faults cutting through the Upper Triassic Bituminous dolostones Fm. cropping out in the Fornaca Valley in the Gran Sasso Range (Central Apennines). The extensional faults are located in the footwall of the younger-on-older Mt. Camicia Thrust. I discuss the structural evidences associated to the Late Miocene-Early Pleistocene compressional phase related to the activity of the Mt. Camicia Thrust and to the following Middle Pleistocene to Quaternary extensional phase that partly reactivated the thrust and resulted also in the formation

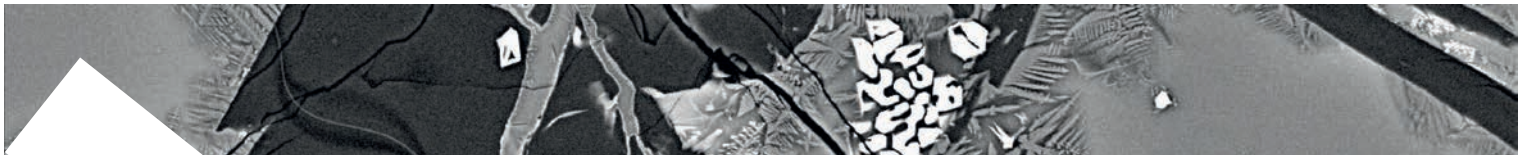

(and reactivation) of a complex network of minor faults. The normal faults have slipping zones recording multiple slip events and are bounded by mirror-like often bitumen-rich ultrapolished slip surfaces. Microstructural evidences support the hypothesis that these faults recorded both seismic slip (ultracataclasites with fragments of bitumen-rich slipping zones) aided by the ingression of carbonate-rich fluids (ultracataclasites are cemented by a calcite-rich vein-precipitated matrix) and aseismic creep (cataclastic flow in dolostones aided by pressure-solution and viscous shear of the bitumen-rich layers).

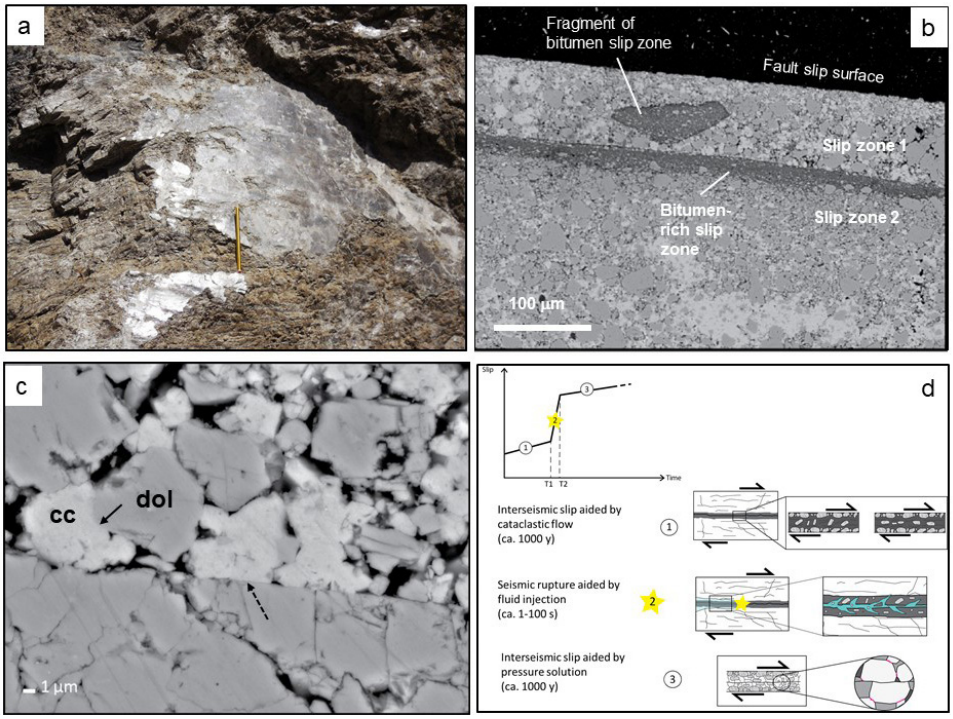

Fig. 11 Mirror-like fault slip surface cutting the Upper Triassic Bituminous dolostones Fm. cropping out in the Fornaca Valley in the Gran Sasso Range (Central Apennines). (a) Field exposure of mirror-like slip surface (pencil for scale). (b) Mirror-like fault slip surface with two slip zones beneath (slip zones 1 & 2). The upper slip zone 1 includes fragments of the underlying bitumen-rich slip zone immersed in ultracataclasite made of dolomite clasts cemented by calcite. The presence of the latter is indicative of the percolation of carbonate-rich fluids. The lower slip zone 2 is made of an ultracataclasite similar to the one of the slip zone 1. The contact with the slip 1 is marked by a quite continuous layer of a smeared bitumen-rich matrix. (c) Detail of the contact between slip zones. The calcite grains (probably precipitated by carbonate-rich fluids) are indented by the dolomite grains (black arrow). The calcite grains have flat contacts with the lower dolomite-built polished slip surface, indicative of the activation of diffusive mass transfer processes (pressure solution, dashed black arrow). (d) The microstructures described in (b) and (c) can be interpreted as the result of different stages of the seismic cycle. (b & c: Field Emission Scanning Electron Microscope Back Scatter Electrons Images, INGV-Rome HP-HT labs).

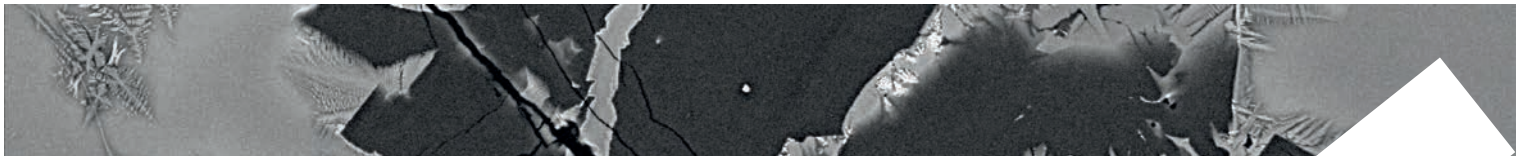

On the stability of sliding: hydromechanical responses of basalt rock-on-rock contacts to fluid pressure stimulation

Giacomel P., Spagnuolo E., Aretusini S., Di Toro G., Collettini C.

Diffusion of fluid pressure into pre-existing faults is one of the principal mechanisms for human-induced seismicity. This mechanism reduces the effective normal stress that clamps the fault in place promoting fault motion, yet it remains unclear the mode of fault slip upon reactivation and the conditions leading to dynamic frictional instabilities. Here we present laboratory tests on simulated basalt faults to investigate how the hydromechanical coupling affects the fault slip behavior and the dynamic weakening upon fluid pressure stimulations. We performed two types of experiments using the rotary-shear apparatus SHIVA on initially-bare, basalt surfaces: (1) Constant displacement rate experiments at 10 µm/s to characterize the failure envelope of basalts bare rock surfaces; (2) Unconventional creep experiments at constant shear stress on nearly critically stressed faults subjected to fluid pressurization, consisting in stepwise increases of 0.2 MPa/300 s (Figure 1a). Creep experiments were run after a pre-shear stage of 4 mm and 50 mm of slip to test the effect of cumulated displacement on the hydromechanical properties and hence on fault frictional stability. To this end, the simulated faults were categorized according to their initial transmissivity and to net displacements before and after the tests. With the experimental simulation, we document that sheared basalts are frictionally strong, with the static friction coefficient within the range of Byerlee's rule for friction, i.e., $\mu \sim 0.66$. Before the onset of seismic slip, we recorded repeated slip pulses accompanied by shear compaction, and followed by fault deceleration and arrest. In the fault pre-sheared for 4 mm, the first slip episodes were characterized by slip rates of ~ 20 mm/s, whereas in the one pre-sheared for 50 mm, slip rates were one order of magnitude faster. Shear-enhanced compaction hindered the flow-through faults, facilitating the transition from drained to locally undrained hydrologic conditions, as testified by the development of fluid overpressure transients larger than the imposed fluid pressures (Figure 1b,c). Fluid overpressure transients exacerbated the mechanical fault weakening effect induced by fluid pressure stimulations, becoming more pronounced the lower the hydraulic transmissivity of the faults. Overall, our results show that compaction-induced weakening driven by fluid pressurization can overcome the rate-strengthening behavior of bare rock surfaces on basalts, promoting seismic slip (MI in Figure 1c). Such feature would produce strong implications for the assessment and mitigation of seismic risk in geo-energy projects associated with in-situ wastewater injection into underground basaltic occurrences. To this purpose, further experimental investigation is strongly needed to support the present hypothesis.

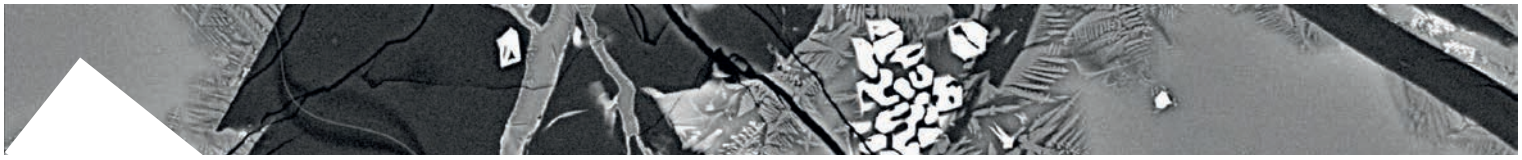

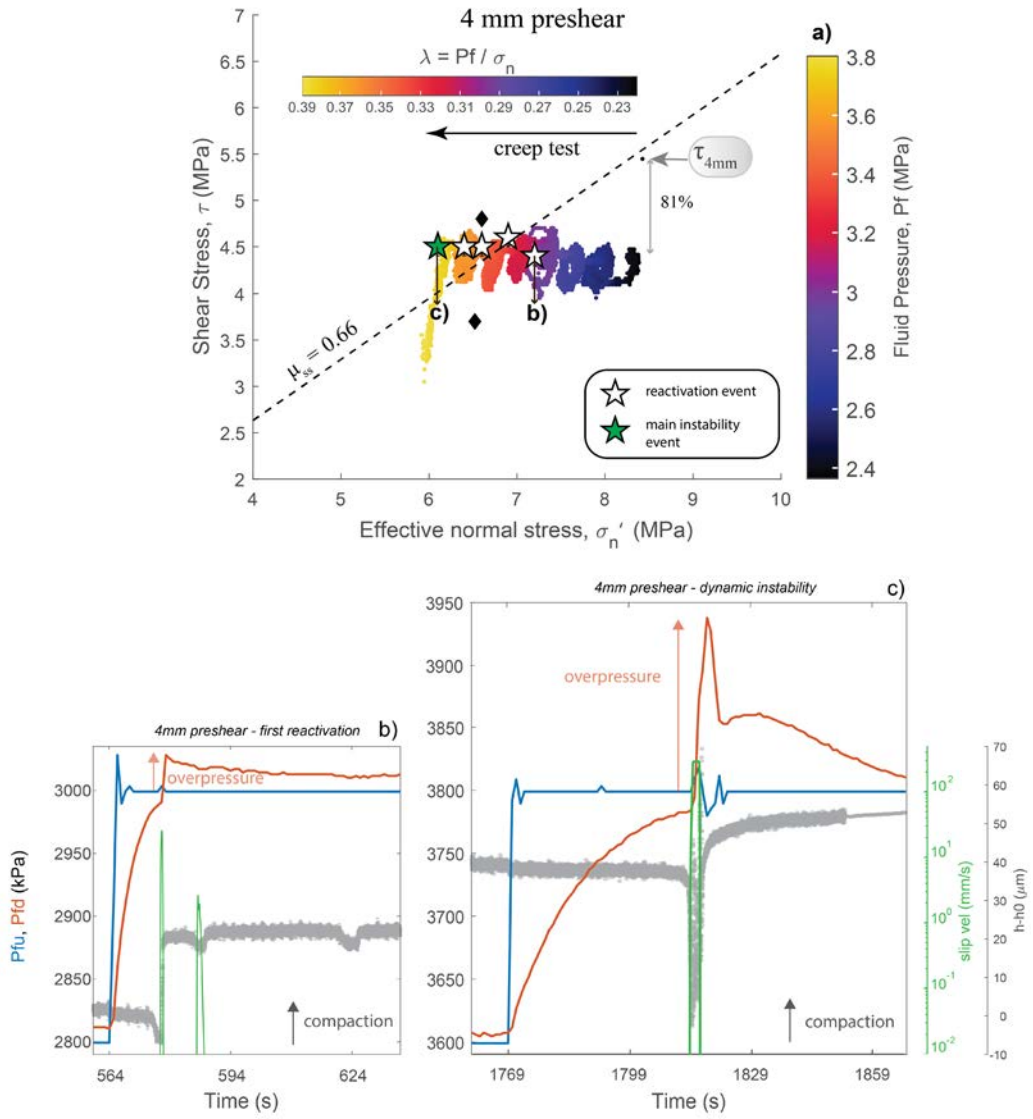

Fig. 11 **(a)** Stress path of a creep test at constant shear stress carried out on initially-bare, basalt surfaces pre-sheared for 4 mm and the coupled hydromechanical response associated with **(b)** the first slip event and **(c)** the seismic slip event (MI) during fluid pressurization. The blue line represents the imposed upstream pressure step (Pfu); in orange we show the downstream fluid pressure (Pfd) that tends to equilibrate with the upstream pressure with time. h-h0 indicates the fault axial displacement with respect to the reference value h0, i.e., the axial displacement at the onset of the fluid pressure steps: h-h0 > 0 means compaction, whereas h-h0 <0 implies fault dilation. Note the large fluid overpressure transient associated with the seismic slip event (MI). The development of large fluid overpressure transients testifies a remarkable reduction in hydraulic transmissivity accompanying shear-enhanced compaction throughout the test, promoting fault weakening.

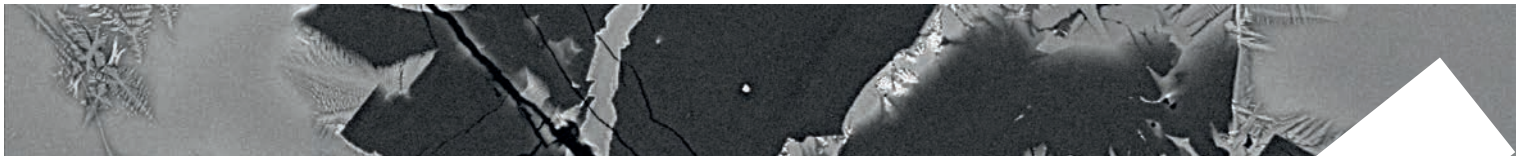

The role of tectonic lithological contacts in controlling fault weakening at seismogenetic PT

Aretusini S., Tesei T., Mittempergher S., Remitti F., De Paola N.

Tectonic lithological contacts occur when faulting or folding activity juxtaposes two lithologies with different viscoelastic and hydraulic properties. It was shown that these lithological contacts provide heterogeneity at the mesoscale, giving rise to anisotropy in the rock body. This anisotropy can be exploited from a variety of natural processes, from fluid flow to strain localization and rupture propagation parallel to the interface.
We performed a series of experiments in a triaxial apparatus hosted at the University of Durham in direct shear configuration. The samples were natural claystones collected in the Argille Varicolori formation (Northern Appennines), representative of an exhumed shallow accretionary prism. We sampled near the tectonic contact from two claystones (red and grey) that were put in contact by folding and which undergo incipient shear deformation along the fold limbs. We preserved the original texture of the natural material, consisting in a scaly fabric. Gray, red, and grey/red scaly clays were tested in the triaxial apparatus in a two stage experiment consisting in two subsequent stages composed of a constant velocity step at 1 µm/s for 3-4 mm followed by a slide-hold-slide sequence. The first stage was performed at 10, 30, 50 MPa normal stress and 22 °C temperature, was followed by a hold time of ca. 2 hours in which temperature was raised to 150 °C and equilibrated across the sample, and then followed by another stage performed at 80, 100, 120 MPa normal stress and 150 °C temperature.
The grey and red lithologies showed slip strengthening behavior at all normal stress and temperature conditions, whereas the grey/red contact showed slip strengthening behavior in the low temperature stages (at all normal stresses) evolving to slip neutral-slip weakening in the high temperature stages.
The tectonic contact in the high temperature stage showed an evolution to slip weakening behavior with increasing normal stress.
To assess whether the slip weakening behavior could be represented by a higher degree of strain localization in the interface between the grey and red domains, we performed microstructural studies in a FEG-SEM hosted at the HPHT laboratory of INGV (Rome, Italy). A post mortem sample with the tectonic contact (experiment #321) was cracked open parallel to the tectonic contact. High resolution SE images on the crack showed polished areas with preferential alignment of clay minerals (Figure 1). Future microstructural work will assess whether or not strain localization occurred in the red and grey samples.

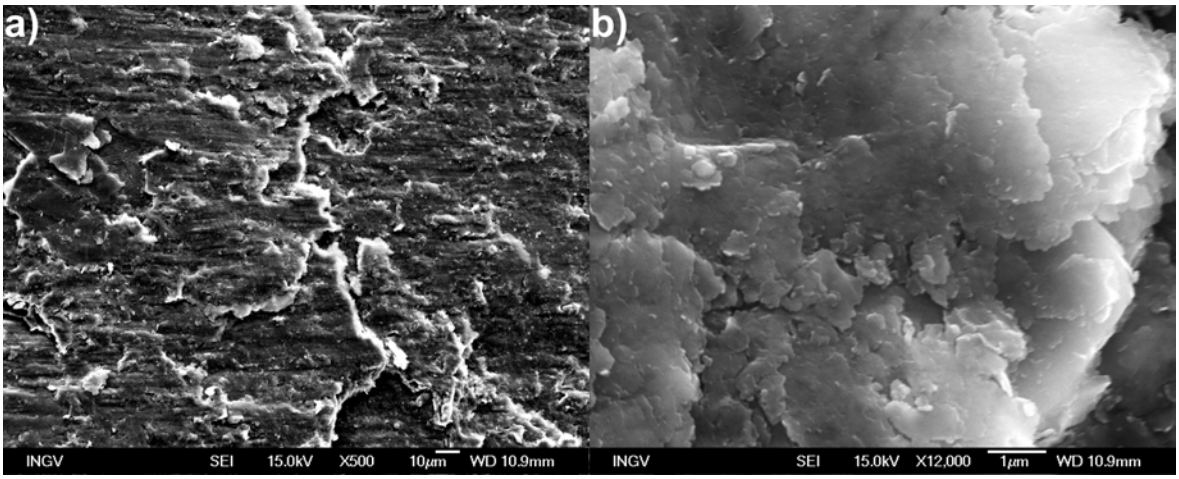

Fig. 1| Secondary electron image obtained on the crack surface parallel to the tectonic contact after the experiment #321. A) Polished surface at lower magnification. B) Preferential alignment of clay minerals is observed parallel to the surface

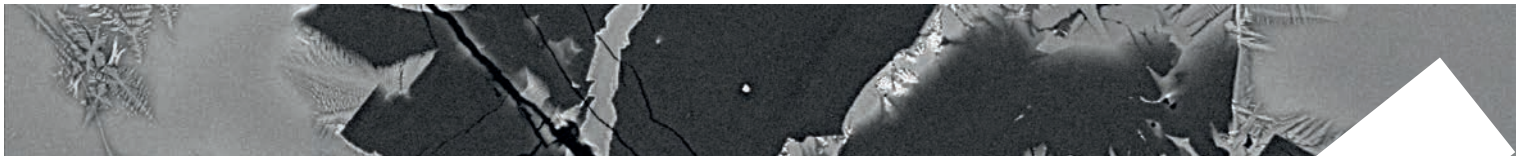

Thermal weakening friction during seismic slip: experiments and models with heat sources and sinks

Nielsen S., Spagnuolo E., Violay M., Di Toro G.

Recent experiments systematically explore rock friction under crustal earthquake conditions revealing that faults undergo abrupt dynamic weakening. Processes related to heating and weak-ening of fault surface have been invoked to explain pronounced velocity weakening. Both contact asperity temperature Ta and background temperature T of the slip zone evolve significantly during high velocity slip due to heat sources (frictional work), heat sinks (e.g. latent heat of decomposition processes) and diffusion. Using carefully calibrated High Velocity Rotary Friction experiments, we test the compatibility of thermal weakening models: (1) a model of friction based only on T in an extremely simplified, Arrhenius-like thermal dependence; (2) a flash heating model which accounts for evolution of both V and T ; (3) same but including heat sinks in the thermal balance; (4) same but including the thermal dependence of diffusivity and heat capacity. All models (Figure 1) reflect the experimental results but model (1) results in unrealistically low temperatures and models (2) reproduces the restrengthening phase only by modifying the pa-rameters for each experimental condition. The presence of dissipative heat sinks in (3) significantly affects T and reflects on the friction, allowing a better joint fit of the initial weakening and final strength recovery across a range of experiments. Temperature is significantly altered by thermal dependence of (4). However, similar results can be obtained by (3) and (4) by adjusting the energy sinks. To compute temperature in this type of problem we compare the efficiency of three different numerical solutions (Finite differences, wavenumber summation, and discrete integral).

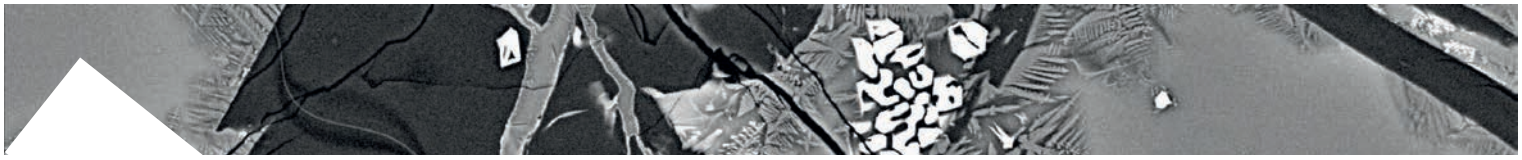

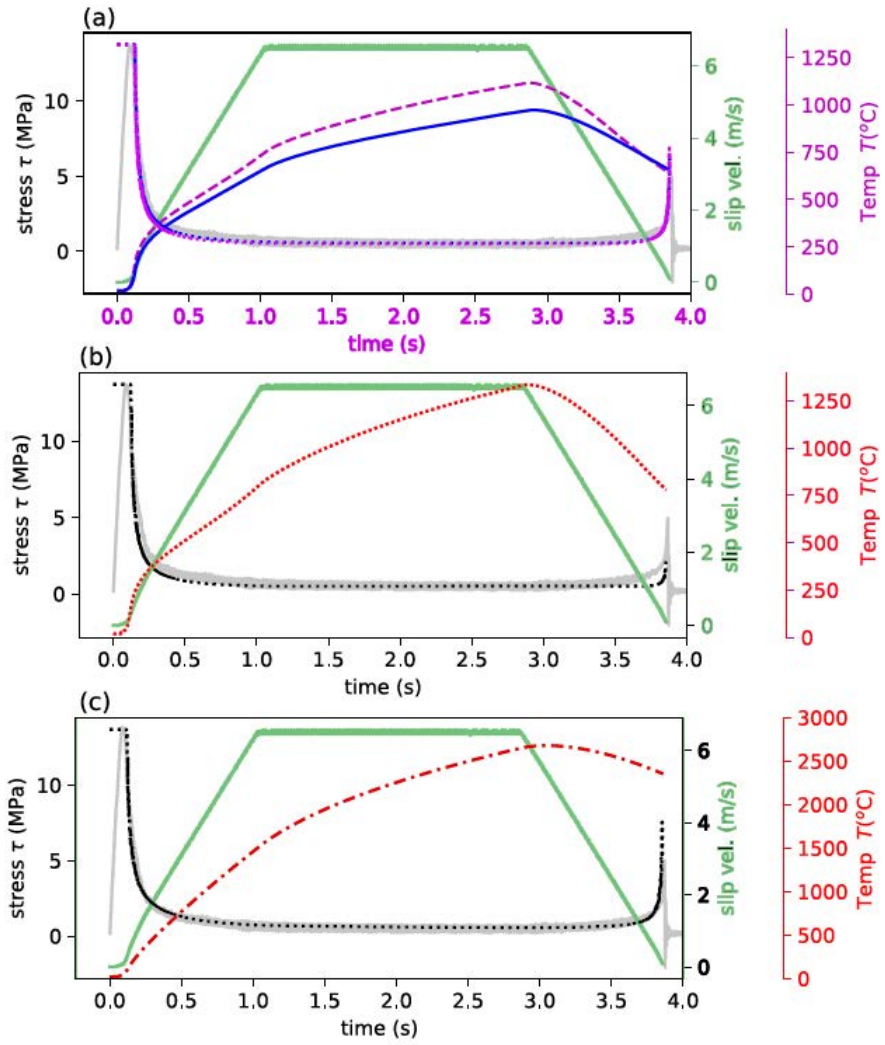

Fig. 1l Effect of thermal-dependent diffusivity and heat capacity κ,c. Experiment s308 on Carrara marble, data and model (normal stress 20MPa, target velocity 6.5 m/s, acceleration 6.5 m/s^2) (a) Purple and blue dotted curves show simulated stress evolution for models (2,3) respectively. Note that both are very similar. Grey solid curve is experimental stress. Solid blue and dashed purple represent temperature. Light green curve is experimental slip velocity. (b) Black dotted curve is simulated stress evolution for model (1). Red dotted curve is temperature. (d) A model with no heat sinks (Cs = 0) and variable κ,c also fit the data reasonably, at a substantially higher temperature, but with a different combination of friction parameters:
(Tw,B) = (3800,0.02 10^{-6}).

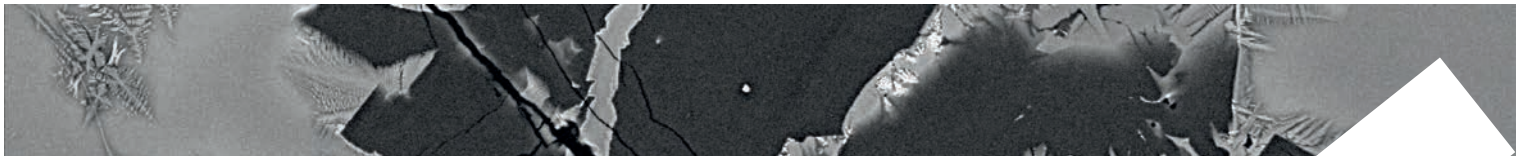

Fault friction during simulated seismic slip pulses

Harbord C., Spagnuolo E., Di Toro G., Brantut N.

Theoretical studies predict that during earthquake rupture faults slide at non-constant slip velocity. It is known that temperature evolution plays a key role in governing the strength of faults sliding at high velocity, which arises from a coupling between the sliding velocity and constitutive law of fault strength. Here we present results from high velocity friction experiments with non-constant velocity history (Figure 1), employing a well-known seismic source solution compatible with earthquake source kinematics.

The evolution of friction in experiments is unique and shows a strong dependence on the applied slip history, and parameters relevant to the energetics of faulting scale with the impulsiveness of the applied slip function.

We compare constitutive models of strength against our experimental results and demonstrate that the evolution of fault strength is strongly coupled to the temperature evolution on and off the fault. Flash heating accurately predicts weakening behaviour at short timescales, but at larger timescales data is better predicted by a model of grain size sensitive creep.

Comparison with previous experiments suggests that variable velocity experiments give a better constraint on the underlying constitutive law than experiments conducted at steady state conditions.

Strong temperature coupling highlights that careful consideration must be given to experimental boundary conditions in order to understand the underlying weakening mechanisms active during experiments. Furthermore crustal scale models must use an accurate calculation of temperature to obtain realistic models of earthquake rupture.

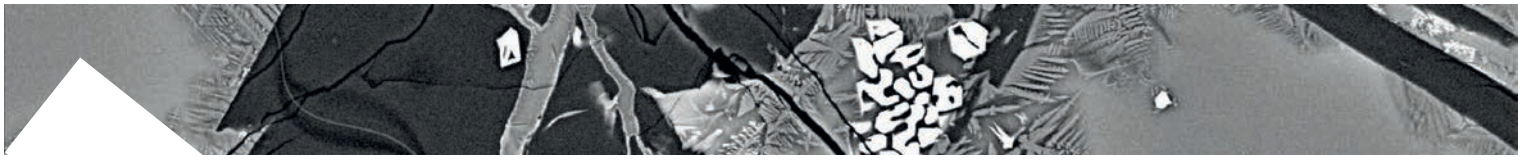

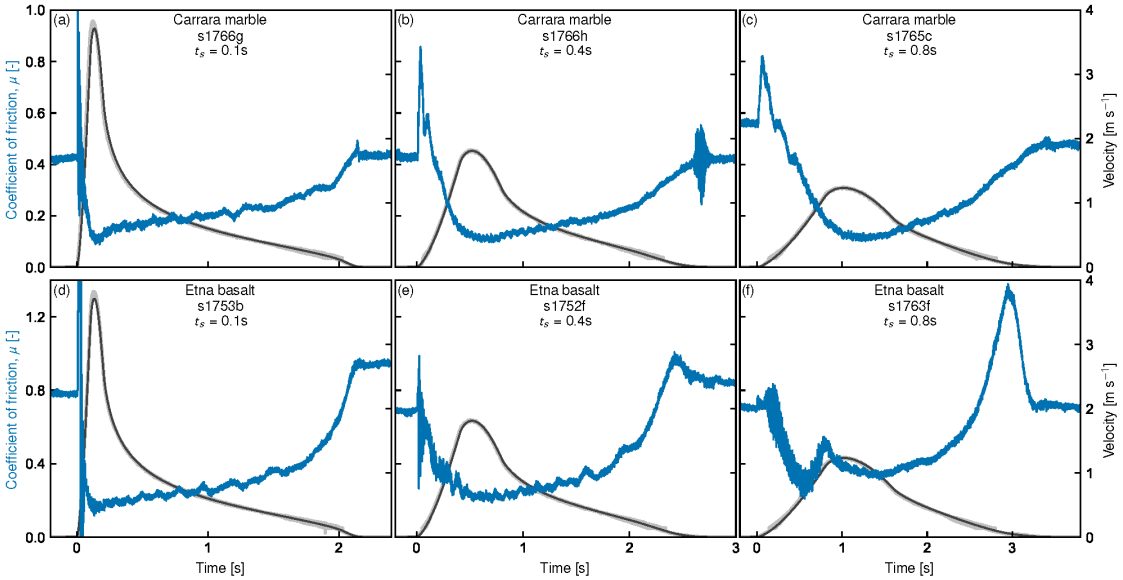

Fig. 1l Frictional response of simulated faults during application of Yoffe functions of varying smoothing time. Panels a)-c) show Carrara marble with increasing values of the smoothing time from left to right (0.1 to 0.8), panels d)-f) show Etna basalt frictional response for the same slip histories as a)-c). Velocity history is shown for reference, where the thicker grey curve represents the encoder derived velocity history, and the black the imposed control signal.

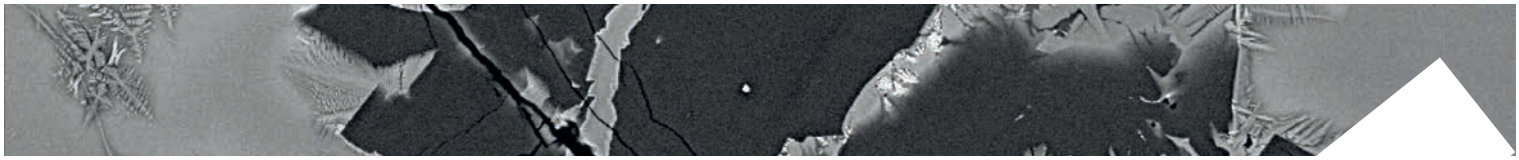

Lithological control on the shallow co-seismic slip at the Sumatra subduction zone megathrust

Spagnuolo E., Aretusini S., Vannucchi P., Di Toro G.

Rupture models of the 2004 Mw 9.2 Sumatra-Andaman EQ imply shallow co-seismic slip extending close to the trench particularly offshore the northern part of the island of Sumatra. Geophysical imaging of the Sumatran accretionary prism suggested that the shallow plate boundary interface propagates through sediments deposited in the Warton Basin near the base of the Bengal-Nicobar fan and even in pre-fan layers. However, imaging was not able to identify the precise location of the frontal megathrust, and three "candidates" for this sediment horizon were proposed in the input section. IODP Exp. 362 sampled these layers where drilling could reach them, ~225 km seaward of the deformation front, to investigate the factors controlling shallow seismogenic slip potential. We conducted an innovative set of experiments – "creep tests" – where shear stress increases stepwise until the onset of accelerated fault slip. Unlike the usual creep tests, this novel technique allows us to observe a broad spectrum of slip behaviors that spontaneously occur during faulting, from aseismic creep to accelerated slip at seismic slip rates (1 m/s). Creep tests also prevent dynamic weakening forced by the imposed seismic slip rate – i.e. at 1 m/s all materials verge toward a slip weakening behavior. These tests reveal that although all the "candidate" fault materials have a similar dynamic weakening behaviour, they differ in how they accumulate and adjust shear stress, resulting in two endmember fault stability characteristics, explained using the energy budget for rupture propagation. Specifically, we identified a pre-fan layer that can accumulate a high amount of elastic shear stress and release it all at once through a fast (>1 m/s) event – i.e. behaving like a locked fault patch. While most of the other layers, although also able to accumulate elastic shear stress, release it both by creeping and by short-lasting and fast (> 0.1 m/s) events – i.e. behaving like creeping patches which can accelerate to reach seismic slip rates. These conclusions hold if elastic strain is not released by adjacent weaker lithological units. Deformation features in the lower plate as well as in the prism, and plate flexural bending can all exert a key role in building up elastic stress favoring fault propagation – as well as fault nucleation – in the candidate décollement layer (Figure 1).

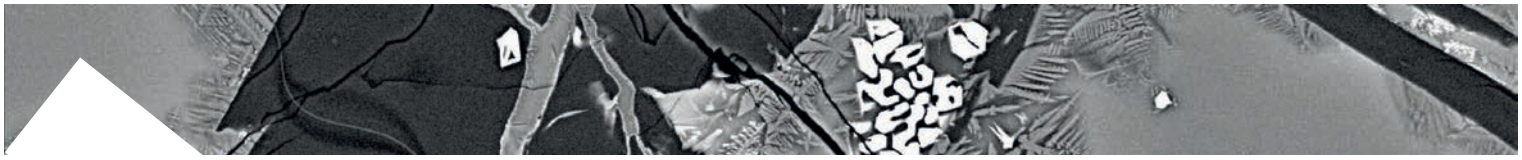

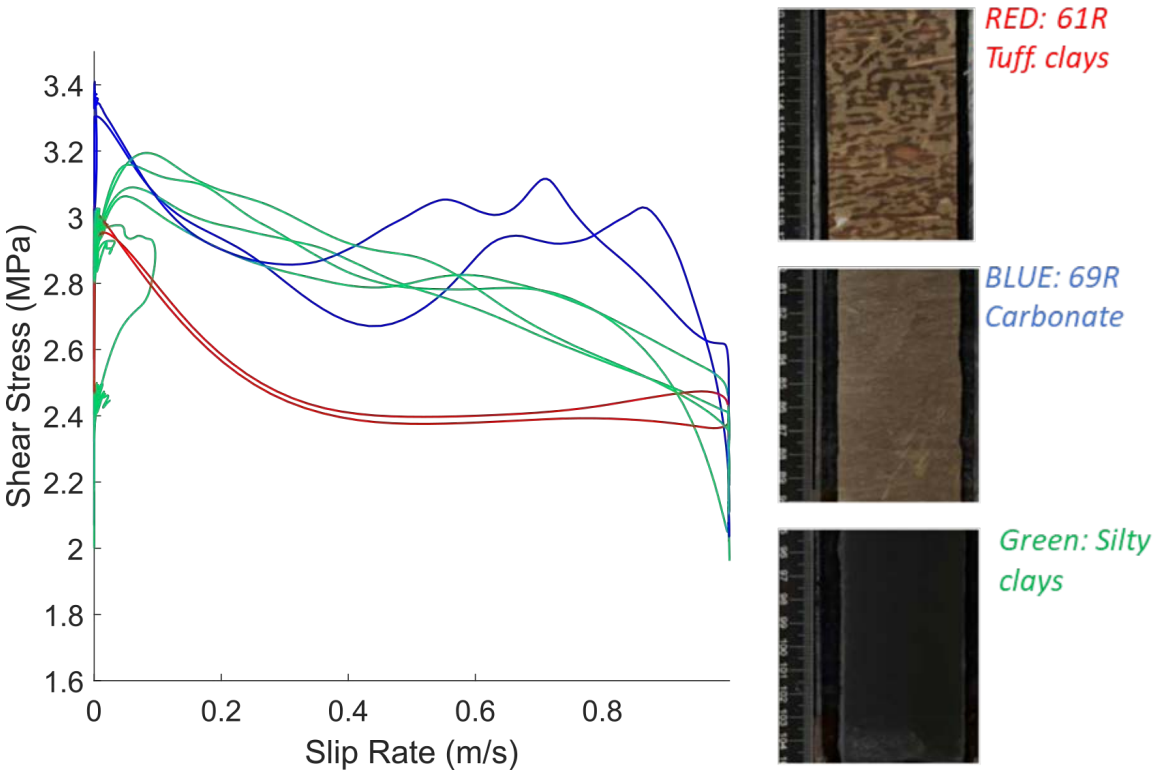

Fig. 1l Red samples (tuffaceous clays): velocity weakening, they release all stress for v<3 cm/s; from v>3 cm/s they do not accumulate stress anymore; Blue samples (carbonates): similar to red samples, but they are less efficient in releasing stress; Green samples (clay rich): are velocity strengthening until they reach velocities of 10 cm/s; from v>10 cm/s shear stress decreases as a function of velocity.

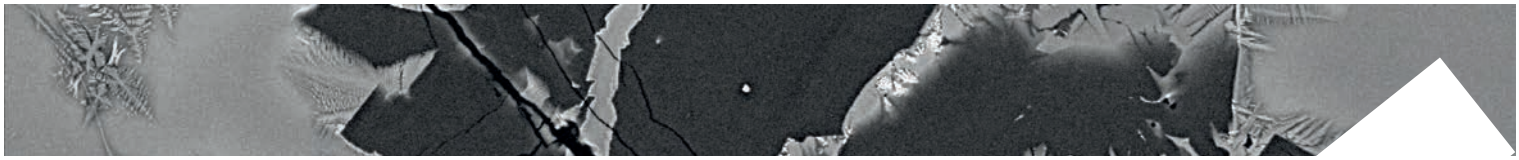

The influence of textures on the slip mode of experimental faults

Pozzi G., Scuderi M., Tinti E., Collettini C.

Recent studies proved that fault deformation can be accommodated by a wide spectrum of slip modes, which includes earthquakes and slow slip events. While frictional behaviour and inherent geometrical properties of the fault are intimately related to the nucleation phase, fault architecture seems to play a foremost role in the modulation of fault motion.
For example, distributed versus localised deformation in different materials may affect the mechanical properties of slow slip events. It is unclear, however, whether a range of failure modes may originate only as a function of textures. We therefore designed a set of shear experiments to investigate the influence of microstructures on the frictional behaviour of analogue anhydrite-dolomite-hosted fault gouges. Different equilibrium textures were formed at standard velocity of 1 µm s^{-1} at different normal stress (15 - 100 MPa). When brought at the same normal stress (35 MPa), and re-sheared at the same velocity, faults that experienced stress-up conditions are stable while stressed-down faults manifest stick-slip behaviour. The latter arises when deformation is accommodated by nanogranular principal slip zones. Depending on the grain size distribution (function of the normal stress) and cohesion of the fault, fault slip velocity follows either Yoffe-shaped (Figure 1a) or Gaussian profiles (Figure 1b), and different peak values (19 – 90 µm s^{-1}). We conclude that the textural nature of fault principal slip zones, with the combined effect of cohesion, modulate the failure mode of experimental faults.

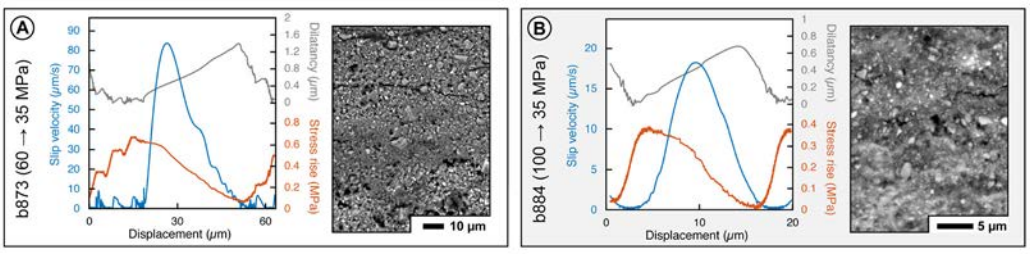

Fig. 1| Detail of the mechanical properties of repetitive stick-slip events for two experiments showing unstable behaviour and associated back-scattered SEM image of the principal slip zones (PSZs) accommodating the fault slip. A) 60 MPa texture re-sheared at 35 MPa. The velocity slip profile is asymmetric and characterized by rapid acceleration to peak. PSZ is formed by sub-micron sized grains with dispersed angular porphiroclasts (5 µm). B) 100 MPa texture re-sheared at 35 MPa. The velocity slip profile is symmetric. PSZ is homogeneous and the grain size is completely reduced below 1 µm.

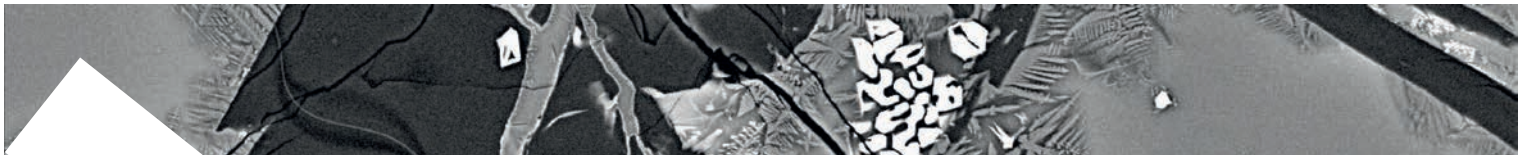

Thermally activated weakening mechanisms efficiency

Cornelio C., Spagnuolo E., Nielsen S., Aretusini S., Passelegue F., Violay M., Di Toro G.

While sliding at seismic slip-rates of ca. 1 m/s, a natural fault undergoes an abrupt decrease of its strength called dynamic weakening. Processes related to fast heating and weakening of the asperities, efficient crystal-plastic yielding, frictional melting or thermal pressurization of fluid saturated faults have been invoked to explain pronounced velocity weakening during initial slip-rate acceleration. However, few weakening mechanisms can explain the experimental evidence of fault strength recovery during the slip-rate deceleration at the end of seismic slip.
Here we present a compilation of ca. 100 experiments performed in the rotary shear apparatus SHIVA, at varying effective normal stress (5-40 MPa), slip-rates (V=0.1-6.5 m/s) and fluid pressures (from room-humidity condition, Pf=0, to Pf=15 MPa) on Etna basalt, Carrara marble, microgabbro and Westerly granite.
We analyzed the experimental results on the light of combined weakening mechanisms models (flash heating and bulk melting, flash heating and dislocation/diffusion creep and thermal pressurization). Moreover, we use a norm-based optimization routine which compares the measured shear strength during the experiments with the estimated shear strength from the models to optimize a set of model parameters. The analysis of the squared norm value of the residual (SNR) gave us the opportunity to evaluate the efficiency of the combined mechanisms.
Our results showed that:

1) For flash heating and bulk melting model, the norm value increase with the increase of the melt complexity;

2) For Carrara marble, the flash heating and diffusion creep model had lower norm value than the flash heating and dislocation creep model;

3) Under fluid pressurized conditions, the experimental data cannot be explained with thermal pressurization model, for which the norm value was on the order of ~104.

Moreover, the modelling procedure allowed us to detect the slip-switch d0, i.e. the slip necessary for the complete activation of the bulk weakening mechanism taking over the asperity scale weakening mechanism. Our results showed that:

1) The d0 is decreasing by increasing the effective normal stress acting on the fault;

2) For the same weakening mechanisms, the d0 is a function of rock lithology;

3) Flash heating law can be used for representing with good approximation small magnitude earthquakes, but with increasing depth bulk weakening models have to be included..

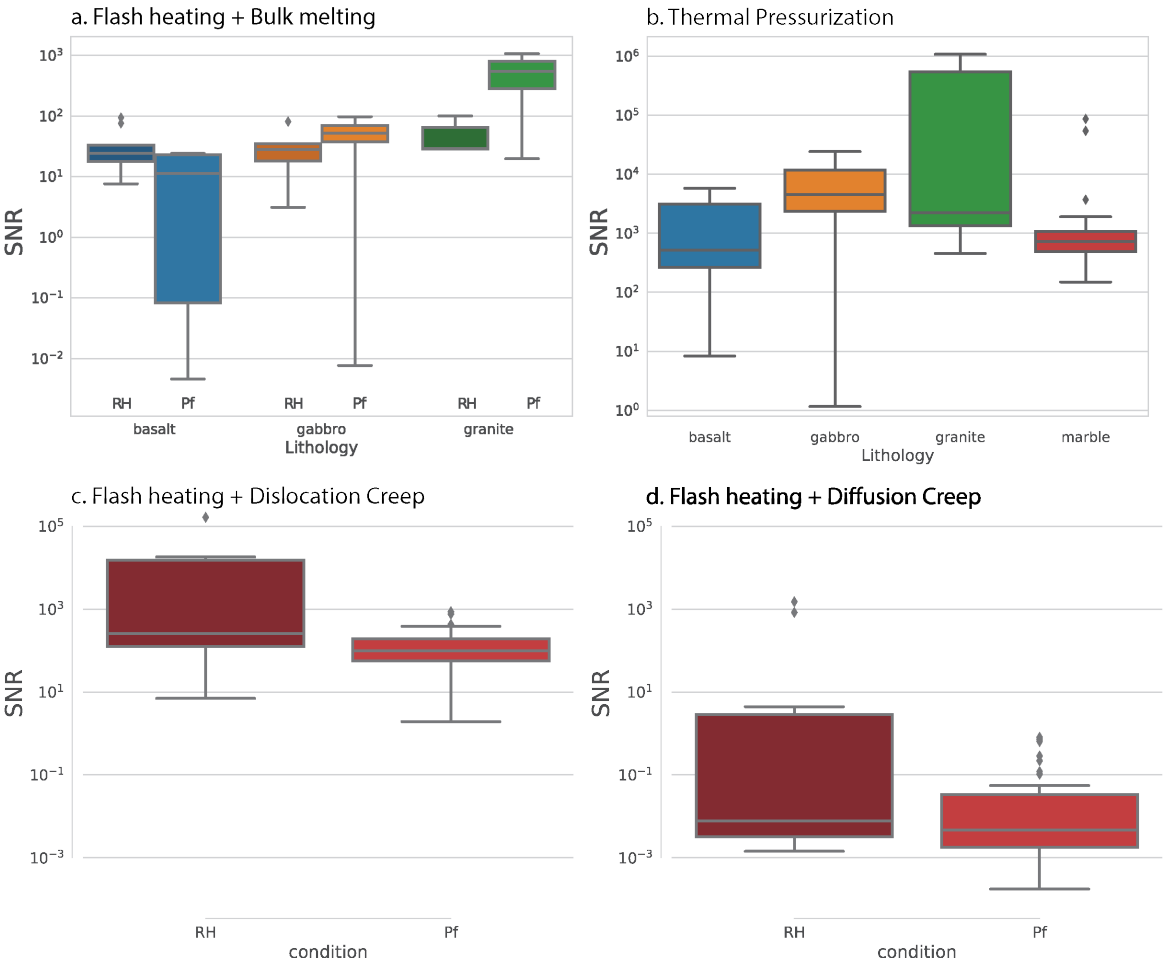

Fig. 11 Boxplots for the error of the optimization models. The SNR is a measure of the goodness of the fit of the experimental curve by the proposed model, lower was the SNR, better was the fit of the experimental curve. We propose to use the SNR as a parameter for determining the efficiency of the mechanisms represented by the models. a) SNR of the flash heating and bulk melting model as a function of the sample lithology (Etna basalt, microgabbro, Westerly granite) and the experimental condition (room-humidity RH or with fluid pressure Pf). The median lower SNR was for basalt experiments, while the higher SNR was for westerly granite experiments. b) Boxplots of the SNR for thermal pressurization model for all analyzed lithologies. The median SNR is higher than 103 for all the lithologies, suggesting that thermal pressurization was not a valid weakening mechanism for our experiments. c-d) Boxplots of the SNR for flash heating and dislocation creep model and flash heating and diffusion creep model for experiments performed on Carrara marble samples. Comparing the values of the SNR we can observe that it was lower for the flash heating and diffusion creep model (median values of 0.0078 and 0.0047, for room humidity and fluid pressurized experiments, respectively) than the one for flash heating and dislocation creep model (median values of 256.0 and 98.7, for room humidity and fluid pressurized experiments, respectively).

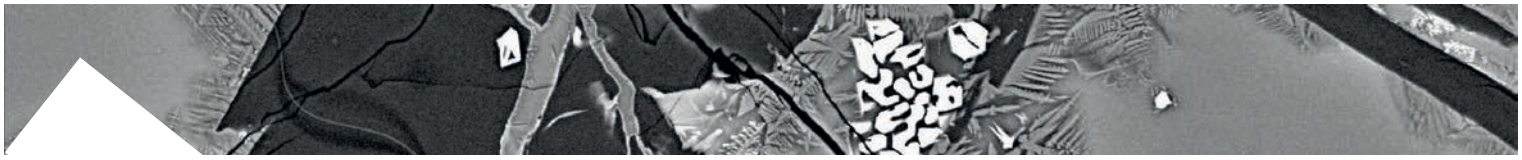

Frictional properties of Apennine basement rocks

Volpe G., Pozzi G., Collettini C., Scuderi M.

Recent seismological studies of the Amatrice-Norcia sequence highlighted microseismicity at depth comparable to the top of the crystalline basement. This microseismicity suggest the presence of a basal shear zone (BSZ) comprised between 10 and 12 km, gently dipping to east.
This microseismicity precedes and seems to migrate toward the hypocentral area 8 months prior to the mainshock. By the analysis of the seismicity preceding the 26 August mainshock, variations of the tectonic loading rate are detected along this BSZ and interpreted as the loading process promoting unclamping of the overlaying seismogenic high-angle normal faults.
It is therefore plausible that the properties of the crystalline basement play an important role in the mechanism of Apennine earthquake as in Amatrice-Norcia 2016 seismic sequence. However, what it is known about the apenninic crystalline basement is fragmentary and often based on indirect evidences. In particular, it is unknown its mineralogy and associated mechanical properties.
To fill this knowledge gap we have characterised the mineralogical and frictional properties of the crystalline basement of central-northern Apennines cropping out in Mt. Romani. Four shear experiments were performed in the bi-triaxial apparatus BRAVA (INGV, Rome) using rock powders of selected basement samples. Mineralogical and microstructural analysis of natural and experimental samples have been carried using X-ray diffraction (University of Siena) and SEM imaging (La Sapienza university, Rome), respectively.
Sheared samples achieve a steady state friction coefficient of ~0.4 (Figure 1), display velocity strengthening behaviour ($a-b > 0$) and low healing rates ($\beta = 0.0019$). Sampled rocks composition consists mainly of phyllosilicates (muscovite and minor chlorite) and lesser quartz. Microstructural analysis shows that slip is mainly accommodated by sliding along aligned phyllosilicates foliae (Figure 1, yellow lines), which is consistent with the observed friction coefficients.
With future experiments we will further investigate i) the influence of mineralogical anisotropy, observed within the basement sequence, on the frictional properties (i.e. gouges with variable mineralogy) and ii) the role of existing textural anisotropy on re-shear of intact rock samples.

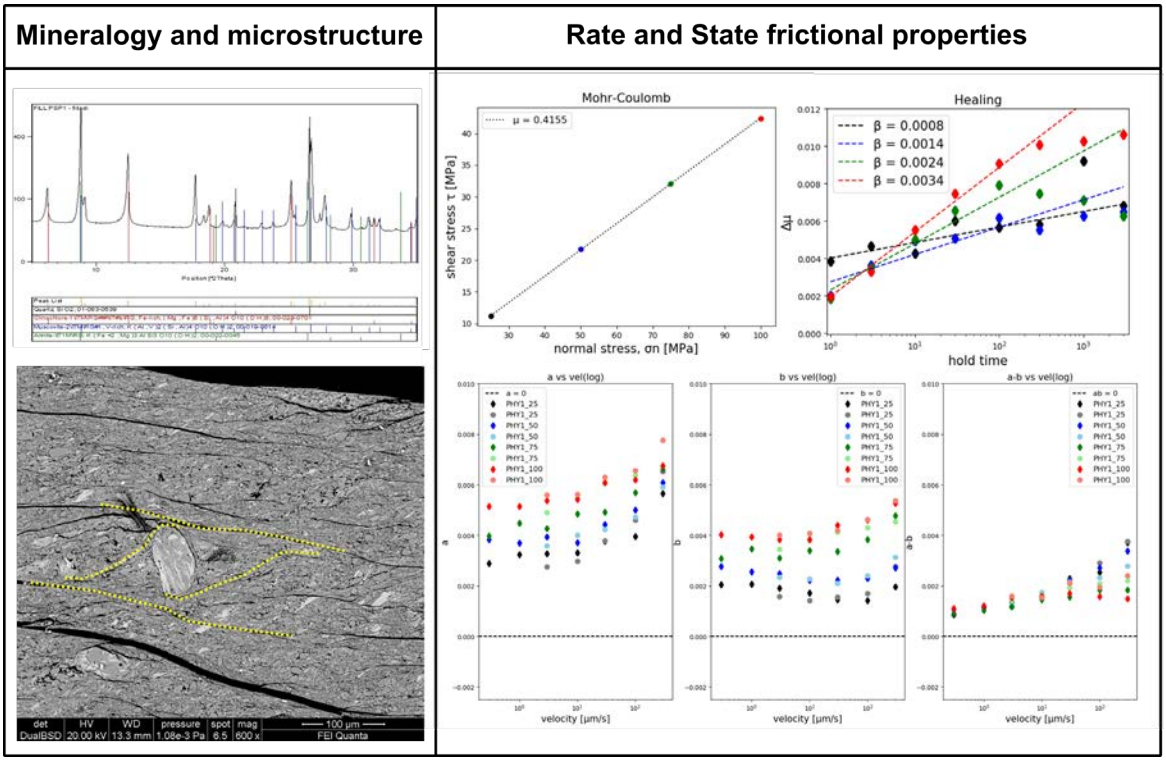

Fig. 11 Left panel: results of X-ray powder diffraction (top) and back scattered image of the post-mortem shear zone developed during experiment in selected rock gouges (bottom). Sense of shear of microstructures is top to the right. Right panel: Summary of the frictional properties measured during experiments.

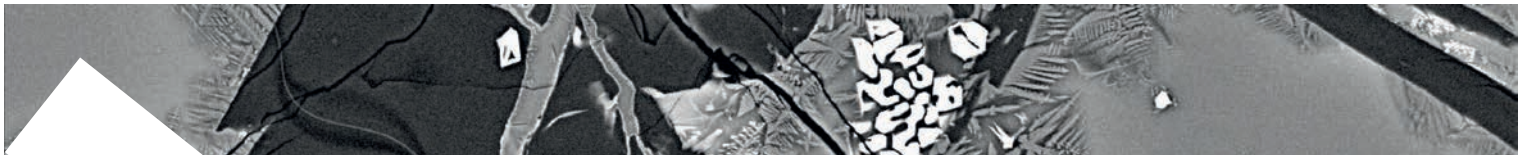

Frictional properties of Opalinus Clay: influence of humidity, normal stress and grain size

Bigaroni N., Scuderi M., Pozzi G., Collettini C.

The Opalinus Clay (OPA) is an argillaceous formation that is being considered as potential host rocks for repositories of radioactive waste in Switzerland. If on the one hand its low permeability makes it an excellent candidate, on the other hand the presence of faults inside the formation can compromise its long-term hydrological isolation. Therefore, it is of fundamental importance to study the frictional behavior of the OPA in relation to the variation of permeability. Preliminary studies conducted on the host rock have shown how OPA exhibits a frictional behavior characterized by aseismic slip. However still only a small spectrum of experimental conditions was explored.
For this reason, we have put together an experimental dataset aimed at exploring the frictional response of OPA following the variation of parameters such as humidity, grain size and normal stress. Sieved host rock powders with two different grain sizes, both wet and dry, were sheared in double-direct configuration, at different normal stresses conditions (10, 20, 35 and 50 MPa).
We observe that these tree parameters cause first order variation in friction coefficient both for peak friction "μ_{peak}" and steady-state friction "μ_{ss}" (Figure 1a). Experiments performed at 100% humidity exhibit systematically lower μ_{peak} and μ_{ss} compared to the dry ones. The increase in normal stress promotes the decrease of both μ_{peak} and μ_{ss}, and for high normal stresses the difference between μ_peak and μ_ss is decreased. Samples with a lower initial grain size show higher friction values than those with a higher initial grain size, and this effect is enhanced as normal stress increases. Moreover, the analysis of velocity-steps in the light of Rate- and State-friction framework shows that the frictional parameter, expressed as "a-b", is always positive and it increases with the increase of sliding velocity (Figure 1b). Whereas, the critical slip distance "Dc" decreases with the increase of sliding velocity and is systematically higher for experiment conducted at 100% humidity (Figure 1c).
Taken together these results let us conclude that, although we observe first order variation of both μ_{peak} and μ_{ss} friction coefficient, the effect of humidity and grain size does not influence the frictional stability of the Opalinus Clay in the range of pressure we examined. Although the dependence of "Dc" on both velocity and humidity let us hypnotize that more complex micromechanical mechanisms can be involved in the process. Therefore, further studies are needed to explain this behavior in the light of dilatancy and porosity changes.

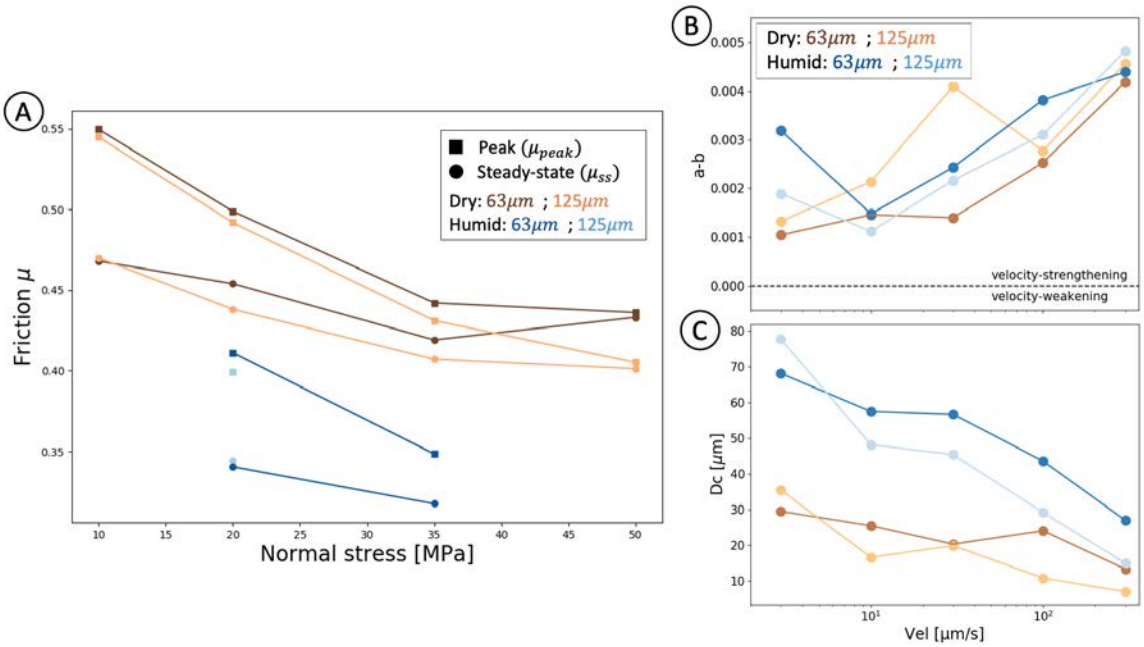

Fig. 1| Frictional behavior of Opalinus Clay (OPA), at different conditions of humidity, grain size and normal stress. Brown colors are for "dry" experiments and Blue colors are for 100% humidity ones. Brown colors indicate "dry" experiments while blue colors indicate 100% humidity experiments. Colors of a darker hue indicate powders at an initial particle size below 63 μm while lighter colors indicate a particle size between 63 μm and 125 μm. A). First order changes of peak "μ_{peak}" (squares) and steady-state "μ_{ss}" (circles) friction coefficients with the increase of normal stress. B) Evolution of the frictional parameter "a-b" with velocity, at constant normal stress of 20 MPa with different grain sizes and humidity conditions. C) Evolution of Critical Slip Distance "Dc" with velocity, at constant normal stress of 20 MPa with different grain sizes and humidity conditions.

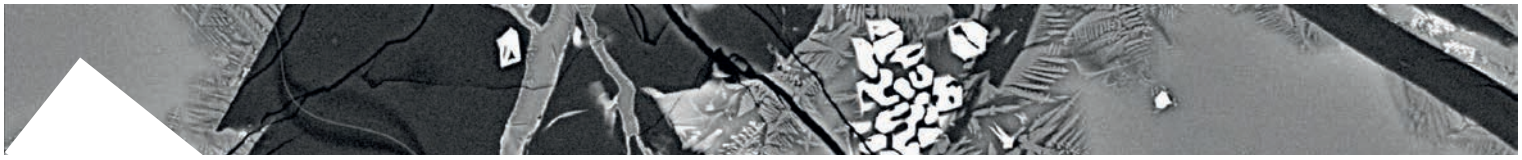

8.3 TECHNOLOGY

HERMES HEmera Returning MESsenger

Romeo G., Lepore A., Iarocci A., Spinelli G., Vallocchia M., Mari M., Di Stefano G.

Why HERMES? HERMES (HEmera Returning MESsenger) aims to transfer data and samples from a stratospheric balloon to the ground through an automatic motor glider (the aircraft carries a copy of the computer disk on board).
The control of operations (the ground station) can decide its recovery through a command via a satellite channel, after uploading the coordinates of the landing point to the autopilot. At this moment the aircraft is able to glide for more than 200 km (see Figure 3) in calm air, therefore the reachability of the landing point is a function of the wind conditions along the trajectory.
Project evolution
The interaction with the Swedish launchers highlighted the impossibility of sharing the flying gondola with other scientific experiments, linked to two considerations: the release of a load can change the attitude of the gondola and be a source of disturbance and HERMES makes generous use of equipment capable of generating RF disturbances.
In order to increase efficiency, the glider has been enriched with a tail engine. The result of the flight test, conducted in Benevento, showed that the presence of the engine helps the aircraft to get into flight attitude, which stabilizes at around 20 km of altitude, compared to 10 km achieved with flights without engines. Figure 1 shows the trend of vertical speed in the experimental flight of the glider equipped with the engine, while Figure 2 shows the trend of the distance from the base and of the altitude of the flight.

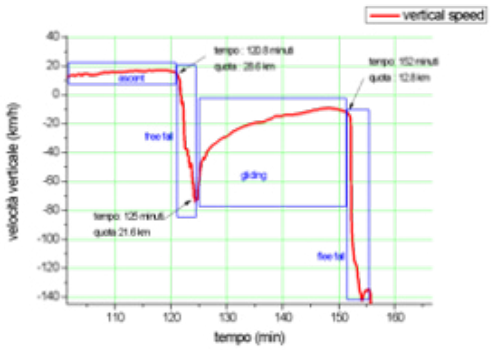

Fig. 1| Trend of the vertical speed.

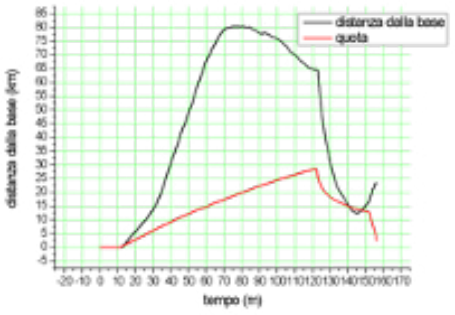

Fig. 2| Trend of the distance from the base and of the altitude.

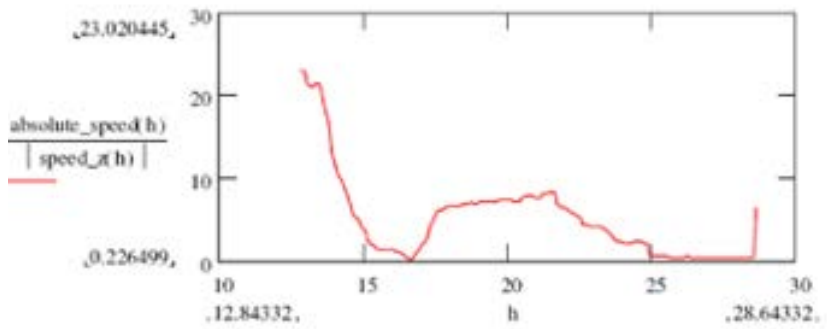

Fig. 31 Glider efficiency vs. height

Figure 3 shows the glider efficiency (horizontal speed/vertical speed vs. height), calculated from the flight test data.
The graph shows an efficiency greater than 20 at 13 km, this allows the glider to fly more than 200 km.
The first experimental flight is scheduled in Sweden for summer 2021.
The flight must be short (few hours) because the air rules for UAVs in Sweden do not allow an experimental automatic aircraft to travel too far from the launch point.
Modular design HERMES is built in the name of modularity. This choice was designed to:

-Make modules usable separately in other balloon projects; -Make debugging easy;

-Make the project updatable: if a module is technically obsolete it can be replaced with an updated module that respects the functionality, with a minimum redesign of both HW and SW.

-Easily add new features. All modules communicate on the bus and use the same connectors so you can add functionality simply by adding a module.

In Figure 4 it is shown the overall view without solar panels; in Figure 5 the payload frame, made by the mechanical workshop of LNTS.
In Figure 4 it is shown the overall view without solar panels; in Figure 5 the payload frame, made by the mechanical workshop of LNTS.
Ready equipment
The modules developed so far by LNTS are now described briefly. They are modules that are part of the balloon side instrumentation (Figure 6).
The battery pack manages the system power supply (Figure 8), keeping the batteries (Figure 7) in the correct state of health.
The SD module records a flight log. Allows system debugging using a serial interface that can be connected to a PC.
The releaser (Figure 9) module checks the

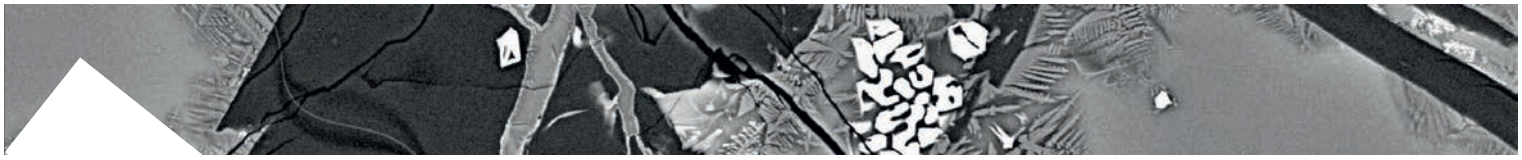

glider detachment operations: detachment of the umbilical connector, removal of restraints, thrust. The flight computer simulator produces synthetic data with which to fill the SSD, simulating the presence of a flight computer. A camera records a movie of the flight.

The glider charger + junction box (Figure 10) provides communication through the umbilical connector, connects the SSD to the flight computer simulator and keeps the glider's battery charged and warms it if necessary.

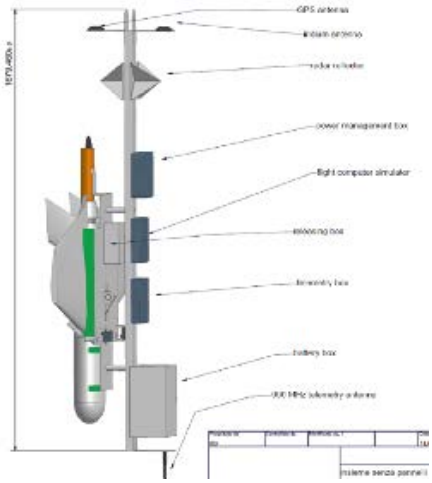

Fig. 4| The overall view of the payload

Fig. 5| The payload frame.

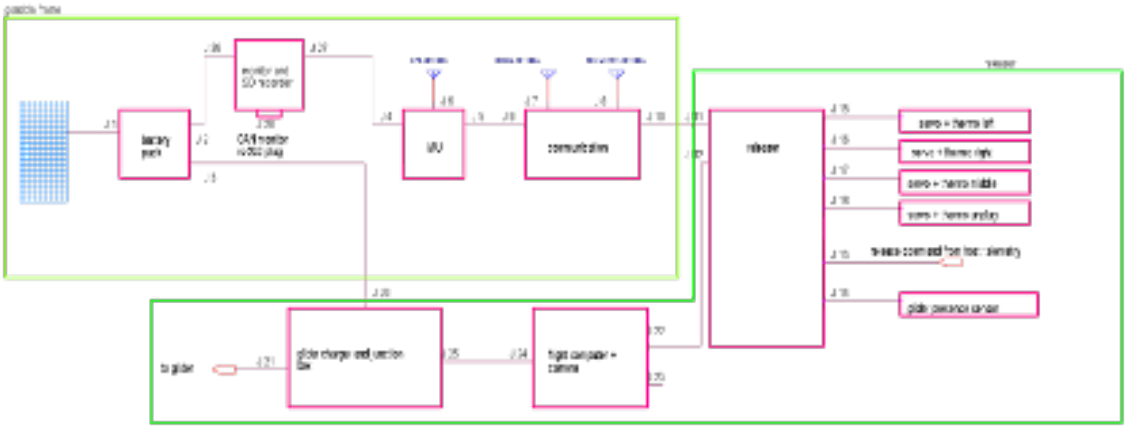

Fig. 6| Summary block diagram of the launch platform.

Fig. 7| A detail of the battery box.

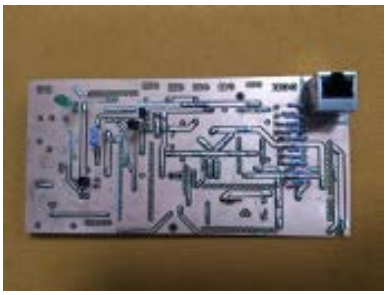

Fig. 8| The PCB of the battery pack electrical circuit.

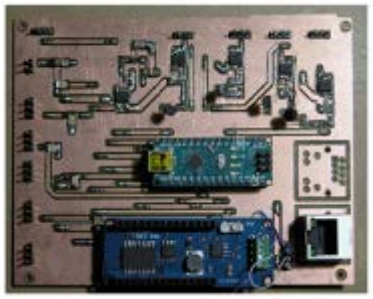

Fig. 9| The releaser module.

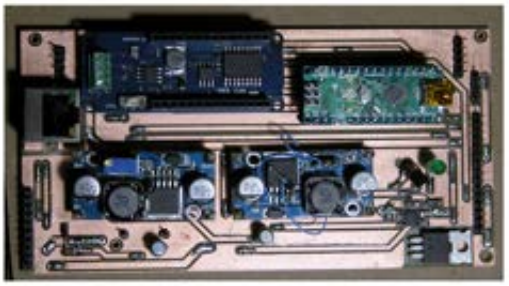

Fig. 10| The glider charger + junction box.

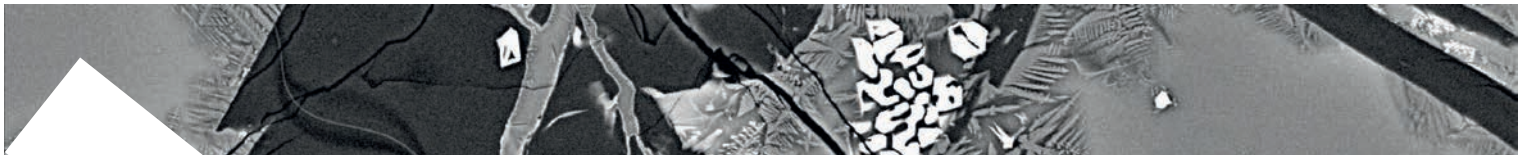

Relative humidity sensors comparison inside a radon chamber

Pongetti F., Galli G., Mari M.

Commercial radon-in-air measuring devices are calibrated at our Radionuclide Lab. facility using an original equipment (radon chamber, detector, etc.) developed at INGV. Our goal is to simplify the calibration procedures by automating some time consuming processes. To do so we are selecting relative humidity (RH) digital sensors.
Relative humidity and temperature of the air are parameters needed to calibrate radon measuring devices that use a semiconductor diode as a detector. As a matter of fact, humidity hampers the collection onto those detectors of alpha emitting short lived radon daughters.
The chip-sensor BME280 (capable of measuring RH, pressure and temperature of the air) has been tested and compared versus two already known measuring devices as the Algade RAD7 instrument and the Extech RHT50 probe. All of them being simultaneously connected to a radon chamber.
BME280 chip is wired to a RaspberryPi computer board for control and data acquisition (Figure 1a). Also a sealed aluminium housing for in-line-piping insertion of the sensor (Figure 1b) has been manufactured at our mechanical workshop.
During the test, the humidity in a radon chamber has been cyclically increased and decreased by using a humidification and drying system.
The data analysis from all acquisitions (Figure 2) shows that BME280 has the better-shaped curves of the three and could be suitable for integration in our under development automatic system.

Fig. 1l . (a) Acquisition board based on RaspberryPi and BME280 chip-sensor which measures air parameters: RH, pressure, temperature. (b) BME280 sealed housing, employed for pipe in-line insertion of the device.

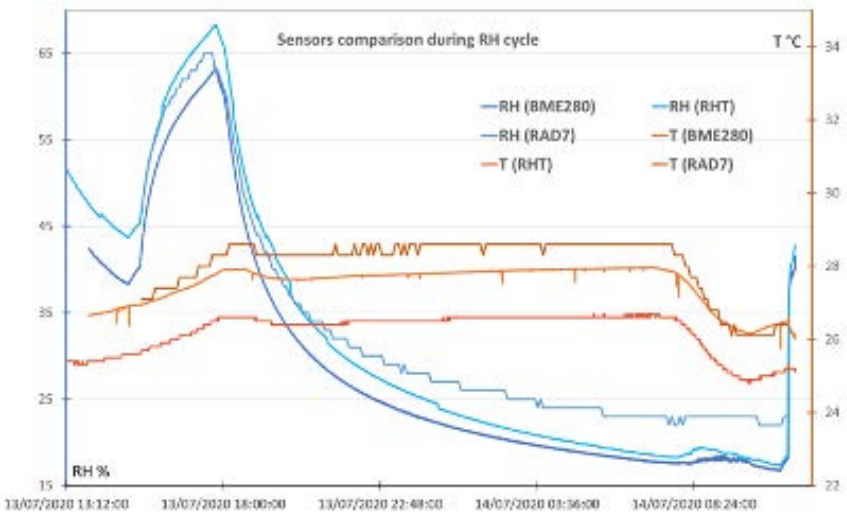

Fig. 21 Data comparison of three different devices measuring air RH and temperature (pressure acquired but not shown for simplicity) during humidification and drying cycle in a sealed radon chamber. (Blue-tone color: RH; red-tone color: temperature).

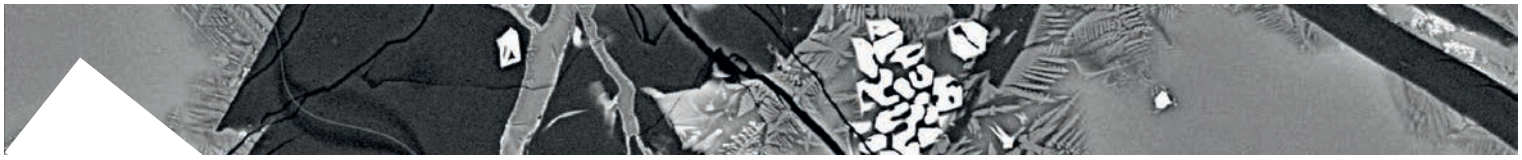

Seminars

Di Toro G. | I terremoti: fisica, previsione e pericolosità | Liceo Scientifico Messedaglia Verona, 17 Gennaio 2020.

Di Toro G. | I terremoti: fisica, previsione e pericolosità | Liceo Classico E. Montale San Donà (Venezia), 20 Gennaio 2020.

Di Toro G. | Il ciclo sismico in laboratorio (il sistema massa più molla) | Liceo Scientifico A.Cornaro, Padova, 23 Gennaio 2020.

Di Toro G. | Come nascono i terremoti | Liceo Scientifico e Linguistico IIS Ferrari Este (Padova), 24 Gennaio 2020.

Ricci T. | Cosa succede a Stromboli e ai Campi Flegrei | Lectiones magistrales "Renato Funiciello" 2019-2020, Tivoli (Roma), 29 Aprile.

Teaching

De Astis G. | Corso semestrale di "Inglese per Scienze della Terra" | Laurea triennale A.A. 2019-2020 Università di Roma La Sapienza

Training

1. **Aretusini S.** | Grant | Experimental studies of frictional properties of water- and fluid-rich gouges. ERC CoG NOFEAR.

2. **Cantonetti M.** | Stage | Analisi di video ad alta velocità dell'attività esplosiva di tipo stromboliano Supervisors: Taddeucci J. - INGV Roma1| Palladino D.M. - Sapienza University of Rome

3. **Gomila R.** | Grant | Architecture of fault zones in the continental crust: geological constraints. ERC CoG NOFEAR.

4. **Harbord C.** | Grant | Experimental studies of elastic properties and attenuation of fault zones. ERC CoG NOFEAR

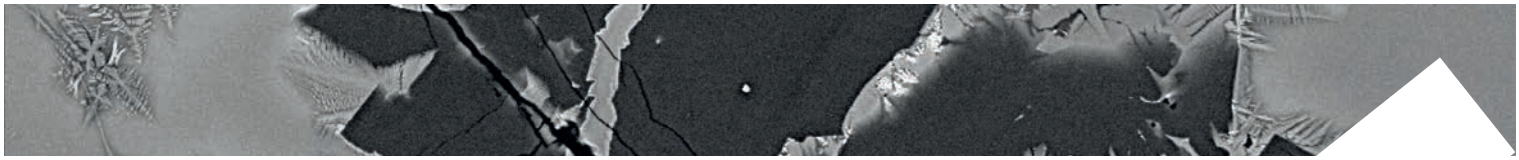

5. **Pennacchia F.** | Stage | High speed cameras and field deployment at Stromboli volcano
Supervisors: Del Bello E. - INGV Roma1 | Vona A., Università Roma Tre

6. **Valentini F.** | Stage | Analisi video ad alta velocità dell'attività esplosiva di tipo stromboliano
Supervisors: Taddeucci J. - INGV Roma1 | Palladino D.M. - Sapienza University of Rome

Thesis

1. **Amodio A.** | Master Thesis | Caratterizzazione delle proprietà dell'attrito delle serpentiniti ricche in Antigorite
Supervisors : Collettini C.- Sapienza University of Rome | Pozzi G. - INGV Roma1

2. **Bersan E.** | Master Thesis | Field and microstructural investigation of extensional faults in bituminous dolostones (Fornaca Valley, Central Apennines, Abruzzo)
Supervisors: Di Toro G. - Dipartimento di Geoscienze, Università degli Studi di Padova | Fondriest M. Institut des Sciences de la Terre (ISTerre), Université, Grenoble Alpes, Grenoble, France

3. **Cantonetti M.** | Master Thesis | Studio sperimentale dei getti supersonici e loro implicazioni per le eruzioni vulcaniche Stromboliane
Supervisors: Taddeucci J. - INGV Roma1 | Palladino D.M. - Sapienza University of Rome

4. **Falcone E.** | Master Thesis | Studio delle variazioni spazio-temporali dell'attività esplosiva ordinaria a Stromboli mediante analisi di immagini termiche IR ad alta frequenza
Supervisors: Del Bello E. - INGV Roma1 | Palladino D. – Sapienza University of Rome

5. **Lombardi F.** | Analisi micro-tessiturale delle fontane dell'Etna: Implicazioni per la stima delle velocità di risalita del magma nel condotto vulcanico
Supervisors: Mollo S. and Moschini P. - Sapienza University of Rome

6. **Moltoni R.** | Triennale Thesis | Caratterizzazione di rocce di faglia sperimentali |
Supervisors: Collettini C. and Ruggieri R.– Sapienza University of Rome

7. **Panunzi S.** | Master Thesis | Studio sperimentale dei getti supersonici e loro emissioni acustiche nelle eruzioni Vulcaniche Stromboliane
Supervisors: Taddeucci J. - INGV Roma1 | Palladino D.M. - Sapienza University of Rome

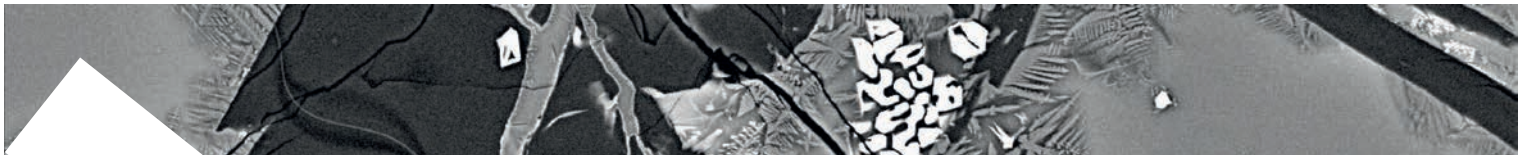

8. **Pilotti S.** I **Master Thesis I Caratterizzazione delle eruzioni Stromboliane attraverso l'analisi di video ad alta velocità**
   Supervisors: Taddeucci J.- INGV Roma1 I Palladino D. – Sapienza University of Rome

9. **Valentini F.** I **Master Thesis I Dinamiche delle eruzioni dello Stromboli dell'estate 2019 sulla base dei prodotti dei social media**
   Supervisors: Taddeucci J.- INGV Roma1 I Palladino D.M. - Sapienza University of Rome

10. **Volpe G.** I **Master Thesis I Caratterizzazione delle proprietà di attrito di rocce di basamento alpino**
    Supervisors: Collettini C. - Sapienza University of Rome I Pozzi G.- INGV Roma1

PhD

1. **Benà E.** I PhD I **Tectonic control on enhanced geogenic radon as a first order factor in radon hazard assessment I Padua University**
   Supervisors: Ciotoli G., Sassi R. - CNR I Spagnuolo E., INGV Roma1

2. **Bigaroni N.** I PhD I **Riprodurre il ciclo sismico di una faglia complessa in laboratorio e predire l'andamento con il machine learning**
   Supervisor: Scuderi M. – Sapienza University of Rome

3. **Del Rio L.** I PhD I **Mechanism of formation of slip surfaces in carbonate-built rocks: seismic faulting vs. Deep Seated Gravitational Slope Deformation**
   Supervisor: Di Toro G. – Università di Padova I co-supervisor Fondriest M., Saroli M., Gori S., Falcucci E., Moro M.

4. **Giacomel P.** I PhD I **Laboratory investigation on the frictional properties of basalts interacting with H_2O- and CO_2-rich fluids and implications for CO_2 storage**
   Supervisors: Collettini C. - Sapienza University of Rome I Spagnuolo E. – INGV Roma1 I Di Toro G. – Università di Padova

5. **Lang S. D.** I PhD I **Kinetic aspects of major and trace element partitioning between olivines and melt during solidification of terrestrial basaltic materials**
   Supervisors: Mollo S. - Sapienza University of Rome I Lyderic L. – CRPG-CNRS Nancy

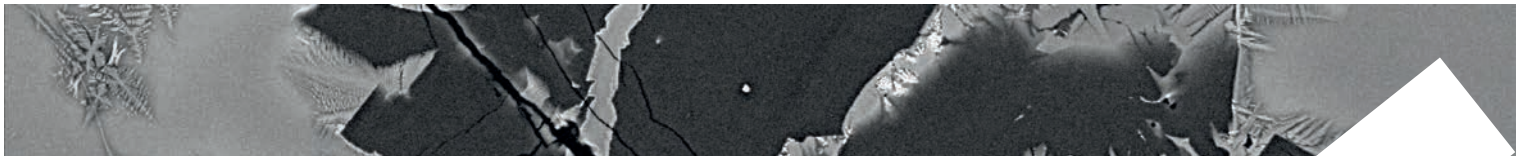

6. **Masoch S.** I PhD I **Structure, evolution and deformation mechanisms of large displacement seismogenic faults in the continental crust**
   Supervisor: Di Toro G. I co-supervisor: Pennacchioni G., Cembrano J.

7. **Mercuri M.** I PhD I **Struttura e comportamento meccanico di zone di faglia carbonatiche in presenza di plaghe argillose**
   Supervisors: Carminati E., Collettini C. - Sapienza University of Rome

8. **Moschini P.** I PhD I **Volcanic hazard assessment at Mt. Etna: a time-integrated, polybaric and polythermal perspective**
   Supervisors: Gaeta M. - Sapienza University of Rome I Scarlato P. - INGV Roma1

9. **Palummo F.** I PhD I **Reconstruction of the intensive variables and magmatic architecture of Vulcano island (Aeolian Arc, Italy)**
   Supervisors: Mollo S. - Sapienza University of Rome I De Astis G. - INGV Roma1

10. **Ruggieri R.** I PhD I **Experimental investigation on fault stability of clay-bearing carbonate fault rocks**
    Supervisors: Scuderi M., Trippetta F. - Sapienza University of Rome

11. **Stopponi V.** I PhD I **Rheology, structure and ascent rate of volatile-bearing magmas at Earth's upper mantle conditions**
    Supervisor: Stagno V. - Sapienza University of Rome

12. **Volpe G.** I PhD I **Proprietà dell'attrito e permeabilità di faglie in basamento per una migliore caratterizzazione del loro potenziale sismogenico**
    Supervisor: Collettini C. - Sapienza University of Rome

13. **Wei F.** I PhD I **Investigation of seismic slip in experimental faults under hydrothermal conditions. Chinese Government Scholarship**
    Supervisor: Di Toro G. - Università di Padova

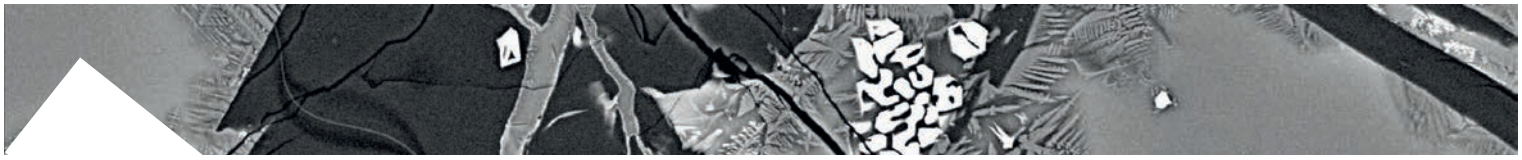

10| VISITING SCIENTISTS

Due to the pandemic situation visiting and travelling were strongly discouraged. We only had one visitor late January, one month before the general lockdown.

Feng Wei | Beijing Computational Science Research Center | Beijing China | Jan 2020

11| MEETINGS, WORKSHOP and SYMPOSIA

Meetings and sessions organization

Cities on Volcanoes Heraklion

Heraklion, Greece | 23-27 May

Del Bello E., Di Traglia F., Scarlato P., Andronico, D.
Special session 'Impact of volcanic activity in places of tourist interest: the 2019 paroxysmal eruption of Stromboli Volcano (Italy) and other case studies'
POST-PONED DUE TO COVID-19

Meetings and sessions attendance

VMSG Conference

Plymouth, UK | 6-9 January

Di Stefano F., Mollo S., Blundy J., Scarlato P., Nazzari M., Bachmann O.
The effect of CaO on the partitioning behavior of REE, Y and Sc between olivine and melt: implications for basalt-carbonate interaction processes

Di Stefano F., Scarlato P., Mollo S., Petrone C.M., Ubide T., Nazzari M., Andronico D.
Mush cannibalism and disruption recorded by clinopyroxene phenocrysts at Stromboli volcano: new insights from recent 2003-2017 activity

Palummo F., Mollo S., De Astis G., Di Stefano F., Nazzari M., Scarlato P.
Reconstruction of the intensive variables and magmatic architecture of Vulcano island (Aeolian Arc, Italy)

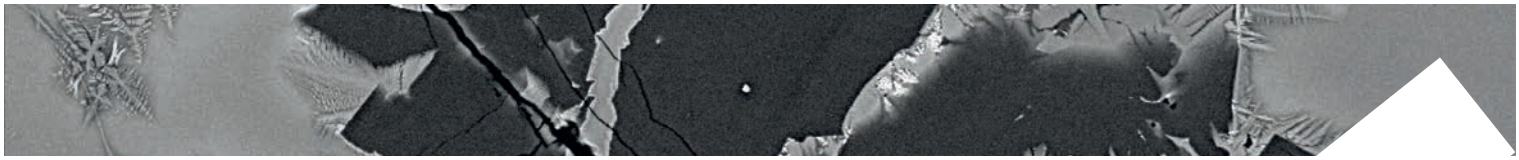

Conferenza A. Rittmann

Catania (Italy) I 12-14 February

Andronico D., Del Bello E., Ciancitto F., Cristaldi A., D'Oriano C., Landi P., PennacchiaF., Ricci T., Scarlato P., Taddeucci J.
The 3 July and 28 August 2019 paroxysms at Stromboli

Capizzi L.S., Stagno V., Bosi F., Ballirano P., Andreozzi G.B., Scarlato P.
Iron-rich tourmaline breakdown at high pressure and temperature as potential source of metasomatic B-rich fluids in the mantle

Civico R., Ricci T., Andronico D., Cantarero M., De Beni E., Del Bello E., Di Traglia F., Eggersglüß M., Hansteen T., Hoernle K., Johnson J. B., Kwasnitschka T., Pizzimenti L., Scarlato P., Strehlow K., Taddeucci J.
Monitoring the morphological changes associated with the 3 July 2019 and 28 August paroxysmal eruptions at Stromboli volcano (Italy) using UAVs

De Astis G. and Giordano G.
The summer 2019 eruptive activity of Stromboli: new insights on volcano system from observations and field data collection of the July 3 and August 28 paroxysms

De Beni E., Cantarero M., Strehlow K., Kwasnitschka T., Eggersglüß M., Hansteen T., Hoernle K., Di Traglia F., Civico R., Ricci T., Andronico D., Del Bello E., Johnson J.B., Pizzimenti L., Scarlato P., Taddeucci J.
Stromboli paroxysms 2019: volume estimation and morphological changes

Gruppo di Lavoro Comunicazione INGVvulcani (HP-HT: De Astis, Ricci, Scarlato)
INGV Social Communication during Stromboli 2019 crisis

Marras G., Stagno V., Cerantola V., Perinelli C.
In situ Mössbauer spectroscopy on spinel and clinopyroxene of clinopyroxenites from the Hyblean plateau

Stopponi V., Stagno V., Kono Y., Hrubiak R., Misiti V., Scarlato P., Gaeta M.
Experimental constraints on mobility of volatile-bearing magmas and timing of melt-rock interaction in the Earth's upper mantle

Tamburello G., T. Ricci T., J. Taddeucci J., Del Bello E., Scarlato P.
High frequency UV camera imagery of Strombolian explosive activity

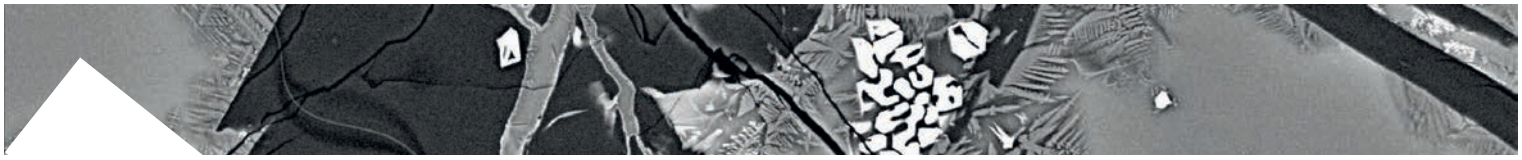

European Geoscience Union General Assembly

Vienna I Virtual Conference 4-8 May

Aretusini S., Cascajero A.N., Spagnuolo E., Tapetado A., Vazquez C., et al.
How hot is a lab-earthquake?

Bistacchi A., Mittempergher S., Smith S.A.F., Di Toro G., Nielsen S.
Detailed statistical analysis of the Gole Larghe Fault Zone fracture network (Italian Southern Alps) improves estimates of the energy budget for intraplate earthquakes in basement rocks

Cornelio C., Passelegue F., Spagnuolo E., Toro G.D., Violay M.
Earthquake nucleation in presence of viscous fluids:
Thermal Pressurization or Elastohydrodynamic Lubrication?

De Beni E., Andronico D., Cantarero M., Civico R., Del Bello E., Di Traglia F., Eggersglüß M., Hansteen T., Hoernle K., Johnson J., Kwasnitschka T., Pizzimenti L., Ricci T., Scarlato P., Strehlow K., Taddeucci J.
UAV surveys illuminate the morpho-structural and volume changes from the 2019 paroxysmal eruptions of Stromboli volcano (Italy)

Deegan F. M., Bédard J. H. ,TrollV. R., Dewing K., Geiger H., Grasby S. E., Misiti V., Freda C.
Voluminous crustal degassing and immiscible sulfide genesis caused by magma-shale interaction in Large Igneous Provinces

Di Toro G., Fondriest M., Mitchell T.M., Gomila R., Jensen E., Masoch S., Bistacchi A., Magnarini G., Faulkner D., Cembrano J., Mittempergher S., Spagnuolo E.
Field and experimental evidence of frictional melting in fluid-rich faults

Ferry M., Gautier S., Mazzotti S., Villani F., Stell E., Jacottin M., Pantosti D., Sapia V., Ricci T., Benedetti L., Di Giulio G., Vassallo M..
Structure and segmentation of the Ovindoli - Piano di Pezza - Campo Felice fault system (Central Apennines, Italy): Evolution and reactivation of inherited faults

Fondriest M., Balsamo F., Bistacchi A., Clemenzi L., Demurtas M., Storti F., Di Toro G.
Structural Complexity and Mechanics of a shallow crustal Seismogenic Source
(Vado di Corno Fault Zone, Italy)

Giacomel P., Ruggieri R., Scuderi M.M., Spagnuolo E., Di Toro G., Collettini C.
Frictional strength, stability, and healing properties of basalt faults for CO2 storage purposes

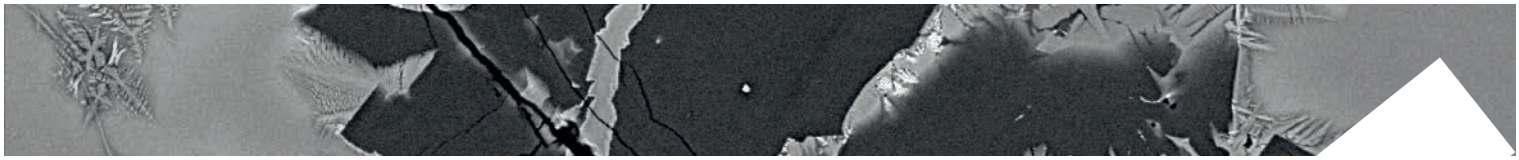

Lang S., Mollo S., France F., Nazzari M., Misiti V., Gurenko A.A., Devidal J.L.
Kinetic aspects of major and trace elements in olivines from variably cooled basaltic melts

Misiti V., Riposati D., Di Laura F., Crescimbene M.
Geotrivial pursuit: discovering the earth planet

Petrone C.M., Di Stefano F., Gertisser, R., Mollo S., Tommasini S., Del Bello E., Andronico D., Scarlato P., Giacomoni P.P., Coltorti M.
Significant changes in the magma dynamics of Stromboli steady-state volcano recorded by clinopyroxene crystals

Sapia V., Villani F., Fischanger F., Lupi M., Baccheschi P., Brunori C.A., Civico R., Coco I., De Martini P.M., Giannattasio F., Improta L., Materni V., Murgia F., Pantosti D., Pizzimenti L., Pucci S., Ricci T., Romano V., Sciarra A., Smedile A.
A deep resistivity Full Waver survey unravels the 3D structure of the Castelluccio basin in relation to the source of the 2016 Mw 6.5 Norcia earthquake (central Italy)

Taddeucci J., Del Bello E., Merrison J.P., Rasmussen K.R., Iversen J.J., Scarlato P., Ricci T., Andronico D.
In situ study of volcanic ash resuspension using a portable wind tunnel

Goldschmidt 2020 Conference

Virtual | 21-26 June

Iezzi G., Lanzafame G., Mancini L., Behrens H., Tamburrino S., Vallefuoco M., Passaro S., Signanini P., Ventura G.
Deep sea explosive eruptions may be not so different from subaerial eruptions

MacDonald A., Ubide T., Masotta M., Mollo S., Pontesilli A.
The Role of Undercooling on Trace Element Partitioning in Sector-Zoned Clinopyroxene

Petrone C.M., Di Stefano F., Mollo S., Gertisser R., Del Bello E., Andronico D., Scarlato P.
The 2019 Paroxysms at Stromboli Volcano (Italy): Timescales of Eruption Triggering

Pontesilli A., Brenna M., Ubide T., Mollo S., Masotta M., Caulfield J., Le Roux P., Nazzari M., Scarlato P.
Basalt Alkalinity Modulated by a Lithospheric “Filter”: Thermobarometry of a Complex Plumbing System beneath the Dunedin Volcano

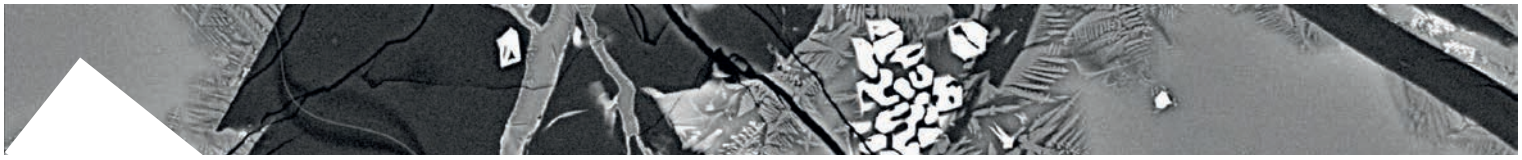

106° Congresso Nazionale Società Italiana di Fisica

14-18 September

Taddeucci J., Scarlato P.

High-speed imaging of subsonic to supersonic jets from explosive volcanic eruption

INVITED

AGU Fall Meeting

San Francisco, USA I 1-17 December

Bistacchi A., Mittempergher S., Di Toro G.

New combined nonparametric/parametric statistical analysis of fracture networks to unravel the evolution of fault zones: a study of the exhumed seismogenic Gole Larghe Fault Zone (Italian Southern Alps)

Conrad E., Tisato N., Di Toro G., Carpenter B., Faccenna C.

New data on the stick-slip mechanics of seismogenic faults from rotary shear experiments

Cornelio C., Spagnuolo E., Nielsen S., Passelègue F., Di Toro G., Violay M.

Weakening mechanisms efficiency during seismic slip

Pozzi G., Scuderi M. M., Tinti E., Di Stefano G., Collettini C.

The role of fault fabric in fault stability under different stress conditions

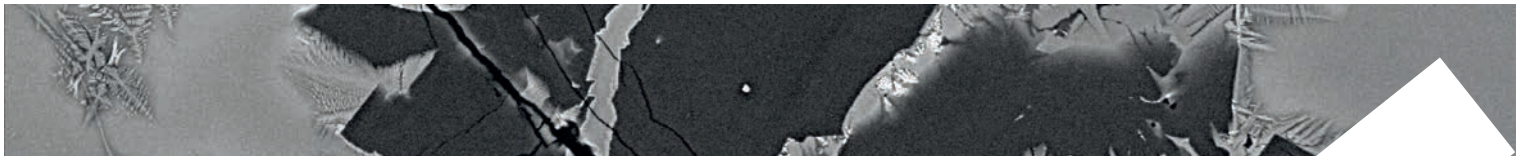

12| PUBLICATIONS

Bini G., Chiodini, G., Lucchetti C., Moschini P., Caliro S., Mollo S., Selva J., Tuccimei P., Galli G., Bachmann O.
Deep versus shallow sources of CO_2 and Rn from a multi-parametric approach: the case of the Nisyros caldera (Aegean Arc, Greece)
Scientific Report, https://doi.org/10.1038/s41598-020-70114-x

Boncio P., Amoroso S., Galadini F., Galderisi A., Iezzi G., Liberi F.
Earthquake-induced liquefaction features in a late Quaternary fine-grained lacustrine succession (Fucino Lake, Italy): implications for microzonation studies
Engineering Geology, doi.org/ 10.1016/j.enggeo.2020.105621

Carapezza M. L., Tarchini L., Ranaldi M., Ricci T., De Simone G., Diano G., Gattuso A., Pagliuca N. M.
Continuous monitoring of CO_2 and H_2S air concentration and soil CO_2 flux survey for gas hazard assessment at Tor Caldara nature reserve (Anzio, Italy)
Quaderni di Geofisica, doi:10.13127/qdg/164

Carapezza M. L., Ranaldi M., Tarchini L., Ricci T., Barberi F.
Origin and hazard of CO_2 and H_2S emissions in the Lavinio-Tor Caldara zone (Metropolitan City of Rome Capital, Italy)
Journal of Volcanology and Geothermal Research, doi:10.1016/j.jvolgeores.2020.106985

Cornelio C., Spagnuolo E., Passelegue F., Di Toro G., Violay M.
Effect of fluid viscosity on fault reactivation and coseismic weakening
Journal of Geophysical Research, vol. 125, pp. 1-18, e2019JB01888, doi: 10.1029/2019JB018883

Costa S., Masotta M., Gioncada A., Pistolesi M., Bosch D., Scarlato P.
Magma evolution at La Fossa volcano (Vulcano Island, Italy) in the last 1000 years: evidence from eruptive products and temperature gradient experiments
Contributions to Mineralogy and Petrology, 175, 31, https://doi.org/10.1007/s00410-020-1669-0

De Astis G., Giordano G.
The summer 2019 basaltic Vulcanian eruptions (paroxysms) of Stromboli
Bulletin of Volcanology, https://doi.org/10.1007/s00445-020-01423-2

Demurtas M., Smith S.A.F., Spagnuolo E., Di Toro G.
Frictional properties and microstructural evolution of dry and wet calcite-dolomite gouges
Solid Earth https://doi.org/10.5194/se-2020-170

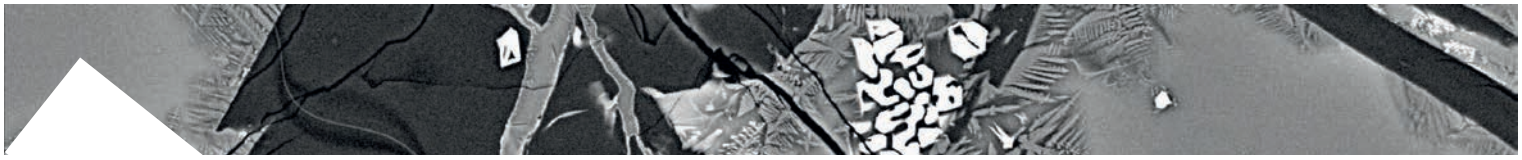

Di Nezza M., Misiti V., Di Laura F., D'Addezio G.
Escape Volcano: un nuovo gioco geo-scientifico
Miscellanea 55, ISSN 2039-6651

Di Stefano F., Mollo S., Ubide T., Petrone C.M., Caulfield J., Scarlato P., Nazzari M., Andronico D., Del Bello E.
Mush cannibalism and disruption recorded by clinopyroxene phenocrysts at Stromboli volcano: New insights from recent 2003–2017 activity
Lithos, https://doi.org/10.1016/j.lithos.2020.105440

Eichelberger J., Kiryukhin A., Mollo S., Tsuchiya N., Villeneuve M.
Exploring and Modeling the Magma–Hydrothermal Regime
Geosciences, 10.3390/geosciences10060234

Fondriest M., Mecklenburgh J., Passelegue F., Artioli G., Nestola F., Spagnuolo E., Rempe M., Di Toro G.
Pseudotachylyte alteration and the rapid fade of earthquake scars from the geological record
Geophysical Research Letters, 10.1029/2020GL090020

Fondriest M., Balsamo F., Bistacchi A., Clemenzi L., Demurtas M., Storti F., Di Toro G.
Structural Complexity and Mechanics of a shallow crustal Seismogenic Source (Vado di Corno Fault Zone, Italy)
Journal of Geophysical Research: Solid Earth, 125, https://doi.org/10.1029/2019JB018926

Giudicepietro F., Chiodini G., Avino R., Brandi G., Caliro S., De Cesare W., Galluzzo D., Esposito A., La Rocca A., Lo Bascio D., Obrizzo F., Pinto S., Ricci T., Ricciolino P., Siniscalchi A., Tramelli A., Vandemeulebrouck J., Macedonio G.
Tracking episodes of seismicity and gas transport in Campi Flegrei caldera trough seismic, geophysical and geochemical measurements
Seismological Research Letters, doi:10.1785/0220200223

Giuliani L., Iezzi G., Mollo S.
Dynamics of volcanic systems: physical and chemical models applied to equilibrium versus disequilibrium solidification of magmas
Geophysical Monograph Series, https://doi.org/10.1002/9781119521143.ch5

Giuliani L., Iezzi G., Vetere F., Behrens H., Mollo S., Cauti F., Ventura G., Scarlato P.
Evolution of textures, crystal size distributions and growth rates of plagioclase, clinopyroxene and spinel crystallized at variable cooling rates from a mid-ocean ridge basaltic melt
Earth-Science Reviews, https://doi.org/10.1016/j.earscirev.2020.103165

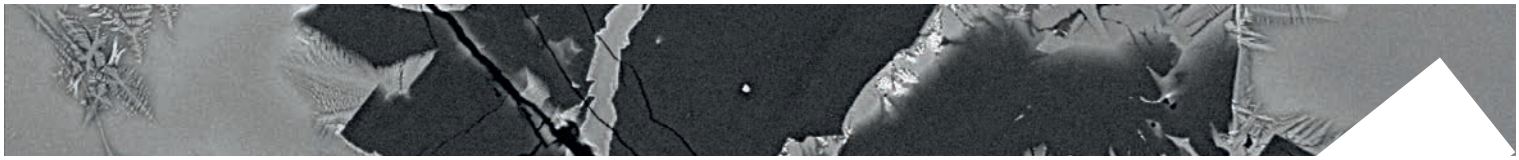

Giuliani L., Iezzi G., Hippeli T., Davis M., Elbrecht A., Vetere F., Nazzari M., Mollo S.
The Onset and Solidification Path of a Basaltic Melt by in situ Differential Scanning Calorimetry (DSC) and ex situ Investigations
Frontiers in Earth Science, 10.3389/feart.2020.00337

Hughes A., Kendrick J.E., Lamur A., Wadsworth F.B., Wallace P.A., Di Toro G., Lavallée Y.
Frictional behaviour, wear and comminution of synthetic porous geomaterials
Frontiers in Earth Science, section Earth and Planetary Materials, https://doi.org/10.3389/feart.2020.562548

Hughes A., Kendrick J., Salas G., Wallace P., Legros F., Di Toro G., Lavallée Y.
Shear localisation, strain partitioning and frictional melting in a debris avalanche generated by volcanic flank-collapse
Journal of Structural Geology, vol. 140, https://doi.org/10.1016/j.jsg.2020.104132

Iezzi G., Lanzafame G., Mancini L., Behrens H., Tamburrino S., Vallefuoco M., Passaro S., Signanini P., Ventura G.
Deep sea explosive eruptions may be not so different from subaerial eruptions
Scientific Reports, doi.org/10.1038/s41598-020-63737-7

Lombardo V., Pick L., Spinetti C., Taddeucci J., Zakŝek K.
Temperature and Emissivity Separation 'Draping' Algorithm Applied to Hyperspectral Infrared Data
Remote Sensing, 12(12), 2046. doi:10.3390/rs12122046

Masotta M., Pontesilli A., Mollo S., Armienti P., Ubide T., Nazzari M., Scarlato P.
The role of undercooling during clinopyroxene growth in trachybasaltic magmas: Insights on magma decompression and cooling at Mt. Etna volcano
Geochimica et Cosmochimica Acta, 268, 258–276, doi: https://doi.org/10.1016/j.gca.2019.10.009

Merico A., Iezzi G., Pace B., Ferranti L., Cremona M., Scafa M., Cavallo A., Colella A., Nazzari M., Scarlato P. Grain size and grain size distribution of a lithified fault core in carbonates rocks using multi-scale image analysis: the example of the San Benedetto-Gioia dei Marsi fault (Central Italy)
Journal of Structural Geology, https://doi.org/10.1016/j.jsg.2020.104017

Misiti V., Voltattorni N., Brunori C.A., Govoni A., Pizzimenti L., Murgia F., Pietrangeli D., Pinzi S.
L'INGV all'ISOLA DI EINSTEIN (Lago Trasimeno): giocando con la scienza
Miscellanea 54, ISSN 2039-6651

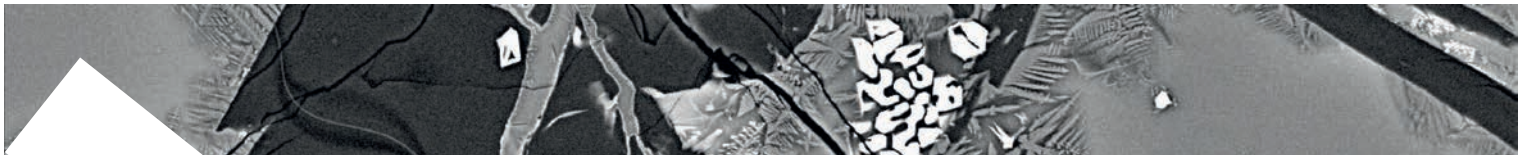

Mollo S., Blundy J., Scarlato P., Vetere F., Holtz F., Bachmann O., Gaeta M.
A review of the lattice strain and electrostatic effects on trace element partitioning between clinopyroxene and melt: Applications to magmatic systems saturated with Tschermak-rich clinopyroxenes
Earth-Science Reviews, https://doi.org/10.1016/j.earscirev.2020.103351

Mollo S., Ubide T., Di Stefano F., Nazzari M., Scarlato P.
Polybaric/polythermal magma transport and trace element partitioning recorded in single crystals: A case study of a zoned clinopyroxene from Mt. Etna
Lithos, https://doi.org/10.1016/j.lithos.2020.105382

Palummo F., Mollo S., De Astis G., Di Stefano F., Nazzari M., Scarlato P.
Petrological and geochemical modeling of magmas erupted at Vulcano Island in the period 54–8 ka: Quantitative constraints on the sub-volcanic architecture of the plumbing system
Lithos, https://doi.org/10.1016/j.lithos.2020.105715

Rempe M., Di Toro G., Mitchell T.M., Smith S.A.F., Hirose T., Renner J.
Influence of effective stress and pore-fluid pressure on fault strength and slip localization in carbonate slip zones
Journal of Geophysical Research: Solid Earth, 10.1029/2020JB019805, JGRB54497

Riposati D., D'Addezio G., Di Laura F., Misiti V., Battelli P.
Graphic design and scientific research – the National Institute of Geophysics and Volcanology (INGV) experience
Geoscience Communication, https://doi.org/10.5194/gc-3-407-2020

Robidoux P., Rizzo A.L., Aguilera F., Aiuppa A., Artale M., Liuzzo M., Nazzari M., Zummo F.
Petrological and noble-gas features of Lascar and Lastarria volcanoes (Chile): inferences on plumbing systems and mantle characteristics
Lithos, https://doi.org/10.1016/j.lithos.2020.105615

Rotolo S.G., Carapezza M.L., Correale A., Foresta Martin F., Hahn G., Hodgetts A.G.E., La Monica M., Nazzari M., Romano P., Sagnotti L., Siravo G., Speranza F.
Obsidians Of Pantelleria (Strait of Sicily): A Petrographic , Geochemical and Magnetic Study Of known And New Geological Sources
Open Archaeology,https://doi.org/10.1515/opar-2020-0120

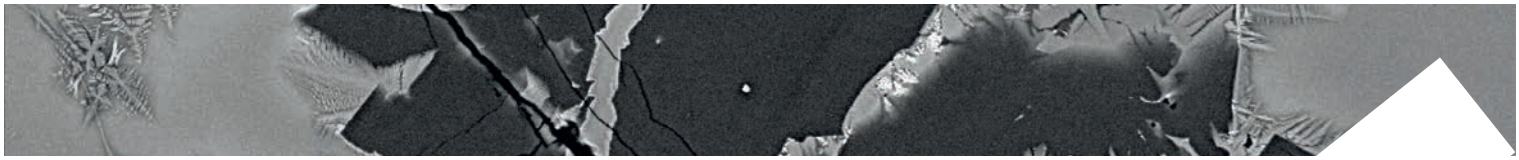

Rouwet D., Tamburello G., Chiodini G., Pecoraino G., Procesi M., Ricci T., Venturi S., Santi A., Cabassi J., Vaselli O., Tassi F., Costa A.
New insights into the degassing dynamics of Lago Albano (Colli Albani volcano, Rome, Italy) during the last three decades (1989-2019)
Italian Journal of Geosciences, doi:10.3301/IJG.2020.19

Rouwet D., Tamburello G., Ricci T., Sciarra A., Capecchiacci F., Caliro S.
CO_2 and H_2S degassing at Fangaia mud pool, Solfatara, Campi Flegrei (Italy): origin and dynamics of the pool basin
Minerals, doi:10.3390/min10121051

Salvatore V., Cigala V., Taddeucci J., Arciniega-Ceballos A., Peña Fernández J.J., Alatorre-Ibargüengoitia M.A., Gaudin D., Palladino D.M., Kueppers U., Scarlato P.
Gas-Pyroclast Motions in Volcanic Conduits During Strombolian Eruptions, in Light of Shock Tube Experiments
Journal of Geophysical Research Solid Earth, https://doi.org/10.1029/2019JB019182

Sciarra A., Cantucci B., Sapia V., De Ritis R., Ricci T., Civico R., Galli G., Cinti D., Coltorti M.
Geochemical and geoelectrical characterization of the Terre Calde di Medolla (Emilia-Romagna, northern Italy) and relations with 2012 seismic sequence
Journal of Geochemical Exploration, doi:10.1016/j.gexplo.2020.106678

Selva J., Bonadonna C., Branca S., De Astis G., Gambino S., Paonita A., Pistolesi M., Ricci T., Sulpizio R., Tibaldi A., Ricciardi A.
Multiple hazards and paths to eruptions: A review of the volcanic system of Vulcano (Aeolian Islands, Italy)
Earth-Science Reviews, doi.org/10.1016/j.earscirev.2020.103186

Stagno V. , Stopponi V., Kono Y., D'Arco A., Lupi L., Romano C., Poe B.T., Foustoukos D.I., Scarlato P., Manning C.E.
The Viscosity and Atomic Structure of Volatile-Bearing Melilititic Melts at High Pressure and Temperature and the Transport of Deep Carbon
Minerals, 10(3), 267, https://doi.org/10.3390/min10030267

Stagno V., Kono Y.,Stopponi V., Masotta M., Scarlato P., Manning C.E.
The viscosity of carbonate-silicate transitional melts at Earth's upper mantle P-T conditions by in-situ falling-sphere technique
In Manning, C.E., Lin, J-F., Mao, W. (Eds) Carbon in Earth's Interior, AGU monographs. https://doi.org/10.1002/9781119508229.ch19

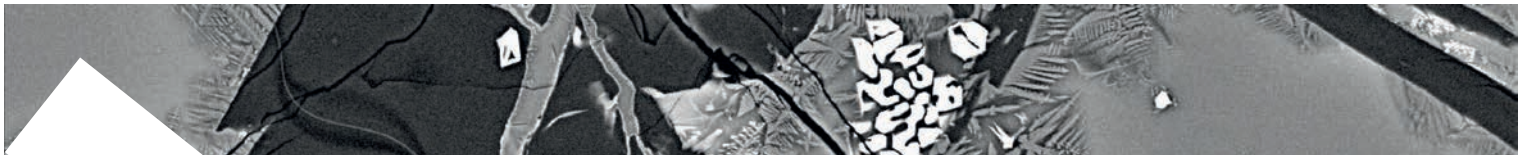

Taddeucci J., Scarlato P., Del Bello E., Spina L., Ricci T., Gaudin D., Tournigand P.Y.
The dynamics of explosive mafic eruptions: New insights from multiparametric observations
in: Forecasting and Planning for Volcanic Hazards, Risks, and Disasters, Hazard and Disasters series, eds. J. F. Shroder and P. Papale, Elsevier, 2, 9, 379-411, ISBN: 978-0-12-818082-2

Villani F., Pucci S., Azzaro R., Civico R., Cinti F., Pizzimenti L., Tarabusi G., Branca S., Brunori C. A., Caciagli M., Cantarero M., Cucci L., D'Amico S., De Beni E., De Martini P. M., Mariucci M. T., Messina A., Montone P., Nappi R., Nave R., Pantosti D., Ricci T., Sapia V., Smedile A., Vallone R., Venuti A.
Surface ruptures database related to the 26 December 2018, MW 4.9 Mt. Etna earthquake, southern Italy
Scientific Data, doi:10.1038/s41597-020-0383-0

In press

Del Bello E., Taddeucci J., Merrison J.P., Rasmussen K.R., Andronico D., Ricci T., Scarlato P., Iversen J.J.
Field-based measurements of volcanic ash resuspension by wind
Earth and Planetary Science Letters, https://doi.org/10.1016/j.epsl.2020.116684

Foresta Martin F., Rotolo S., Carapezza M., Nazzari M.
Chlorine as a Discriminant Element to Establish the Provenance of Central Mediterranean Obsidians
Open Archaeology

Houghton B.F., Tisdale C.M., Llewellin E.W., Taddeucci J., Orr T.R., Walker B.H., Patrick M.R.
The birth of a Hawaiian fissure eruptio. Journal of Geophysical Research: Solid Earth
https://doi.org/10.1029/2020JB020903

Scarlato P., Mollo S., Petrone C.M., Ubide T., Di Stefano F.
Interpreting magma dynamics through a statistically refined thermometer: Implications for clinopyroxene Fe-Mg diffusion modeling and sector zoning at Stromboli
AGU books - Crustal Magmatic System Evolution: Anatomy, Architecture, and Physico-Chemical Processes

Stagno V., Aulbach S.
Redox Processes Before, During, and After Earth's Accretion Affecting the Deep Carbon Cycle
AGU book5

Bruno M., Caramelli A., Romeo G., Savio G.
Rimessa per velivoli multi-rotore a controllo remoto
Brevetto per invenzione industriale N. 102017000076573

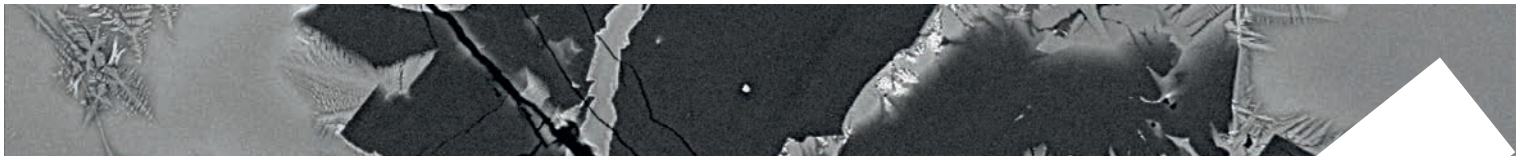

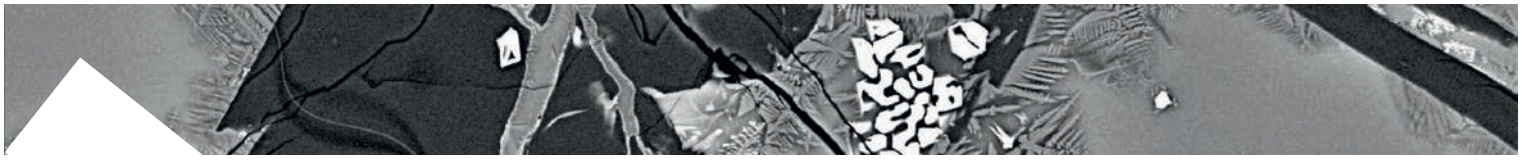

Design by Laboratorio Grafica e Immagini INGV

Editing by Valeria Misiti

Rome, March 2021